Brigham Young University

BYU ScholarsArchive

2005-07-15

Experimental and Numerical Investigation of Tool Heating During Friction Stir Welding

Joshua L. Covington
Brigham Young University - Provo

Follow this and additional works at: https://scholarsarchive.byu.edu/etd

Part of the Mechanical Engineering Commons

EXPERIMENTAL AND NUMERICAL INVESTIGATION OF

TOOL HEATING DURING FRICTION STIR WELDING

by

Joshua L. Covington

A thesis submitted to the faculty of

Brigham Young University

in partial fulfillment of the requirements for the degree of

Master of Science

Department of Mechanical Engineering

Brigham Young University

December 2005

BRIGHAM YOUNG UNIVERSITY

GRADUATE COMMITTEE APPROVAL

of a thesis submitted by

Joshua L. Covington

This thesis has been read by each member of the following graduate committee and by majority vote has been found to be satisfactory.

_____   _____
Date   Brent W. Webb, Chair

_____   _____
Date   Tracy W. Nelson

_____   _____
Date   Carl D. Sorensen

BRIGHAM YOUNG UNIVERSITY

As chair of the candidate's graduate committee, I have read the thesis of Joshua L. Covington in its final form and have found that (1) its format, citations, and bibliographical style are consistent and acceptable and fulfill university and department style requirements; (2) its illustrative materials including figures, tables, and charts are in place; and (3) the final manuscript is satisfactory to the graduate committee and is ready for submission to the university library.

_____   _____
Date   Brent W. Webb
                                     Chair, Graduate Committee

Accepted for the Department

                                     _____
                                     Matthew R. Jones
                                     Graduate Coordinator

Accepted for the College

                                     _____
                                     Alan R. Parkinson
                                     Dean, Ira A. Fulton College of Engineering
                                     and Technology

ABSTRACT

EXPERIMENTAL AND NUMERICAL INVESTIGATION OF

TOOL HEATING DURING FRICTION STIR WELDING

Joshua L. Covington

Department of Mechanical Engineering

Master of Science

The heat input to the tool has been investigated for friction stir welding (FSW) of

aluminum alloy AL 7075-T7351 over a wide range of process operating parameters using

a combined experimental/numerical approach. In a statistical Design of Experiments

fashion, 54 experimental welds (bead-on-plate) were performed at 27 different parameter

combinations. Measured outputs during each of the welds included forces in all three

coordinate directions and internal temperature of the rotating tool at three locations near

the tool/workpiece interface. The heat input to the tool was also identified for each weld

using infrared imaging temperature measurement techniques and the portion of the total

mechanical power entering the tool was calculated. These values were subsequently

analyzed to identify the effect of process operating parameters. Two-dimensional,

axisymmetric numerical heat conduction models of the tool were then produced and

the approximate spatial distribution of the heat input to the tool along the tool/workpiece interface was identified.

Experimental values for the heat input to the tool ranged from 155 W to 200 W, comprising 2.8% to 5.1% of the total mechanical power. Regression equations developed for the two values show that each is a function of the process operating parameters. Heat conduction models of the tool show that the approximate spatial distribution of the heat input to the tool along the tool/workpiece interface is one where the heat input is distributed non-uniformly along the interface, with 1% entering the tool at the pin, 20% entering at the base of the pin, and the remainder entering the flat portion of the shoulder. This distribution was valid for the majority of process operating parameter combinations tested. The maximum predicted temperature for the simulations occurred in the pin. This result was verified by the experimental tool temperature measurements. Insights gained into the FSW process from the combined experimental/numerical investigation were then discussed.

ACKNOWLEDGEMENTS

I would like to first thank my wife, Joslyn, for always believing in and loving me and for helping me to believe in myself. I would also like to acknowledge the support of all of my family and friends who have inspired and taught me throughout my life. I would also like to thank my graduate committee for their help and guidance and my colleagues in the Friction Stir Research Lab for learning along with me.

TABLE OF CONTENTS

LIST OF TABLES

LIST OF FIGURES

1 Introduction

1.1 Process Introduction

Friction stir welding (FSW) is a solid-state joining process by which an interface-free union of two workpieces is formed [Thomas, 1991]. A non-consumable, rotating tool consisting of a smaller, protruding cylinder (pin) and a larger, concentric, outer cylinder (shoulder) is forced, or plunged, into the joint line of the workpieces until the shoulder is in intimate contact with the top surface of the workpieces. After a short dwell time, the tool and workpieces are then moved relative to each other such that the tool traces the joint line, after which the tool is extracted from the workpiece (Figure 1). Heat produced at the tool/workpiece interface from friction and interfacial shear is sufficient to locally soften the workpieces. The rotation of the tool aids in 'stirring' the workpieces together
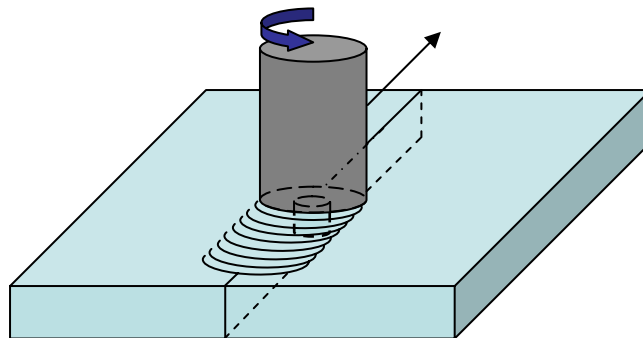
Figure 1. Schematic of the friction stir welding process.

1

to form a potentially defect-free bond. The joint that is produced is solid-state in nature, meaning that the workpiece material was not actually melted during the process, but only softened.

FSW has proven to be an effective joining technique for a variety of different materials, including metals and polymers. Metals with low melting temperatures such as aluminum and copper were among the first to be joined by this technique using a steel tool. More recently, with the development of tools with high-temperature strength characteristics, the welding of materials with high melting temperatures such as mild and stainless steel has been possible [Sorensen, 2001]. Regardless of the material, research has shown that joints produced by FSW retain much of the base material strength and have many other advantages over joints produced by traditional welding techniques [Mahoney, 1998; Sterling, 2003]. It is generally thought that such advantages stem from the lower heat input required by FSW. Studies report that the maximum temperature in the material being welded is usually less than 80% of its melting temperature [Chao, 1998]. However, some maximum temperatures closer to the melting point have been reported for thick-section welds [Song, 2003a; Song, 2003b; Song, 2003c; Colegrove, 2003]. Ideal welds generate only enough heating for the material to become plastic and flow around the tool. Weld parameters such as spindle speed, feed rate, and tool position are adjusted during experiments to keep the temperature just high enough around the tool for proper material flow and weld consolidation, filling the cavity produced by the pin and forming a solid joint. Optimal weld parameters for a given tool/workpiece combination are typically found using a trial and error approach over a wide range of operating parameters.

1.1.1 The FSW Tool

The tool plays a very important role in successful joints produced by FSW. Tool shape and size will dictate, to some degree, material flow and heat generation in the weld zone, which will, in turn, affect the final weld properties. The shoulder of the tool, which is thought to be the main source of heat generation, is typically concave in shape. This aids in weld consolidation by forcing the softened material to remain in the weld zone as the tool traverses the joint line. The pin also plays a very important role, joining the workpieces in a through-thickness manner. It is thought that the portion of the heat that is generated by the pin is considerably smaller than that generated by the shoulder, but an intense region of shearing and flowing material must exist in order for the workpiece material to move around the pin and reconsolidate behind it. Although a pin with a smooth surface has proven to be satisfactory for many weld configurations, features are often added to the pin, such as facets, flats, or threads, to increase the ability of the pin to move through the workpiece material and to aid in material mixing which can occur in both a horizontal and vertical manner. Temperatures in the tool and workpiece are often near the solidus of the workpiece and 3-8 kW of mechanical power are converted to heat during each weld. Thus, for a complete understanding of the FSW process, both tool and workpiece need to be carefully considered.

1.2 Previous Literature

An understanding of heat generation, heat flow, and temperature distributions that exist in both the workpiece and tool has come from a combined approach of mathematical modeling and experimental observation. The models are implemented in either a closed-

form, or analytical, nature that can be solved using a spreadsheet computer program or in a numerical form, utilizing commercial software packages that divide the modeled domain into numerous cells and calculate desired values at each point in the domain. The typical approach for FSW modeling is to obtain predictions from a model and then validate the model using experimental workpiece temperature measurements taken using thermocouples which are placed at various locations in the workpiece during weld experiments. Occasionally, tool temperatures will also be used for model validation. Portions of the model are then adjusted until agreement is reached between the predicted and measured temperature fields.

Since the FSW process is driven by the heat generated at the tool/workpiece interface, a model of the process is similarly driven by this input value. Other values, such as the heat that is transferred from the back side of the workpiece or heat that is transferred into the tool, are also unknown and must be investigated. Various attempts have been made to better understand the exact mechanisms of heat generation using the combined experimental/mathematical modeling method outlined. However, few researchers have specifically analyzed the heat that enters the tool or noted variation in this value that may occur with respect to operating parameters. The spatial distribution of the heat input along the tool/workpiece interface has similarly not been investigated.

1.2.1 Research Focused on Workpiece Temperatures

Analytical modeling strategies were among some of the first methods used to predict workpiece temperatures. Stewart et al. used two analytical models to analyze weld forces, torques, and maximum workpiece temperatures, and their results were compared with some of the first experimental data available [Stewart, 1998]. In a similar manner,

4

Gould and Feng predicted workpiece temperatures using a three-dimensional analytical model derived from the Rosenthal equations describing a moving heat source [Gould, 1998]. The heat input was a function of process operating parameters and was applied in the model as a circular ring on top of the workpiece with a radius equal to that of a typical FSW tool. Although the results were not compared with experimental data, modification of the model to correlate with weld experiments, which was published by McClure et al., allowed for ample prediction of workpiece temperatures [McClure, 1998]. More recently, Heurtier et al. also used an analytical model to predict workpiece temperatures [Heurtier, 2002], but later converted the model to a numerical form to increase prediction accuracy [Heurtier, 2003; Desrayaud, 2004].

Numerical investigations of FSW have given some wonderful insight into FSW workpiece temperature distributions. One of the first numerical FSW studies focused on workpiece temperatures was produced by Chao and Qi in which a moving, circular heat flux region on the top surface of the workpiece with a magnitude that was proportional to radial location simulated the heat generated by the tool [Chao, 1998]. The heat input to the weld and heat transfer from the bottom of the workpiece were iteratively adjusted until predicted workpiece temperatures matched those from validation experiments. Later, a similar approach was adopted by Khandkar and Khan in their numerical model of overlap FSW, but only iterative adjustments of the heat transfer from the workpiece were made and an additional heat generation term in the vicinity of the pin was included [Khandkar, 2001]. The total heat input was a function of process variables. Khandkar et al. [2003] and Reynolds et al. [2003] also investigated workpiece temperature distributions by iteratively adjusting heat transfer from the workpiece, but the total heat

input value was calculated from experimental torque measurements. The profile of the tool was also maintained by applying the heat input at locations on the top surface of the workpiece corresponding to the shoulder and within the workpiece corresponding to the side and bottom of the pin. The applied heat flux varied linearly with position.

In a unique class is the numerical approach taken by Frigaard et al. in their finite-difference model used to predict the transient physics of FSW [Frigaard, 2001]. The total heat input, calculated from process variables and tool geometry, was divided by the number of square grid points that approximately defined the tool shoulder and pin. This volumetric source term then moved with each time step to simulate the tool traverse. The energy input was periodically adjusted so that predicted temperatures in the workpiece did not exceed the specified melting point of the workpiece material.

1.2.2 Studies that Included the Tool

Among the first researchers to include the tool in their thermal analysis of FSW were Russell and Shercliff [Russell, 1998]. Using analytical models based on the Rosenthal equations a heat generation amount was predicted and an approximate interface temperature was calculated. The heat flow through the tool was then determined using one-dimensional heat conduction and was calculated to be 17% of the total weld energy. The derived heat input was then applied in their model as a vertical line source at the weld joint and workpiece temperatures were predicted. Extensions of this work were later reported, giving better experimental agreement, especially at locations away from the tool, and proving the utility of the analytical formulation developed [Russell, 1999; Russell, 2001].

More recently, researchers using numerical techniques have accounted for energy entering the tool by reducing the heat input to the workpiece. Schmidt and Hattel assumed arbitrarily that 25% of the mechanical energy required by the rotating spindle entered the tool, applying the remaining 75% to the workpiece [Schmidt, 2004a]. Similar to some of the research already presented, the heat input magnitude in the shoulder region of this model was proportional to radial location. A separate numerical model, again presented by Schmidt and Hattel, utilized both frictional heating and plastic work to calculate the heat input, 10% of which was assumed to enter the tool [Schmidt, 2004b]. Shi et al. also accounted for heat entering the tool by arbitrarily assuming a value (initially 8% of the mechanical energy) in their numerical analysis, but then adjusted the value until an agreement was reached with experimental data [Shi, 2003]. The heat input to the workpiece was also proportional to radial location.

Simar et al. [2004] used some initial work by Schmidt et al. [2004c] as a starting point for their numerical investigation of FSW. However, the arbitrary assignment of the tool heat input value was eliminated by monitoring the temperature of the tool at two axial locations above the shoulder during each experimental weld, from which the heat flow through the tool was approximated as being 5% of the total mechanical power input. It was reported that there was little variation detected in this value when welding at three different spindle speed values in the range of 500-1000 rpm. Portions of the heat entering the plate were then applied in both the shoulder and pin regions of the workpiece, with some additional heat applied to the workpiece in the area just outside of the weld zone (workpiece heat affected zone). A linearly varying heat input to the shoulder was again used while heat in the pin region was applied on the side of the pin as a heat flux.

Other researchers accounted for energy entering the tool without presenting the values used. Colegrove modeled both the tool and workpiece and applied a constant temperature boundary condition (at room temperature) on the top of the tool to account for energy entering the tool and machinery [Colegrove, 2000]. Both Hyoe et al. [2003] and Colegrove and Shercliff [2003] modeled the backing plate, tool, and workpiece in their investigations and indicated that heat entering the tool was accounted for, but no specifics were reported [Hyoe, 2003]. The method used to account for energy entering the tool was also not indicated by Song and Kovacevic in their initial studies of thermal profiles in the workpiece which included the plunge, traverse, and extract portions of the weld process [Song, 2003a; Song, 2003b]. They later refined their model to include coupled thermal models of both the tool and workpiece and utilized convection heat transfer from the top and sides of the tool to account for heat entering the tool and machinery [Song, 2003c]. Ulysse similarly included both the tool and workpiece in his numerical model of FSW and thermal profiles of both were presented, but no discussion of heat generation or the tool heat input was given [Ulysse, 2002].

Some researchers have included the tool as a physical rather than a thermal presence. Langerman and Kvalvik [2003] and Siedel and Reynolds [2003] modeled two-dimensional flow around the pin. Chen and Kovacevic modeled a portion of the tool above the shoulder, neglecting the pin, and utilized it as a physical presence to predict residual stress distributions in the workpiece [Chen, 2003]. However, a heat generation that varied linearly with radial position was applied to the workpiece surface just under the tool, but the energy entering the tool was not accounted for. Askari et al. also included at least a portion of the tool as a rigid body in their model, which included a

threaded pin [Askari, 2001]. Although it appeared that tool temperature predictions were made, no discussion of either tool temperatures or tool heat input was given.

1.2.3   Studies Centered on the Tool

Some researchers have furthered the investigation of the portion of the heat that enters the tool by making it a focus of their work. Chao et al. used two separate numerical models in conjunction with experimental temperature measurement of both the tool and workpiece to investigate the heat input into each at two different tool feed rates [Chao, 2003]. Numerical models included an axisymmetric model of the tool used in the experiments, but without the pin, and a separate model of the workpiece. The heat input to the tool was applied along the shoulder and was a linear function of the radius. During experimental welds, five thermocouples were attached to the outer surface of the tool at different distances from the shoulder for model tuning and validation. Heat inputs to the tool were approximated as 85 W and 86 W, which equated to 3.9% and 3.4% of the mechanical power measured during weld experiments (2218 W and 2535 W). Heat inputs to the workpiece were calculated as being 1740 W and 1860 W.

Dickerson et al. also used numerical tool models combined with experimental measurements to investigate the transient and steady-state heat input to FSW tools [Dickerson, 2003]. Thermocouples placed on the top surface of the workpiece were welded over and the recorded temperature was assumed to be the interface temperature. A total power input to the weld was also calculated from the experimental torque measurements. Numerical models of the tool were then generated which included the tool, tool holder, and machinery and the heat input to the tool was applied as a constant temperature boundary condition, equal to the assumed interface temperature, for the

9

shoulder surface and pin volume. Using this method it was reported that approximately 10% of the measured power entered the tool for steady-state FSW.

1.2.4 Tool Temperature Measurement

Perhaps due to the complexity of measuring the temperature of a rotating body, very few researchers have used temperature measurements of the tool for the experimental validation of numerical models and/or the investigation of tool heat inputs. It has already been mentioned that Simar et al. utilized a purely experimental approach to calculate the tool heat input by measuring internal tool temperatures at two axial locations [Simar, 2004]. In a similar fashion, Lienert et al. utilized measurements from two thermocouples attached to the outer surface of the tool at different positions above the tool shoulder in conjunction with infrared imaging of the tool surface to approximate temperature gradients and heat flow through the tool when welding mild steel [Lienert, 2003a]. The steady-state heat flow through the tool was approximated to be 25% of the experimental weld power. A similar two-thermocouple system was again used by Lienert et al. when welding AL 6082 from which tool heat flow and energy losses to the environment by radiation and convection were approximated to be 13% of the power input calculated from torque measurements [Lienert, 2003b]. It is also worthy to note that research reported by both Lienert and Stellwag [2001] and North et al. [2000] indicated the measurement of internal tool temperatures at one location near the tool/workpiece interface and that Nishihara and Nagasaka [2003] measured internal tool temperatures at six locations in a modified tool.

1.3 Problem Statement/Solution Summary

The objective of the current research was to further investigate FSW tool heating by carefully analyzing the steady-state heat input to the tool over a wide range of process operating parameters for friction stir welding of aluminum alloy AL 7075-T7351. A combined experimental/numerical approach was used, which included internal temperature measurement of the rotating tool at three locations, external temperature measurement of the tool using infrared imaging temperature measurement techniques, and subsequent numerical tool models. In this manner both the heat input magnitude and approximate spatial distribution along the tool/workpiece interface were revealed and accurate temperature fields within in the tool were analyzed, giving insight into the FSW process.

2 Experimental Method

2.1 Equipment

2.1.1 Machine

Plates were friction stir processed (bead on plate) on a retrofitted Kearney & Trecker

knee mill with PLC/PC control and data acquisition system. The machine is capable of

performing welds over 1000 mm (42 in) in length and has a maximum travel speed of

approximately 790 mm/min. (31 in/min.). Each axis (x, y, and z (see Figure 2)) is servo-

driven and the position and velocity of each axis was monitored and recorded at a

frequency of 2 Hz during each weld. The power required by the 22.4 kW (30 hp) spindle

motor as well as all other measured parameters discussed hereafter were also recorded at

2 Hz. The spindle has a maximum speed of 1500 rpm. Z-load and Z-depth control are
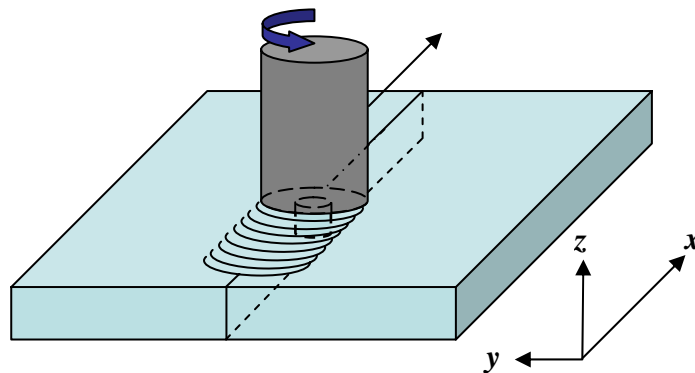
Figure 2. FSW schematic with axis definitions.

available and use feedback control to adjust the tool depth during welding such that a constant Z-force or tool depth is maintained. The latter was used in the current experiments.

2.1.2 Dynamometer

Mounted to the bed of the mill is a 1219 mm (48 in) long dynamometer capable of sensing forces up to 45 kN (10,000 lbf) in both the X- and Y-directions and 90kN (20,000 lbf) in the Z-direction with a resolution of 0.004 kN (1 lbf). The maximum possible workpiece width is approximately 305 mm (12 in). Fixtures for clamping the workpiece are mounted to the upper surface of the dynamometer.

2.1.3 Anvils

Conditions of the current experiment required the efficient running of multiple welds. As seen in Figure 3, a 15.9 mm (0.625 in) thick liquid-cooled aluminum cooling plate was fabricated to remove thermal energy from the workpiece, anvils, and dynamometer. A mixture of ethylene glycol and distilled water was pumped through the plate from a chiller and entered the plate at approximately 10°C. A 4.76 mm (0.1875 in) thick steel anvil was placed on top of the cooling plate for protection and to give a solid backing surface for the workpiece (see Figure 3). As previous work showed that cooling by means of this cooling plate had no significant effect on steady-state results, coolant was allowed to flow continuously through the plate while welding [Record, 2004].

2.1.4 Workpiece Material

The material used in this study was AL 7075-T7351 with a thickness of 9.53 mm (0.375 in). The plates were sheared to nominal dimensions of 127 mm (5 in) x 914 mm (36 in).
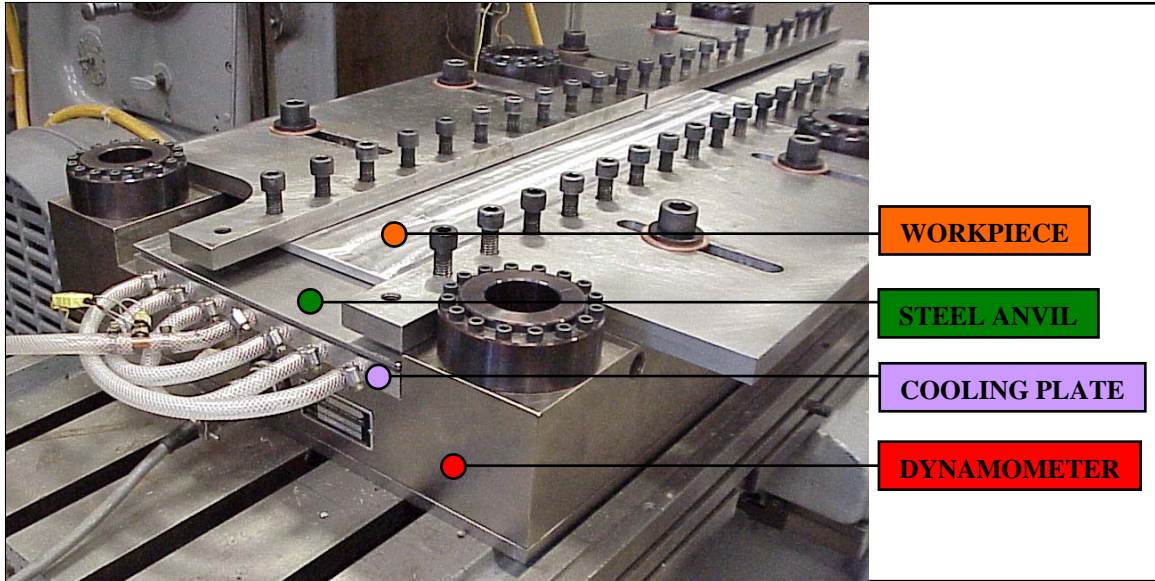
Figure 3. Experimental setup used: workpiece, anvil, cooling plate, and dynamometer.

The oxide layer was removed with a portable disc sander and the surface was cleaned with methanol prior to processing. The thickness of the plate was predetermined so that only partial penetration welds would be run, eliminating any possible interaction that could exist between the tool and the anvil.

2.1.5 Tool Holder/RF Telemetry System

A liquid-cooled tool holder was used to minimize heat flow into the machine head (see Figure 4). The coolant flow rate was approximately 1.9 L/min. (0.5 gal/min.) and was such that while welding there was typically less than 1°C rise in coolant temperature from the inlet of the tool holder to the outlet. Access holes near the top of the tool holder allowed tool thermocouples to be inserted through the back of the tool. A transmitting collar assembly was clamped to the rotating portion of the tool holder and housed RF transmitters which broadcasted the thermocouple readings as FM signals. The signals

15
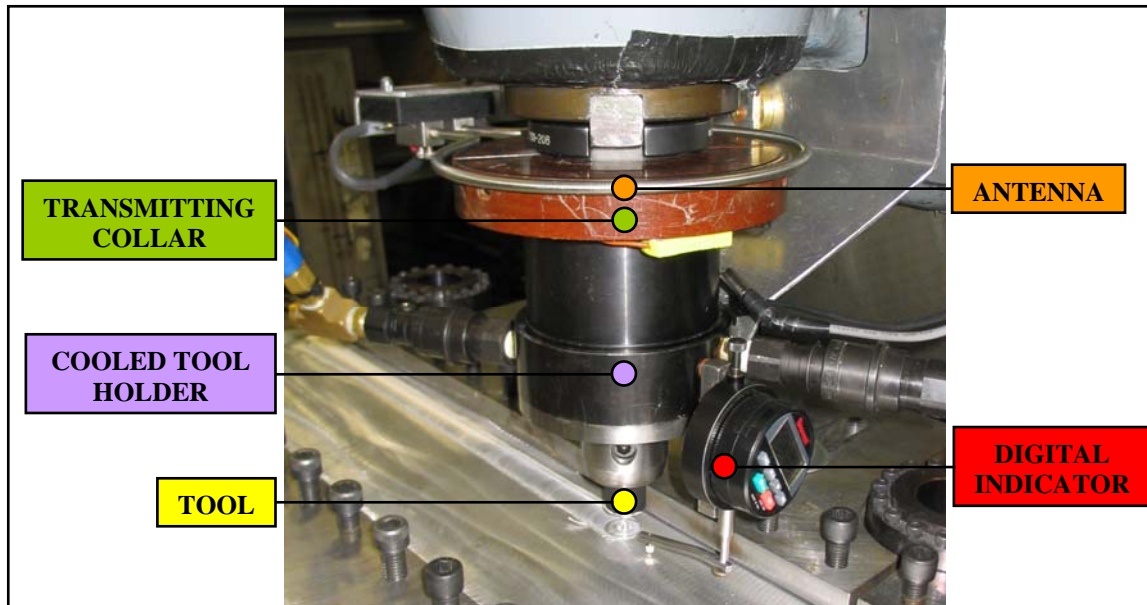
Figure 4. Cooled tool holder and electronic indicator used to measure shoulder depth.

were captured by the receiver through a stationary loop antenna and transferred to the

data acquisition system.

2.1.6 Electronic Depth Measurement and Control

An electronic digital indicator was mounted to the tool holder for tool depth measurement

and to provide an input for the Z-depth control. It has a range of 25.4 mm (1.0 in) and a

resolution of 0.002 mm (0.0001 in). An extension adapter was connected to the indicator

so that weld depth was measured as close to the tool as possible to account for any local

changes in tool depth. Readout error associated with attaching such an adapter is

estimated to be 0.025 mm (0.001 in) or less. The indicator readings are transferred to the

data acquisition system throughout the weld. This digital indicator was used to measure

the actual plunge and weld depth as seen in Figure 4. Due to machine deflection, the

programmed plunge depth will not actually be achieved. Thus, it is important to measure

the actual tool depth throughout the weld. The indicator was zeroed when the tip of the pin was in contact with the top of the workpiece.

2.1.7   Tool

The tool used for this study was manufactured from heat-treated H13 tool steel. Tool dimensions consisted of a shoulder diameter of 25.4 mm (1.0 in), body length (from the top of the tool to the shoulder) of 83.8 mm (3.3 in), shoulder concavity angle of 6 degrees, and a pin length not including the portion that extended into the concave shoulder cavity of 4.8 mm (0.1875 in). The pin was threaded with a pitch of 0.91 mm/thread (28 threads/in), had a major diameter of 7.9 mm (0.31 in), and a minor diameter of approximately 6.9 mm (0.27 in). The tool was used at a tilt angle of 2.5 degrees.

Internal Tool Temperature Measurement

The tool was modified for internal temperature measurement at three different locations near the tool/workpiece interface. An EDM drill was used to cut long, straight, square-bottomed holes to accommodate 1.6 mm (0.063 in) diameter 304 stainless steel sheathed thermocouples at the locations defined in Figure 5. The thermocouple locations are noted here as Pin Center, Root, and Shoulder. The distance between the end of the thermocouple and tool/workpiece interface at each location was 1.3 mm (0.05 in) or less.

Temperature measurement locations were verified by checking hole position, diameter, depth, and shape. Since hole shape can be quite difficult to inspect on a long, deep hole, initial trials were visually inspected by destructively sectioning the tools. Thermocouples slid freely to the desired locations and only a limited amount of oxide, if

17
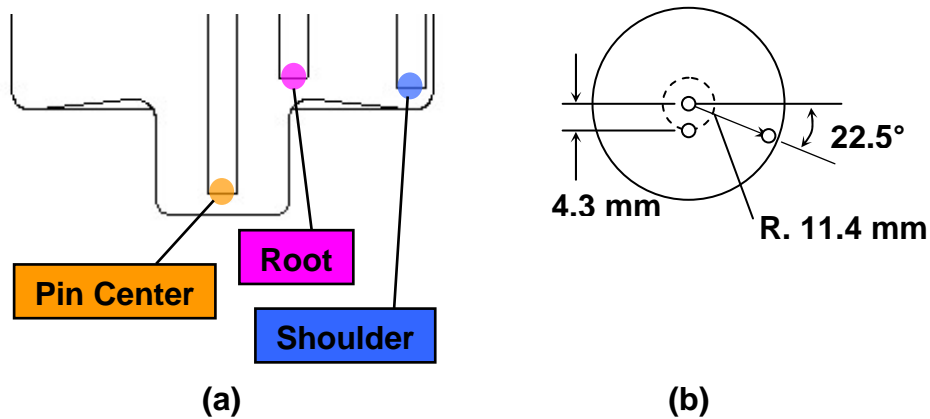
Figure 5. Tool internal temperature measurement locations: (a) tool cross section; (b) radial positions of thermocouples. Threads omitted for simplicity.

any, was present in the holes. Although steps were taken to ensure solid contact at each location between the end of the thermocouple and the bottom of the hole, there still exists the possibility of either minimal contact or no contact (small air gap). Despite these possible conditions, the character of the hole as a blackbody cavity ensures measurement of an accurate steady-state tool temperature if these conditions arise.

To ensure that the thermocouple readings accurately reflected the true physics of the process, the FSW tool was modified as little as possible. Calculations showed that the cross-sectional area of the tool body removed to accommodate the thermocouples was less than 2% and the cross-sectional area of the pin removed was approximately 6%. It can also be seen in Figure 5(b) that the thermocouple holes were spaced circumferentially as well as radially to limit local disruption of the heat flow.

The thermocouples were manufactured by Omega Engineering, Inc., and were of the ungrounded junction type (Figure 6). The 30 AWG (0.010 in diameter) thermocouple wires run inside the metal sheath and are insolated from each other and the sheath by a magnesium oxide (MgO) powder and are joined separate from the sheath near the probe
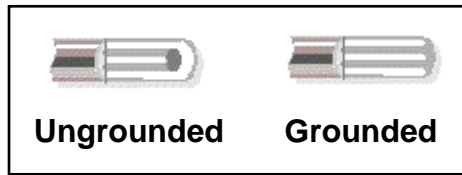
Figure 6. Thermocouple junction types [omega.com].

end. Although this configuration increases the response time of the thermocouple, it electrically isolates the thermocouple junction from the sheath, a characteristic required when using multiple thermocouples in the RF telemetry system. The time constant for the thermocouples when measuring the temperature of steels proved to be longer than that quoted by the manufacturer in water (0.25 sec.), suggesting that measurements taken during the transient phase of FSW may have some temporal lag. However, the measured time constant of 4 sec. proved that for steady-state regions the temperature measurements would be accurate.

External Surface Temperature Measurement

The external surface temperature of the tool was continuously monitored during welding using infrared (IR) imaging temperature measurement techniques. A FLIR SC 500 infrared camera system with an available 2X zoom lens was used to monitor the surface temperature of the tool. The zoom lens allowed for a high-resolution image while keeping the camera a safe distance from moving machinery. The IR system consisted of a camera, laptop computer with FLIR's ThermaCAM Researcher 2001 software interface, and associated cabling.

The SC 500 camera utilizes a solid-state Focal Plane Array (FPA) detector with a spectral range of 7-13 µm. No cryogenic cooling is required. It has a spatial resolution of 320 x 240 pixels and comes originally equipped with a 24° x 18° field of view lens.

The camera, which is configured with an optional high-temperature filter, has a temperature range of -40°C to 2000°C with an accuracy of ±2% of the reading, or ±2°C. When equipped with the optional zoom lens (12° x 9° field of view) the actual field of view at a distance of 1.2 m from the object being measured is reduced by a factor of 2 from 51 x 38 cm to 25 x 19 cm, which greatly increases the image resolution at larger distances.

The camera connects to the computer by means of a PC card interface. The ThermaCAM Researcher software package is then used to record and analyze the IR data, which comes in the form of an IR image recorded by the user. A sequence of successive IR images can also be recorded at various time intervals as specified by the user, with a maximum recording frequency of 5 Hz.

Once recorded, an image or sequence can be analyzed using the various tools available in the software. Analysis tools include such functions as image minimum, maximum and average temperatures, the analysis of temperature at one or more specific locations within the image, the placement of lines to track temperature profiles, and many others. A digital zoom function is also available. All of the analysis tools can be used on the recorded images, provided that focus adjustments are correct before and during the recording.

There are also different object parameters that must be specified by the user for accurate IR data analysis such Room Temperature, Relative Humidity, Object Distance from the Lens, etc. Perhaps the most important of these parameters, and the most difficult to quantify, is the Object Emissivity (ε). Although difficult to quantify in any case, this value for the tool surface would also change during FSW as the surface color

and finish change with an increase in temperature. The emissivity of the tool surface was thus controlled by coating the surface with a high-temperature, flat-black spray paint to establish a tool emissivity to unity (1.0). Emissivity validation experiments involved bringing both a painted and non-painted tool to a known, steady-state temperature in a high-temperature furnace. The surface temperature of each tool was monitored separately with a thermocouple clamped to the surface. The furnace door was then opened and an IR image of both tools was taken. A function available in the ThermaCAM Researcher known as the Emissivity Calculator was then used to calculate the emissivity for each tool. The tool emissivities were tested at 100°C intervals between 200°C and 500°C. It was confirmed through these experiments that the emissivity of the painted tool was indeed 1.0 at all temperatures tested (to within measurement uncertainty), while the emissivity of the non-painted tool changed from 0.4 to approximately 1.0 as the surface finish changed with increasing temperature.

The IR camera was placed such that a constant distance of 1295 mm (51 in) would exist between the tool and the front of the lens. It was placed in such a manner that, for the experimental setup used, what would be considered as the leading face of tool during a weld would be imaged. This orientation was desirable because the warm, already welded plate would move away from the camera, which would allow for a clearer view of the tool surface, even near the shoulder. Previous experiments had shown that the best images of the tool surface were obtained when the camera was level. Thus, a fixture was fabricated so that camera could remain level at a constant position, while the table of the machine could move freely below it. A photograph of the IR camera orientation relative to the tool is shown in Figure 7.
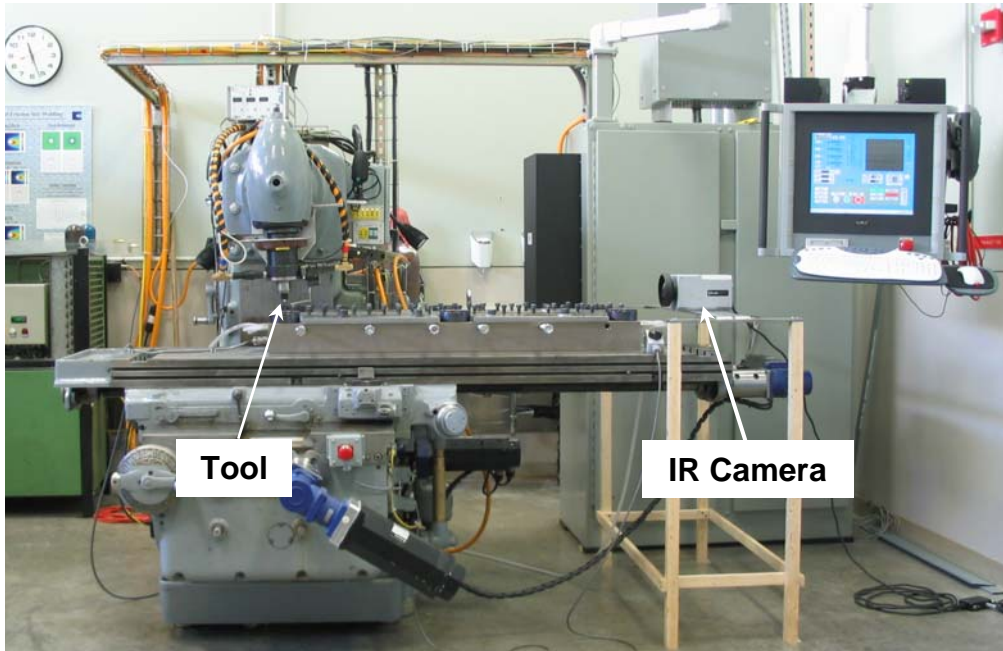
Figure 7. Thermal camera orientation relative to tool.

2.2 Experimental Design

A statistical Design of Experiments (DOE) was planned to analyze the effect of welding parameters on the heat input to the tool. This allowed for parameters to be adjusted in an orderly manner during experiments and a subsequent statistical analysis of the data revealed relationships between the inputs and outputs.

Initial, unpublished experiments were performed to identify a process parameter window for the tool and workpiece material chosen. These experiments also showed that various weld outputs seemed to be affected by a number possible input parameters including key process variables such as spindle speed, feed rate, and weld depth and other variables such as weld position relative to the side of the workpiece, plunge location, thermal state of the workpiece/anvils, etc. To analyze the effect of each of these variables a screening Design of Experiments was performed which proved that the key

input variable were, indeed, spindle speed, feed rate, and weld depth and that only one other variable may have an effect on the steady-state value of the outputs, that being weld position relative to the side of the plate [Record, 2004]. It should be noted that the identified process window pushed the extremes of the three main input parameters but ensured that sound welds were produced (i.e., good weld consolidation, good surface finish, little or no tool breakage, etc.).

With a known process parameter window and a knowledge that variations would exist in the data, it was determined that a 3^3 factorial DOE with two repetitions would be feasible and yield satisfactory results. This required $3^3*2 = 54$ welds at $3^3 = 27$ different parameter combinations. This DOE not only revealed the relationship between inputs and outputs, but provided information on process repeatability.

The three input parameters and their corresponding three levels each are shown in Table 1. While Spindle Speed and Feed Rate are self-explanatory, the input parameter listed as Shoulder Depth may need some additional clarification. Shoulder Depth is a measure of how far the shoulder penetrates the top surface of the workpiece. The Low factor level (0.24 mm) corresponds to a low degree of shoulder penetration, or a shallow weld, and the High factor level (-0.06 mm) corresponds to a high degree of shoulder penetration (i.e., a deep weld, see Figure 8). The Shoulder Depth value for each weld can be calculated by subtracting the tool pin length from the measured weld depth.

Table 1. Input parameters and levels.

	L	M	H
Spindle Speed [rpm]	200	350	500
Feed Rate [mm/min.]	51	178	305
Shoulder Depth [mm]	0.24	0.09	-0.06
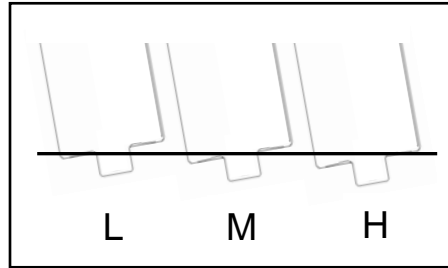
Figure 8. Illustration of the input termed Shoulder Depth.

Using analysis tools available in Minitab, a commercially available statistical software package, the DOE was constructed. When completed, the experimental design consisted of 54 experimental runs in a randomized run order. For each run the parameter combination was given. This randomized run order was followed during the experiments.

2.3   Welding Procedure

A plate was affixed at a predetermined location on the anvil and clamped into place. This same location was used for all plates in the study. The tool was then positioned directly over the plunge location and the pin was brought into contact with the top surface of the workpiece. The tool position was then zeroed. Contact between the pin and workpiece was known by a registered force of 44 N (10 lbf) or less on the dynamometer. Weld parameters were then adjusted to the values dictated by the DOE.

Each plunge was performed at a spindle speed of 500 rpm and a plunge rate of 12.7 mm/min. (0.5 in/min.). Programmed plunge depths were predetermined so that the tool depth near the end of the plunge was approximately that needed during the weld. The tool was then allowed to dwell for either 5 sec. if the Shoulder Depth for the weld was at a Low or Medium value, or 10 sec. if the Shoulder Depth was at a High value (to

allow the shoulder to further penetrate the workpiece surface). The spindle speed during each dwell remained at 500 rpm. After the dwell, the spindle speed was adjusted to the value dictated by the experimental design and the tool began to traverse at a rate of 51 mm/min. (2 in/min.). For the Medium and High Feed Rate values, the feed rate was then accelerated over a distance of 76 mm (3 in) until the desired feed rate was obtained. The tool traverse was performed at a constant Spindle Speed, Feed Rate, and Shoulder Depth as dictated by the experimental design. The extract sequence was performed at a spindle speed of 500 rpm.

The length of each weld varied depending on the Feed Rate. Since steady-state average values for the outputs were desired, it was also desired that the steady-state region for each weld be sufficient in length. To accomplish this, welds at the Low, Medium, and High Feed Rates were 254 mm (10 in), 559 mm (22 in), and 851 mm (33.5 in), respectively, in length, equating to at least 4 min. of data for each weld.

Although the FSW equipment automatically records various values as weld outputs, parameters of interest in the current study were X-force, Z-force, Pin Center Temperature, Root Temperature, Shoulder Temperature, Shoulder Depth (to insure that control was sufficiently accurate), and Motor Power. Motor Power refers to the amount of power required by the welder to turn the spindle under load, which includes the power required to overcome frictional losses. Additionally, IR image sequences were recorded for each weld at a frequency of 1 Hz. These IR sequences included all aspects of the weld including the plunge and extract sequences. The IR camera was frequently checked to ensure that it was level and that the distance between the tool and the front of the lens remained constant.

It should be noted here that during many of the experimental welds a significant amount of flash, or workpiece material that curls up from beneath the tool, would be generated. This flash would often scratch the tool surface near the shoulder, marring the paint coating. Just prior to each weld, the surface would be analyzed. If damaged, a light coating of paint would be reapplied to the surface by rotating the tool and using the corner of a paint brush to apply a new coat of paint. Only the portion of the tool surface that was marred was repainted.

2.4　Data Processing

2.4.1　Weld Process Data

Upon completion of the welds, the data (excluding the IR sequences) were analyzed using a spreadsheet. A preliminary analysis of the data was conducted to identify a steady-state region for each weld. Since the length of each weld varied as described above, some generalizations about the steady-state region for welds performed at each Feed Rate level were made by plotting the data for a select number of welds with respect to X-position and noting the approximate beginning and end of the steady-state region. The steady-state regions thus identified for welds performed at the Low, Medium, and High Feed Rate values began 76 mm (3 in), 203 mm (8 in), and 356 mm (14 in) into the weld, respectively, and ended 25 mm (1 in) before the extract location for welds performed at the Low Feed Rate value and 38 mm (1.5 in) before the extract location for welds performed at the Medium and High Feed Rate values. The selected outputs for each weld were then averaged over this region. A program was compiled to automate the
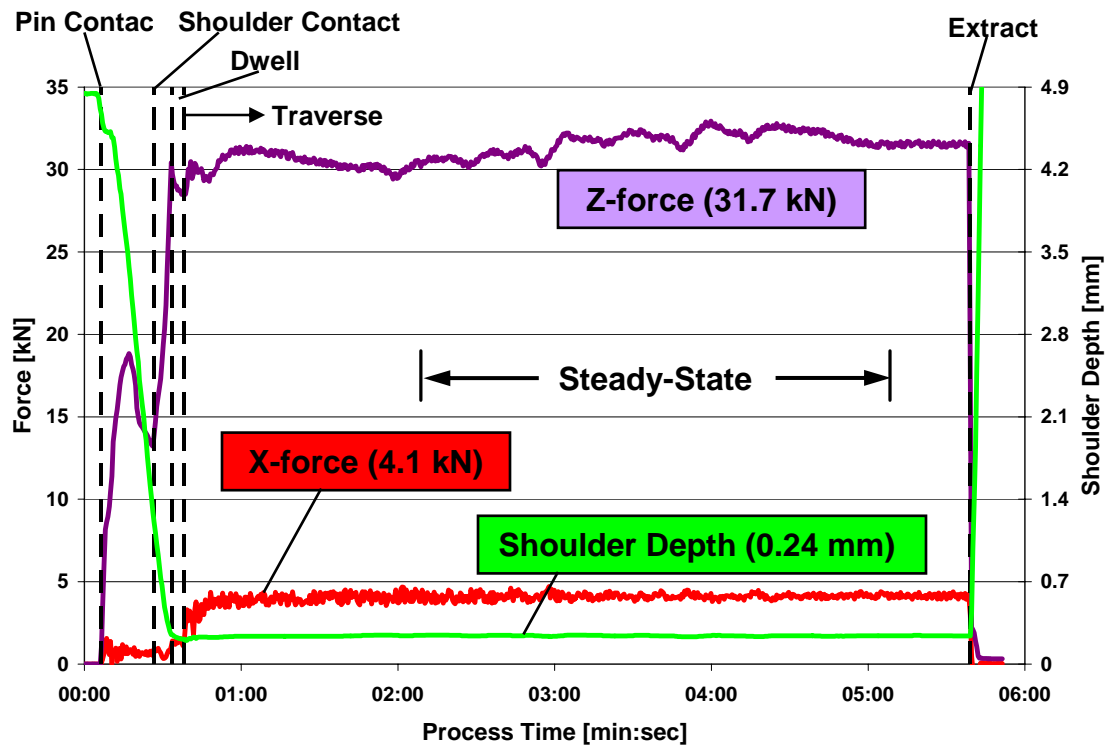
**Figure 9. Representative plot of weld process data (forces and Shoulder Depth)
for one of two welds performed at the LLL parameter combination.**

process for rapid extraction of the data. The steady-state average values for each output

were then compiled into a single summary worksheet.

Examples of the raw data obtained from a representative weld are shown in

Figure 9 and Figure 10. Data from one of two welds performed at the LLL process

parameter combination have been chosen for this purpose. It should be remembered that

the plots are only representative and that each weld will have its own unique set of

values. However, many of the trends that exist in the data will be quite similar. In Figure

9, X-force, Z-force, and Shoulder Depth are plotted versus weld time and in Figure 10 the

three tool temperatures (Pin Center, Root, and Shoulder) and the Motor Power are

plotted, also versus weld time. In each of the plots the significant process events of pin
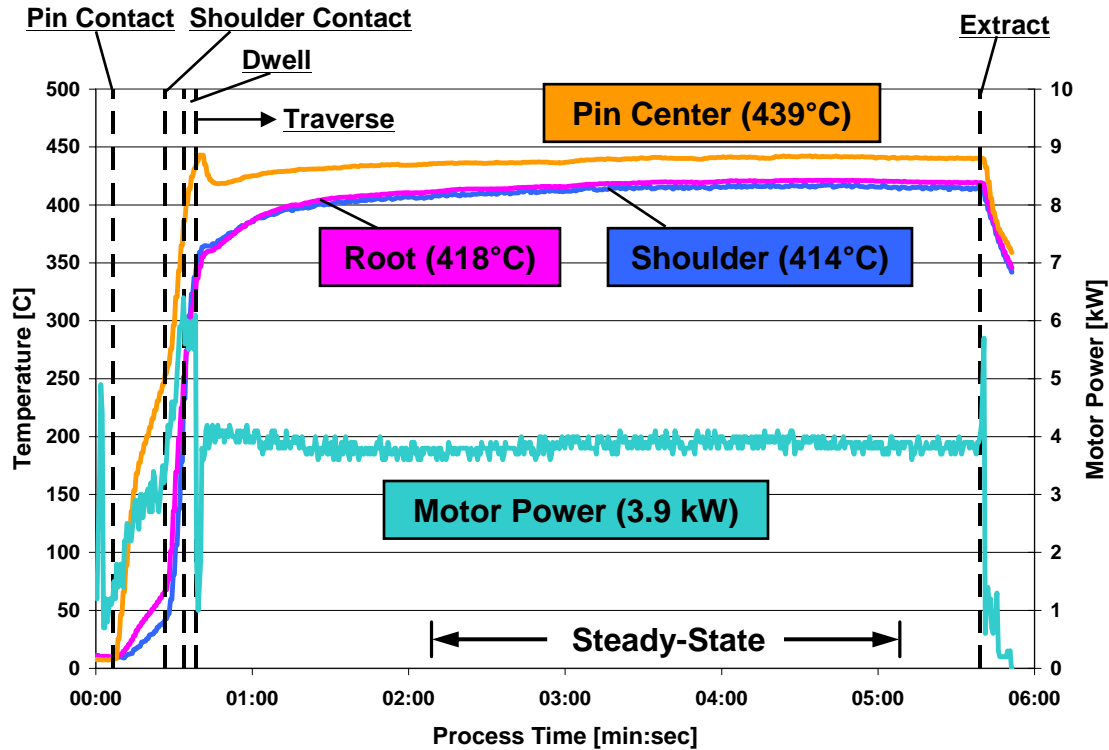
Figure 10. Representative plot of weld process data (tool temperatures and Motor Power) for one of two welds performed at the LLL parameter combination.

contact, shoulder contact, dwell, traverse, and extract are noted. The steady-state region

over which the outputs of interest have been averaged is also identified on each of the

plots and the calculated steady-state values for the outputs are included in the series

identification box.

It can be noted in each of the plots that the significant process events are readily

observed in the weld data. For example, in Figure 9, the Z-force increased sharply at he

pin was first brought into contact with the workpiece material. As heat was generated

around the pin, the material locally softened and the force began to decrease slightly.

Another steep rise was recorded as the shoulder came into contact. A slight decrease in

the Z-force was then measured as the material below the shoulder softened during the

dwell. It can also be noted in the figure that, during the traverse, the Shoulder Depth

fluctuated slightly about the control value of 0.24 mm. In Figure 10, the Pin Center

temperature was the first to increase from the initial condition of 10°C, which was

followed by a rise in the Root temperature as heat was conducted into the tool near this

location, and lastly by a rise in the Shoulder temperature, which did not rise significantly

until after shoulder contact. The Pin Center temperature remained the highest throughout

the weld. The trends are interesting and reveal much about the process.

Total Energy Input

Additional processing of the Motor Power data involved the subtraction of the

approximate power required to overcome losses to the machinery. In a separate

experiment, the free-wheel power required by the spindle motor at various spindle speeds

was measured (Table 2). The appropriate value was then subtracted from the steady-state

Motor Power value for each weld. Assuming that all of the mechanical power required

by the spindle goes into weld heating, an approximate Total Energy Input into each weld

was thus calculated. Since it is likely that the losses which occur while welding are

higher than at a free-wheel state due to the increased strain on the gears and bearings, it is

recognized that the free-wheel power measurements may be a lower limit for the losses

that actually occur during a weld.

Table 2. Approximate losses to the FSW machinery at various spindle speed levels.

Spindle Speed [rpm]	Losses [kW]	Spindle Speed [rpm]	Losses [kW]
200	0.25	550	1.22
250	0.34	600	1.37
300	0.43	650	1.52
350	0.53	700	1.58
400	0.69	705	1.62
450	0.88	750	1.65
500	1.04		

2.4.2 IR Data

Since the format of the IR data is quite unique, additional processing was required. As described above, the IR data comes in the form of an image, or sequence of images, of the entire field of view of the camera. However, it was desired to track the temperature of only a select portion of the image, namely the exterior surface of the tool, so that a steady-state temperature profile of the surface could be obtained. This was done by first identifying a pixel/mm scale for the image, using the known length of an object in the image (tool protruding from the tool holder) and identifying the pixels representing the object. The temperature at various locations spaced uniformly in a linear manner along the tool exterior surface (0.9 mm intervals, 27 locations along tool surface), including a portion of both the tool holder above and the workpiece below the tool, was then extracted for the sequence of IR images for a weld. A Visual Basic program was used to automate the process and place the data in a spreadsheet. Thus, at 27 different locations along the tool exterior surface, the temperature was known for each second of each weld.

A preliminary analysis of the data was then conducted to identify a steady-state region for the IR data. Interestingly, this preliminary analysis showed that the surface temperature of the tool required a longer period of time to reach a steady-state than the other data described above. Thus, the start of steady-state region for the IR data was defined as the point when the surface temperatures reached approximately 2% of their maximum value for the weld. This gave accurate steady-state average values for each measurement location. The steady-state region then ended approximately 10 sec. before the end of the weld. An example of the steady-state temperature profile for a weld performed at the LLL parameter combination is shown in Figure 11.
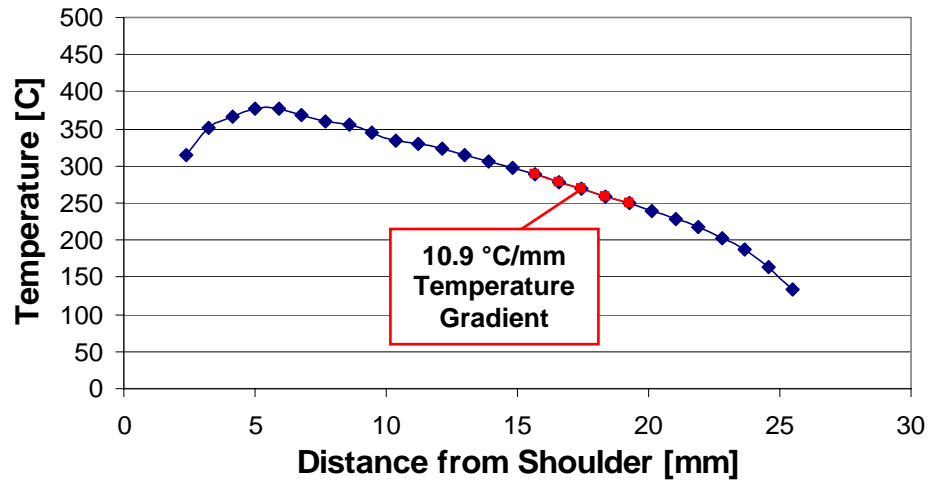
Figure 11. Steady-state surface temperature profile for a weld performed at the LLL parameter combination with accompanying linear-fit temperature gradient.

2.4.3 Heat Flow Calculation

Although the steady-state temperature profile for each weld would be useful for model comparisons, it was desired that the data be used to calculate the heat flow through the tool. The heat transferred by conduction through the tool can be calculated from Fourier's Law in the axial direction of the tool [Incropera, 2002]:

$$q_{cond} = -kA_C \, dT\!\!\Big/\!\!dz \tag{1}$$

where k [W/m-K] is the thermal conductivity of the tool (28 W/m-K), A_C is the cross-sectional area of the tool, and dT/dz is the temperature gradient along the tool. Thus, for each weld, a temperature gradient was identified. The location for the gradient was chosen for each weld by taking the 5 or 6 most linear points of the tool surface

31

temperature profile (maximum R^2 value for a linear fit) and determining the slope of the linear fit to be the temperature gradient (see Figure 11). The location of this gradient with respect to the shoulder was quite consistent for all welds and was located approximately 15 - 20 mm (0.6 – 0.8 in) above the shoulder. The heat flow through the tool was then calculated for each weld using Equation (1).

It may be noted that only a portion of the temperature profile is used for the heat flow calculation. In some cases the surface was so marred from the weld flash that temperature data near the shoulder was not available. However, the heat transfer physics of the process dictate that near the shoulder, where the temperatures are higher, the energy losses to the environment from convection and radiation are much greater. Thus, the temperature gradient along the entire surface is not expected to be linear, and a smaller region is used in the calculation of the heat conduction.

In using the surface temperature gradient of the tool to calculate the heat flow, an assumption is made that radial gradients through the tool are negligible. As will be shown hereafter, numerical modeling of the tool indeed confirms that these radial gradients are very small.

2.4.4   Tool Heat Input Calculation

Taking the tool as a control volume, it was assumed that, for steady-state FSW, the heat flow calculated from the IR data was the energy leaving the tool into the cooled tool holder and machine spindle. Noting that the area over which the heat flow was calculated was some distance from the shoulder, it was determined that radiative and convective losses to the environment must also be accounted for. Conservation of energy for the
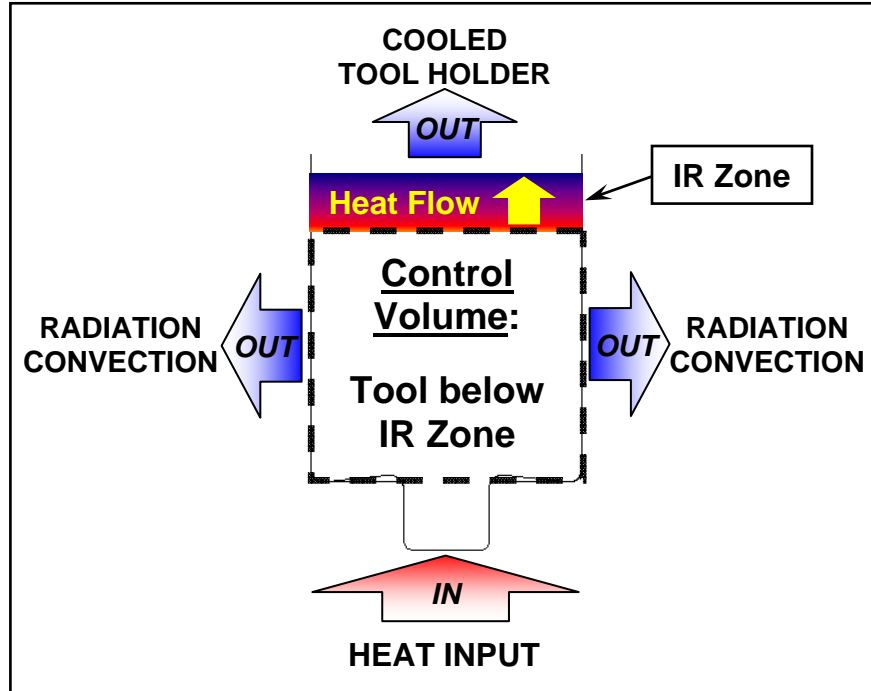
Figure 12. Diagram of control volume used for Tool Heat Input calculation.

control volume dictates that the sum of the energy leaving the tool equals the Tool Heat

Input (Figure 12).

Convective losses (q_{conv} [W]) were approximated by performing the following

integration over the area of the tool below the IR zone:

$$q_{conv} = \int h(T_z - T_\infty)Pdz \qquad (2)$$

where h [W/m^2-K] is the convection heat transfer coefficient, T_z is the local surface

temperature, T_∞ is the free stream air temperature (here assumed to be 24°C), and the

product Pdz is a differential area where P is the tool perimeter and dz is a differential

length along the tool surface. The values for T_z at various locations along the tool surface were approximated from the linear fit equations generated from the IR data.

Values for h at the different spindle speed settings were approximated using a relation from Kendoush [1996] where the average Nusselt number (Nu) for a rotating, isothermal cylinder in a static medium of unlimited extent is calculated from

$$Nu = 0.6366(Re_r Pr)^{\frac{1}{2}} \qquad (3)$$

where Re_r is the Rotational Reynolds number of the cylinder and Pr is the Prandtl number of the fluid ($Pr_{air}= 0.7$). The Rotational Reynolds number for each Spindle Speed level was calculated from

$$Re_r = \frac{D^2 \omega}{2\nu} \qquad (4)$$

where D and ω are the diameter [m] and rotational velocity [rad/sec.] of the cylinder and ν is the kinematic viscosity of the fluid ($\nu_{air} = 1.59 \times 10^{-5}\, m^2$/sec.), which equated to values of 423, 736, and 1054 for the three Spindle Speed levels of 200, 350, and 500 rpm, respectively. Since the relation presented for Nu was said to be valid for $Re_r > 1000$, the Nu values for the Spindle Speed levels of 200 and 350 rpm were extrapolated. It is also noted that the relation was formed for an isothermal cylinder, which is clearly not the case for FSW, but it was felt that this was the best approximation that could be made.

Similar to the convective losses, the losses due to radiation (q_{rad} [W]) were approximated by performing the following integration over the tool surface area:

$$q_{rad} = \int \varepsilon\sigma\left(T_z^4 - T_{surr}^4\right)Pdz \tag{5}$$

where ε is the emissivity of the tool surface, σ is the Stefan-Boltzmann constant (5.67 x 10^{-8} W/m^2-K^4), and T_{surr} is the temperature of the surroundings (again assumed to be 24°C). The convective and radiative losses were thus calculated and added to the heat flow calculations for each weld. The calculated Tool Heat Input data were then compiled into a spreadsheet.

2.4.5   Percent Energy Calculation

The percentage of the total mechanical power that entered the tool for each weld was another value of interest. This value, termed the Percent Energy, was calculated by dividing the Tool Heat Input by the Total Energy Input for each weld as derived from the corrected Motor Power values.

2.5   Statistical Analysis of the Data

In Minitab, the Tool Heat Input and Percent Energy data for each weld condition were entered into a spreadsheet that contained the corresponding welding parameters for each weld as well as other values needed for factorial design and regression analysis. The main goal of the statistical analysis was to develop a regression equation for both the Tool Heat Input and Percent Energy values, known as the responses. A regression equation would allow the responses to be calculated at any factor level and could also be

plotted, showing a visual representation which could be used to easily identify trends in the responses with respect to the input parameters.

2.5.1 General Statistics

A regression equation is a mathematical function that approximates the actual data of a given response and is a function of the input parameters. An example linear regression model which utilizes two input parameters is of the form

$$\hat{Y}(X_1, X_2) = \beta_0 + \beta_1 X_1 + \beta_2 X_2 + \beta_4 X_1 X_2 \qquad (6)$$

where $\hat{Y}$ is the predicted response value as a function of the input parameters, X_{1-2} are the input parameters, β_0 is a term known as the intercept, and β_{1-4} are the coefficients. Products of the input factors, such as $X_1 X_2$, denote interactions between input parameters, which may describe how the effect of an input on the response changes depending on the level of another input. If a non-linear model is desired, additional terms such as X_1^2 and X_2^2 will be included.

The statistical software package is utilized to generate the values of the coefficients for the equation. The goodness-of-fit of the equation is measured by a value known as the R^2-adjusted (R^2-adj) value, which ranges from 0 to 100%, with 100% being a perfect fit, meaning that 100% of the variability in the data is explained by the equation. Thus, a higher R^2-adj is desired.

How well the equation predicts a response at a given factor level may also be analyzed by calculating the residual (R_i), or the error, at that level, which is defined as

$$R_i = Y_i - \hat{Y}_i \tag{7}$$

where Y_i and $\hat{Y}_i$ are the measured and predicted response values at the parameter level. A

complete analysis of the residuals for a given regression model is necessary to validate

assumptions inherent in the regression analysis and to strengthen model validity.

However, plots of the residuals can also indicate how closely the model predicts the data

and declare it as valid for data prediction. As the statistical analysis of the data is not the

focus of the current work, background on residuals and analyses performed for the

current work are included in the Appendix.

2.5.2 Analysis Procedure

A preliminary analysis of the data was first performed, which included a DOE factorial

design analysis to determine which terms were significant using a linear regression

model. Since the analysis uses a linear model, squared terms are not included. Plots

known as main effects plots were then generated and analyzed (Figure 13). As seen in

the figure, main effects plots show the dependence of the outputs (Tool Heat Input and

Percent Energy) on the inputs (Spindle Speed, Feed Rate, Shoulder Depth). Each data

point represents the average of the data over all of the welds performed at a given

parameter level. Simple trends in the data can thus be seen. If a factor were to have little

or no effect on an output, the line would be horizontal. If a factor were to have a linear

effect, a slanted line joining the three points would be displayed, where a steeper line

would indicate a greater effect. Simple nonlinear effects may also be seen, showing that
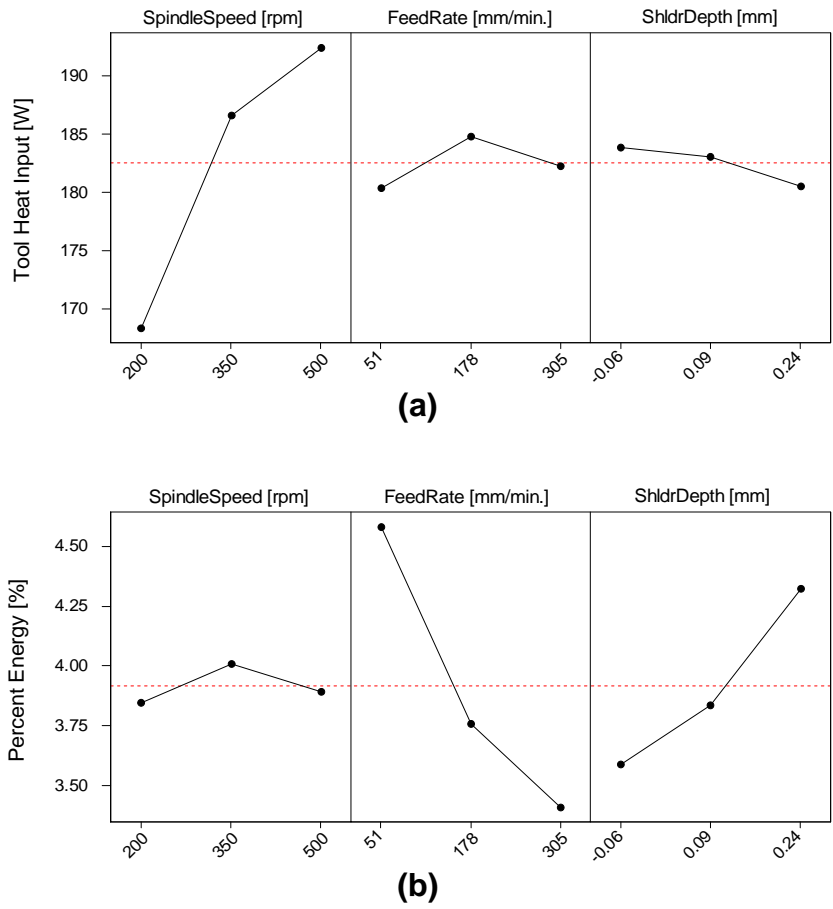
Figure 13. Main Effects Plots (data means) produced during the preliminary factorial design analysis: (a) Tool Heat Input; (b) Percent Energy.

squared terms for a given factor may need to be included in a regression model for good correlation with the data. Thus, from the analysis of the main effects plots shown in Figure 13 it was apparent that the outputs were non-linear functions with respect to some or all of the input factors (see for example Figure 13(a), Feed Rate factor).

Multiple regression analysis cases, each including different combinations of terms, were then performed which gave various regression models. As the main effects plots gave some indication that squared terms may be important, these were especially included in the regression analysis. For each case, the R^2-adj term was noted as well as

trends in the various residual plots available from Minitab. A decision regarding the best regression model for the Tool Heat Input and Percent Energy data was then made by choosing the model with the highest R^2-adj value that accurately reflected trends in the data. The residual analysis proved that the models were sound and adequately predicted the data. The regression models were then plotted and trends with respect to the three input parameters were noted. The regression equations were also available to predict the Tool Heat Input and Percent Energy at any parameter level within the operational window used with reasonable accuracy.

2.6   Uncertainty Analysis

Some quantification of the experimental uncertainty associated with the internal temperature measurement of the tool and calculation of the Tool Heat Input may best be presented here. Additional insight into the results presented hereafter may be gleaned from this analysis. Typical calibrated accuracy of thermocouples is $\pm 1°C$. However, in this application, the uncertainty in the temperature measurement (u_T) can be more appropriately estimated by

$$u_T = u_z \, dT\!\big/\!dz \tag{8}$$

where u_z is the uncertainty in the location of the temperature measurement (in mm) and dT/dz is the average temperature gradient along the tool (in °C/mm). Choosing u_z to be half of the diameter of the thermocouple probe sheath (0.08 mm) and dT/dz to be 11.6 °C/mm, the uncertainty in the temperature measurement is approximately 9°C.

As previously described, the Tool Heat Input was calculated by summing the heat flow through the tool and the heat losses to the environment and can be represented as

$$Q_{tool} = -k\pi R_o^2 \, dT/dz + q_{env} \qquad (9)$$

where R_o is the outer diameter of the tool and q_{env} is the heat transferred to the environment by both convection and radiation. Using the root-sum-squares (RSS) method [Figliola, 2000] the uncertainty in the Tool Heat Input calculation $\left(u_{Q_{tool}}\right)$ can be calculated from

$$u_{Q_{tool}}^2 = \left(u_k \frac{dQ_{tool}}{dk}\right)^2 + \left(u_{R_o} \frac{dQ_{tool}}{dR_o}\right)^2 + \left(u_{dT/dz} \frac{dQ_{tool}}{\left(dT/dz\right)}\right)^2 + \left(u_{q_{env}} \frac{dQ_{tool}}{dq_{env}}\right)^2 \qquad (10)$$

where u_k, u_{R_o}, $u_{dT/dz}$, and $u_{q_{env}}$ are respective uncertainties of the thermoconductivity of the tool steel, the radius of the tool, the axial temperature gradient along the tool, and the losses to the environment. The percent uncertainty in the Tool Heat Input $\left(u_{Q_{tool}}/Q_{tool} * 100\right)$ can then be calculated from

$$\left(\frac{u_{Q_{tool}}}{Q_{tool}}\right)^2 = \left(\frac{u_k}{k}\right)^2 + \left(\frac{2u_{R_o}}{R_o}\right)^2 + \left(\frac{u_{dT/dz}}{dT/dz}\right)^2 + \left(\frac{u_{q_{env}}}{Q_{tool}}\right)^2. \qquad (11)$$

40

When values for the thermoconductivity, tool radius, and temperature gradient of 28 ± 1 W/m-K, 12.7 ± 0.2 mm, and 11 ± 1 °C/mm, respectively (shown with their respective uncertainties), are chosen, an uncertainty of 5 W is assumed for the losses to the environment, and an average Tool Heat Input of 182.5 W is assumed for Q_{tool}, the percent uncertainty in the Tool Heat Input calculation is 10%.

3 Numerical Tool Models

A 2-dimensional axisymmetric numerical model of conduction heat transfer in the tool was developed. Every effort was made to accurately represent the conditions of the experiments described above. The heat input to the tool was applied in various configurations to investigate the true manner of tool heating.

3.1   General Characteristics

3.1.1   Geometry

The model was dimensionally accurate to the tool used in the experiments. Pro-Engineer modeling software was used to produce a 2-D model of the tool. Thus, the difficult portions of the tool to model, such as the rounds and the angle of the shoulder concavity, were accurately represented in a 2-D space. Threads on the pin were omitted for simplicity and the outer diameter of the pin was assumed to be the major diameter of the threaded pin used in the experiments (7.9 mm (0.31 in)). The thermocouple passages were also neglected.

3.1.2   Solution Method

From Pro-Engineer the model was exported as an .IGS file to Gambit for the creation of the mesh. Quadrilateral elements were used and the nodes for the mesh were placed in such a manner that a higher grid density was present near the tool/workpiece interface

where high temperature gradients were likely to occur. The mesh was then exported for

the heat conduction simulations which were performed using FLUENT, a commercially

available Computational Fluid Dynamics (CFD) software package. FLUENT utilizes a

control volume approach for calculating a variety of outputs, all dependent on the

prescribed boundary conditions as defined by the user. Although FLUENT is readily

capable of numerical simulations that involve complex fluid flow and heat conduction,

only the heat conduction analysis capabilities were needed.

Each of the simulations was performed in FLUENT until convergence, with a

numerical residual of 1×10^{-8} being the convergence criteria. Although numerical

residuals this small were never achieved, this allowed the simulations to continue until no

further variation in residual magnitude was detected. Predicted temperature contours of

the tool were generated and the predicted temperatures at the three thermocouple

locations (Pin Center, Root, and Shoulder) were noted for each case and were compiled

into a spreadsheet with the experimental data. Steady-state tool temperature values of the

two experimental welds performed at the same process parameter combination were then

averaged. The predicted temperatures were then compared with the average experimental

temperature at the parameter combinations simulated and conclusions were drawn.

3.1.3   Thermal Conductivity

It was desired that the thermal conductivity of the tool material (heat-treated H13 tool

steel) be properly represented in the numerical model. Typically this involves some

characterization of the thermal conductivity as a function of temperature. Research into

this value yielded a variety of different distributions, none of which complimented one

another. Since one distribution could not be justified over another, it was determined that

44

a constant value of 28 W/m-K would be assumed for the model. The various distributions and their corresponding references are shown in the Appendix.

3.1.4 Grid Independence Study

Proper numerical modeling strategies require that a grid-independence study be conducted to insure that the predictions produced by a given model are accurate and independent of grid density. The grid independence study for these experiments was conducted on models of the tool used during preliminary process window identification studies (6.4 mm (0.25 in) pin length). All other dimensions were the same as those for the tool used in this study. Six different meshes were produced, each with a slightly greater mesh density than the previous, ranging from 464 nodes to 5153 nodes. Solutions were then generated in FLUENT using each mesh and values such as the predicted maximum temperature and the temperatures at each of the three thermocouple locations were monitored and plotted versus the total number of nodes. Interestingly, although the grid density was increased by a factor greater than 11, the solution values changed by 1% or less. Thus, it could be assumed that the highest mesh density was not required for an accurate solution. However, since the computation time for each simulation was less than one minute, even with a high grid density, little advantage was gained from using a lower mesh density and the highest was adopted. Since the simulations required such a short time, the mesh density was further increased near the tool holder when the model for the current study was produced so that temperatures throughout the tool, and not just near the tool/workpiece interface, could be accurately resolved. When completed, the mesh consisted of 6362 nodes, corresponding to 6114 quadrilateral elements.

3.2 Boundary Conditions

A diagram showing the boundary conditions used for the model is shown in Figure 14.

As seen in the figure, the model is axisymmetric. The heat input is applied as a heat flux

(i.e., heat energy per unit area [W/m^2]) along the portion of the tool in contract with the

workpiece during welding. Three different heat flux spatial distributions were used and

will be described hereafter in Section 3.3.

The portion of the tool exposed to the environment was modeled as a mixed

boundary condition, which incorporates the effects of both radiation and convection heat

transfer from the surface to the environment. Values used to define these conditions were

a room temperature of 24°C for both T_∞ and T_{surr} and a value of 1.0 for the surface

emissivity. Values for the convection heat transfer coefficient were functions of the

spindle speed and were, again, taken from the work by Kendoush [1996]. The values
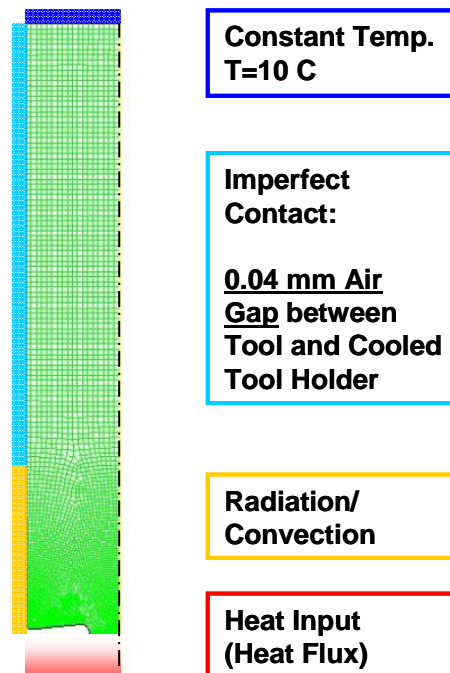
Figure 14. Numerical Boundary Conditions used.

used were 11, 15, and 18 W/m²-K for the three Spindle Speed values of 200, 350, and 500 rpm, respectively.

Due to the high cooling capacity of the cooled tool holder, boundary conditions for the portion of the tool inserted into the tool holder (two boundaries) were both originally modeled as constant temperature boundary conditions at the temperature of the coolant (10°C). However, model comparisons with the IR data from preliminary studies showed that this may not be the case. It was then deduced that, although the top of the tool may indeed have very good contact due to the high axial force that exists while welding, justifying a constant temperature boundary condition there, the side of the tool does have some clearance in the tool holder which allows the tool to be inserted and removed freely. The contact was then assumed to be imperfect and modeled as a small air gap of width *w*. An overall heat transfer coefficient was then calculated assuming the only mode of heat transfer between the tool and the tool holder at this location to be heat conduction through the air present in the gap. The boundary was then modeled as a convection boundary condition where the heat transfer coefficient (h_{gap} [W/m²-K]) was calculated as

$$h_{gap} = \frac{k_{air}}{w} \qquad (12)$$

where k_{air} is the thermal conductivity of air (0.03 W/m-K). The heat transfer coefficient for various air gap widths within the range of 0.03-0.08 mm (0.001-0.003 in) was calculated and implemented in trial models. A gap width of 0.04 mm (0.0015 in) was determined to yield the best results.
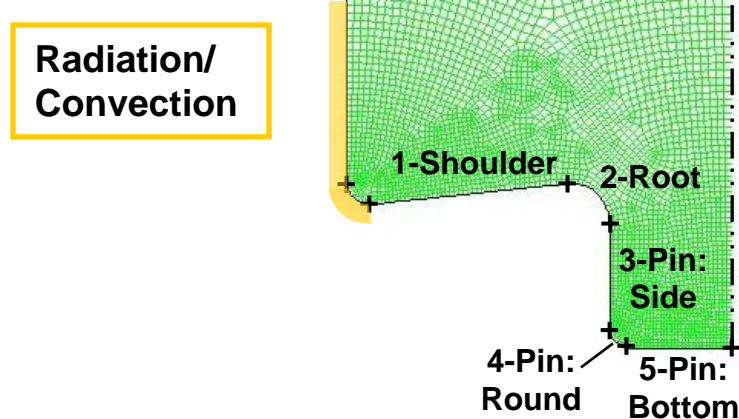
Figure 15. Tool/workpiece interface detail of numerical model showing zone designations.

3.3 Heat Input Implementation

Although the Tool Heat Input value for each weld had been characterized from the experimental data, it was desired to further investigate not only the heat input value, but its spatial distribution along the tool/workpiece interface for steady-state FSW. Three different heat input distributions were thus investigated and are outlined below.

A detailed diagram of the model near the tool/workpiece interface is shown in Figure 15. It is seen here that the interface area for the model is divided into five different zones, as defined by the geometry of the model. Each zone is comprised of cells which are defined by the nodes of the numerical model. Thus, the Tool Heat Input may be applied either equally to each of the cells of a given zone, giving a uniform heat input, or at different magnitudes for each cell, representing some spatial variation that may occur in tool heating during FSW.

The heat flux value for each zone is calculated by means of a User Defined Function (UDF) in FLUENT. A UDF is the manner in which FLUENT can be tailored to

a specific problem by the user and is essentially a C-program which is compiled during

the simulation that uses FLUENT-specific functions. In this manner a value such as the

heat flux need not be spatial uniform in a zone, but can vary with the position of a cell

within the zone. Many functions are available to modify FLUENT for accurate

prediction of a variety of situations. Examples of the User Defined Functions used for

each of the three heat input distributions discussed hereafter are found in Appendix.

3.3.1 Radially Varying Heat Input

The accuracy of applying the heat input in a fashion similar to that already reported in the

literature was investigated. This radially varying heat input (q''_{RV}) was therefore derived

in a similar fashion and converted to a heat flux of the form

$$q''_{RV}(r) = \frac{\eta \mu F_n 2N}{(R_o^2 - R_i^2)} r \qquad (13)$$

where η is the percentage of the total heat flux that is imposed on the tool, μ is the

coefficient of friction, F_n is the normal force (z-direction), N is the machine spindle speed

[rev/sec.], r is the radial position, and R_o and R_i are the outer and inner radii of the tool

shoulder, respectively. F_n and N were experimentally measured values. The value for μ

was arbitrarily set to 0.3 and the value for η was adjusted until the Tool Heat Input

approximately matched that calculated by the regression equation for a given set of weld

input parameters. As it has been assumed in the above equation that the shoulder bears

the normal force, thus being the primary source of heat generation, the heat flux was

applied solely along the shoulder region (zones 1:Shoulder and 2:Root in Figure 15).

Four different parameter combinations were tested using this method to investigate general trends when increasing Spindle Speed and Feed Rate at a constant Shoulder Depth. The Shoulder Depth value used was assumed to be the High condition, or the deepest weld. It was felt that in this condition the assumption of the entire shoulder, and not just a portion of it, bearing the normal force was better reflected. The four parameter combination cases are summarized in Table 3.

Table 3. Four parameter combinations tested using the radially varying heat input.

Case	Spindle Speed	Feed Rate	Shoulder Depth
1	L	L	H
2	L	H	H
3	H	L	H
4	H	H	H

3.3.2   Uniform Heat Flux

Simulations of welds performed at each of the 27 different parameter combinations were developed where the Tool Heat Input was calculated using the regression equation and applied as a uniform heat flux along the entire interface. The heat flux calculation for each zone ($q''_{U,i}$), which was then applied individually at each cell, can be represented as

$$q''_{U,1-5} = \frac{Tool\ Heat\ Input}{A_1 + A_2 + A_3 + A_4 + A_5} \tag{14}$$

where A_i is the area of each zone as calculated by FLUENT. Since the model was axisymmetric in nature, FLUENT was able to calculate the area that would exist by revolving the given 2-D geometry about the axis of symmetry.

3.3.3 Distributed Heat Flux

Again, at each of the 27 different parameter combinations, the regression equation was used to calculate the Tool Heat Input. The heat input here, however, was applied in a distributed manner along the interface. The heat flux for each zone ($q''_{D,i}$) was calculated as

$$q''_{D,i} = \frac{\eta_i \ Tool \ Heat \ Input}{A_i} \tag{15}$$

where η_i is the fraction of the total Tool Heat Input imposed on a given zone, which varied from zone to zone. The optimal η value for each zone was discovered using an iterative approach at the LLL parameter combination where the η values were adjusted until the difference between the predicted and experimental temperatures (T_{pred} - T_{exp}) at each thermocouple location were minimized. The η values then remained the same for the remaining 26 simulations.

4 Results/Discussion

4.1 Experimental Data

4.1.1 Weld Process Data

A comprehensive summary table containing steady-state average values for the responses of interest for each of the welds performed in this study is included in the Appendix. However, plots of the data are shown here for convenience. In Figure 16, X-force and Z-force are shown, plotted versus process parameter combination. In Figure 17, the three tool temperatures are similarly displayed and in Figure 18 the Motor Power data are plotted, also versus process parameter combination.

An analysis of the steady-state process data over the entire operational parameter window shows that the steady-state average X-force ranged between 3.3 kN and 10.7 kN. Forces in the vertical direction (Z-force) ranged between 27.4 kN and 70.2 kN. Temperatures at the Pin Center, Root, and Shoulder locations had the respective ranges of 371°C to 507°C, 371°C to 480°C, and 378°C to 478°C and the steady-state Motor Power values ranged between 3.9 kW and 7.6 kW. The maximum range values listed for the tool temperatures and the Motor Power occurred at welds performed at the High Spindle Speed factor, while X-force and Z-force were more dependent on factor levels of Feed Rate and Shoulder Depth, respectively.
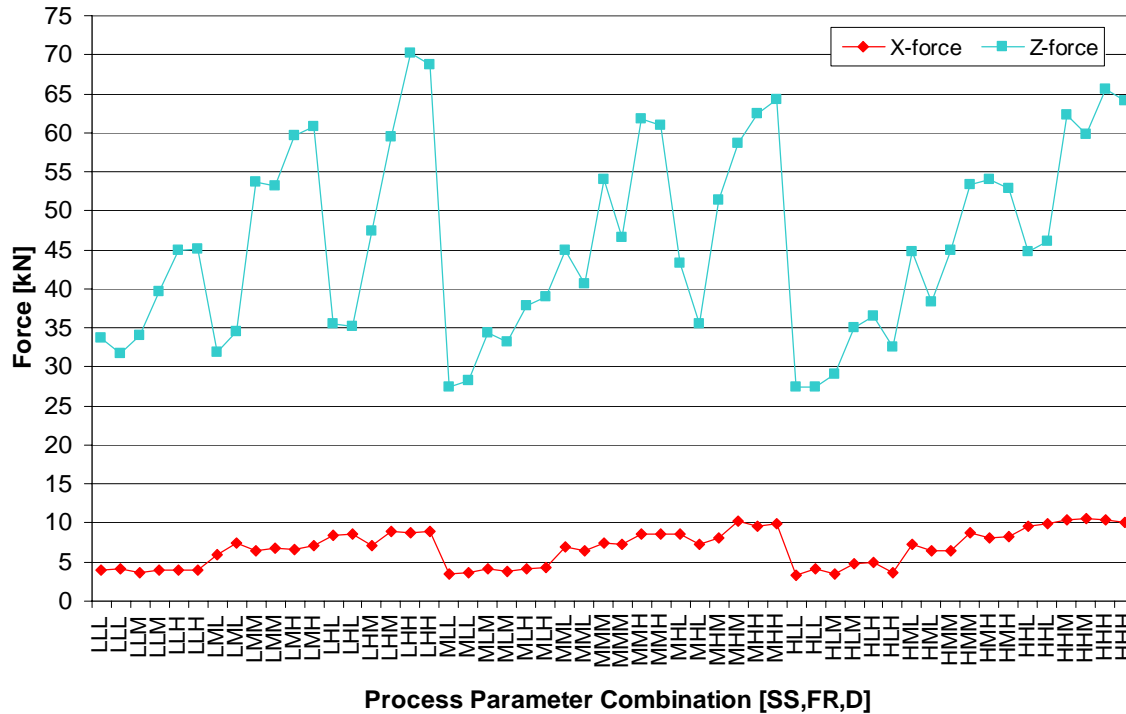
Figure 16. Steady-state force data for all welds plotted versus process parameter combination.
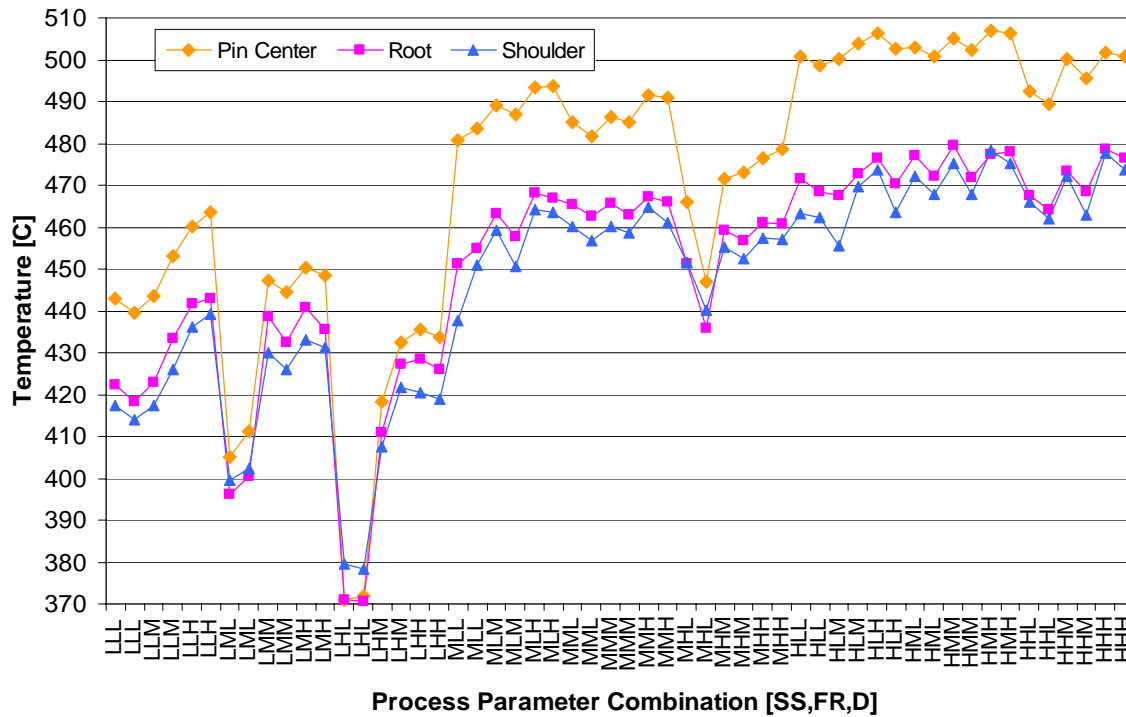
**Figure 17. Steady-state tool temperature data for all welds,
plotted versus process parameter combination.**
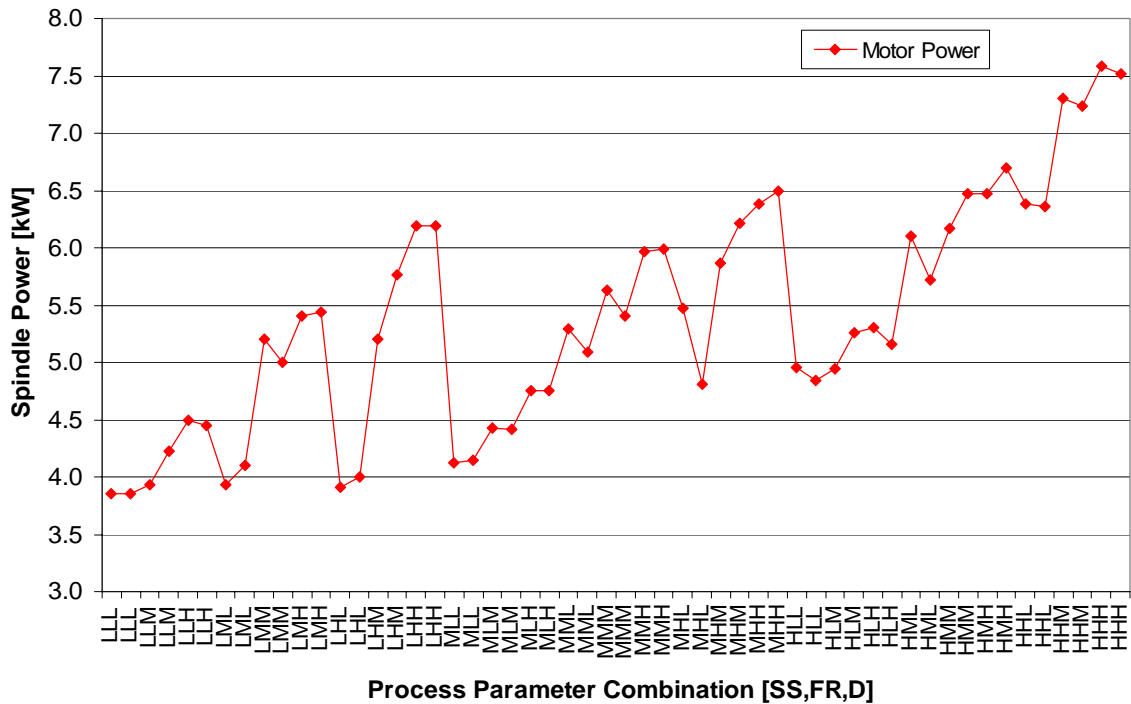
**Figure 18. Steady-state Motor Power data for all welds,
plotted versus process parameter combination.**

Of interesting note in a thermal sense is that the measured Pin Center temperature was greater than the measured Root temperature for all of the 54 welds performed. For 52 of the 54 welds performed the Pin Center temperature was also greater than the Shoulder temperature. The Shoulder temperature was greater than both the Pin Center and Root temperatures during the two welds performed at the LHL parameter combination. There were two other parameter combinations, namely the LML and MHL, where, for both welds performed, the steady-state average Shoulder temperature was greater than the steady-state average Root temperature.

4.1.2 IR Data

A representative IR image for the weld data featured in Figure 9 and Figure 10 is shown in Figure 19 (LLL parameter combination). The image was taken approximately 4 min. 30 sec. into the weld, which is well into the steady-state region. The color palette on the right of the figure indicates the approximate surface temperature of the objects in the field of view of the camera in degrees Celsius. A portion of the image has been cropped so that that the surface temperature of the tool is more apparent. As seen in the figure, the image is quite clear and a temperature distribution on the tool surface is apparent, showing a decreasing trend from the shoulder upwards to the cooled tool holder. The highest temperatures in the image are measured near the tool shoulder. Although the higher temperatures that exist on the exterior surface of the tool cause the tool to be the most apparent object in the image, the outlines of other objects can also be seen and are noted on the figure. It can also be seen that the IR radiation is reflected in the workpiece just in front of the tool.
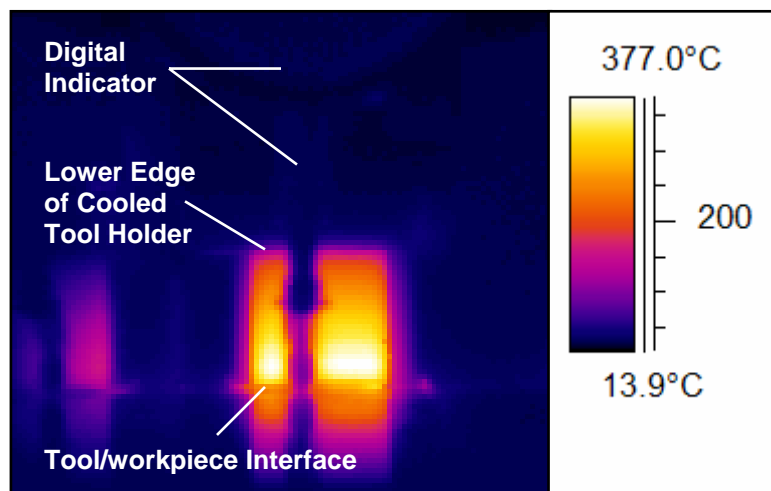
Figure 19. Representative steady-state IR image for a weld performed at the LLL parameter combination.

The surface temperature data extracted from the sequence of images from which this image was obtained is shown in Figure 20. Although the tool surface temperature data was extracted at 0.9 mm intervals, resulting in 27 different locations along the tool surface, the temperature at only three of the locations is shown here for simplicity, plotted versus weld time. An IR image is also shown in the figure and the approximate locations of the temperature traces are indicated. The tool surface temperature was initially near 10°C, which was the temperature of the coolant flowing through the cooled tool holder. The surface temperature then increased over time as heat was generated during the weld and conducted through the tool. There was very little fluctuation in the temperature at each location throughout the weld and temperature decreased with increasing distance from the tool shoulder. A steady-state surface temperature was eventually reached. The steady-state region used for this IR image sequence is shown in the figure as well as the
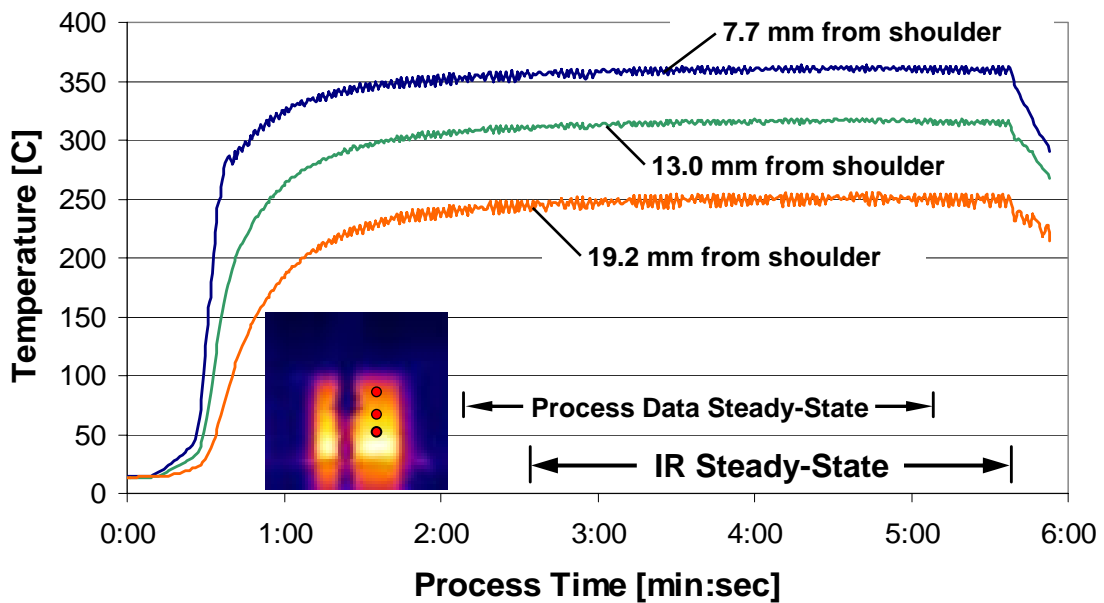
Figure 20. Tool surface temperature at three locations above the shoulder extracted from the IR image sequence for one of the welds performed at the LLL parameter combination.

57

steady-state region used for the weld data (see Figure 9 and Figure 10). When the two

regions are compared it is apparent that a greater time was required for the surface

temperature to come to a steady-state. However, the IR steady-state region was not

shorter that used for the weld process data since the region extends to near the end of the

weld. As discussed in Section 2.4.2, the temperature extracted for each location was then

averaged over the steady-state region, giving a steady-state temperature profile for each

weld.

A plot showing the steady-state tool temperature values for the same weld is

shown in Figure 21. The linear fit of temperatures from which the temperature gradient

was calculated is also shown. It is again noted that, although the surface temperature

gradient is quite linear, it is not expected to be entirely linear, and only a portion of the

temperature gradient is used for the heat flow calculation. As stated previously, an

approximation of the surface temperature profile was also used in calculating energy

losses to the environment from radiation and convection. Thus, by summing the heat
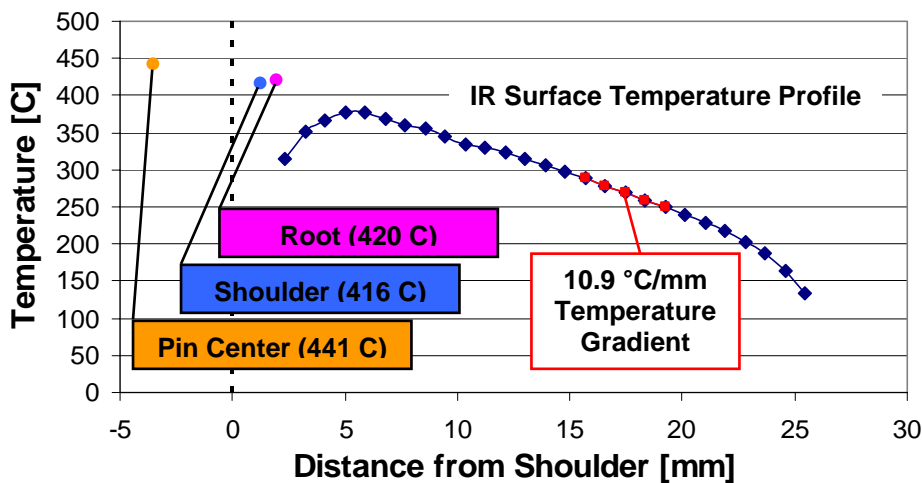
**Figure 21. Tool temperature data obtained for one of the welds
performed at the LLL parameter combination.**

58

flow through the tool (which flows into the machine head and cooled tool holder) and the

energy losses to the environment, the Tool Heat Input was obtained for each weld. The

fraction of the Total Energy Input that entered the tool, or the Percent Energy value, was

then quantified. A table containing these values for each of the welds is found in the

Appendix. However, a summary table providing the minimum and maximum value for a

variety of the calculated values is presented here for convenience as Table 4.

As noted in the summary table, over the entire range of operating parameters the

Total Energy Input varied from 3.60 kW to 6.54 kW. The range of calculated Tool Heat

Input values was 156 W to 200 W, accounting for 2.8% to 5.1% of the Total Energy

Input. However, it should be noted that the minimum and maximum Tool Heat Input and

Total Energy Input values occur at different welding parameters and thus cannot be used

to calculate the minimum and maximum Percent Energy. It is also interesting to note that

the energy losses to the environment below the axial conduction measurement location

imaged by the IR camera due to radiation were greater than those due to convection for

every weld. The total losses to the environment comprised 6% to 10% of the Tool Heat

Input, making them significant to the current study.

Table 4. Experimental minimum and maximum energy values.

	SS Motor Power [kW]	Total Energy Input [kW]	Temp. Gradient [C/mm]	Convective Losses [W]	Radiative Losses [W]	Tool Heat Input [W]	Percent Energy [%]
MIN	3.86	3.60	10.06	3.1	6.3	155.5	2.8
MAX	7.58	6.54	12.71	6.6	11.6	200.2	5.1

4.1.3 Regression Equations

The regression equation generated for the Tool Heat Input was

$$
\begin{aligned}
Q_{tool} = {} & 123.6 + 0.26 * SS + 0.09 * FR - 0.37 * FR * D + \\
& 9.05 \times 10^{-4} * SS * FR * D - 2.19 \times 10^{-4} * FR * FR - \\
& 2.77 \times 10^{-4} * SS * SS
\end{aligned}
\tag{16}
$$

where *SS*, *FR*, and *D* represent the value of the input factors (in rpm, mm/min., and mm, respectively). Thus, the Tool Heat Input at the LLL parameter combination (*SS*=200 rpm, *FR*=51 mm/min., *D*=0.24 mm) was calculated to be 166 W and could be calculated in a similar fashion at any parameter combination. The regression equation fit the data with a R^2-adj value of 84.2%. Magnitudes of the residuals that were calculated at all of the 54 welds were less than 10 W, with an average of 3.7 W. The range of the actual data was trends in the actual weld data are reflected quite well by the model.

Similarly, the Percent Energy value can be calculated from the following regression equation:

$$
\begin{aligned}
\eta_{tool} = {} & 3.66 + 5.95 \times 10^{-3} * SS - 7.56 \times 10^{-3} * FR - \\
& 8.31 \times 10^{-6} * SS * FR + 6.4 \times 10^{-3} * FR * D - \\
& 6.17 \times 10^{-6} * SS * SS + 1.48 \times 10^{-5} * FR * FR + \\
& 6.69 * D * D
\end{aligned}
\tag{17}
$$

which had an R^2-adj value of 94.3%. Magnitudes of the residuals calculated for this model were less than 0.3%, with an average value of 0.1%. The range for the actual data was 2.8-5.1%, and the range predicted by the regression equation was 2.8-5.0%.

It is apparent in the equations that the three independent variables are the process operating parameters. By plotting the regression equations, trends with respect to the input parameters can be visualized. Since plotting the equations would require a four-dimensional space, a sequence of plots must be used to fully visualize the effects of the three input parameters.

Sequences of plots for the Tool Heat Input and Percent Energy are presented in Figure 22 and Figure 23, respectively. In Figure 22, the dependent variable Tool Heat Input is plotted as a function of Spindle Speed and Feed Rate, and the three plots in the sequence represent the three factor levels for Shoulder Depth, where a Shoulder Depth value of 0.24 mm (Low factor level) is weld with the lowest shoulder penetration, or a shallow weld, and a Shoulder Depth value of -0.06 mm represents a deep weld performed at the High factor level (highest shoulder penetration). In Figure 23, the dependent variable Percent Energy is plotted as a function of Feed Rate and Depth, and the three plots in the sequence represent the three Spindle Speed levels. The independent variables along the X- and Y-axes in the two figures are different so that the most interesting trends with respect to the input parameters are visible.

The Tool Heat Input is clearly a function of the input parameters. In general, the Tool Heat Input increases with increasing Spindle Speed regardless of the Shoulder Depth level. A second-order dependence on Spindle Speed can be seen, and it is apparent that the Tool Heat Input is almost asymptotic in nature at higher Spindle Speed

61
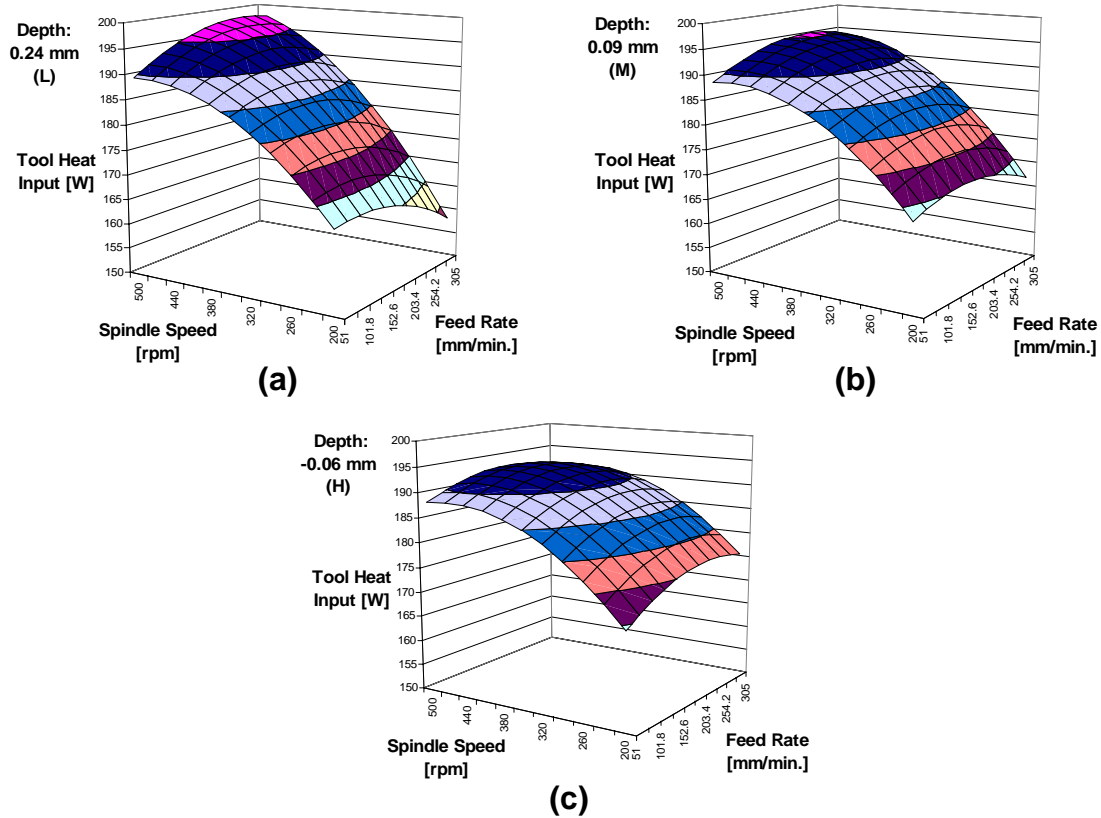
Figure 22. Tool Heat Input regression equation plotted versus Spindle Speed and Feed Rate at different Shoulder Depth values: (a) 0.24 mm (L); (b) 0.09 mm (M); (c) -0.06 mm (H).

values. Although this asymptotic behavior could be a local maximum of some sort (see Figure 22(c)), it should be remembered that sound welds were not produced at parameter combinations outside of the identified process window (i.e., Spindle Speed values greater than 500 rpm) for the chosen tool and workpiece combination. A second-order dependence on Feed Rate is also seen at any given Shoulder Depth level and remains fairly constant, reaching a local maximum near the Medium Feed Rate level. There is also a dependence on Shoulder Depth that can be seen as the surface shifts between each of the plots. In Equation (16) it is seen that the effect of Shoulder Depth is included in the interaction terms of the equation and that the D*D term is not included.

The asymptotic nature of the Tool Heat Input is reminiscent of the behavior of the heat generation in FSW. The workpiece near the tool is softened to such an extent at the higher Spindle Speed values that heat can no longer be generated and a heat generation limit is approached. As a heat generation limit is approached, the Tool Heat Input is similarly limited, and the asymptotic nature is observed.

The surface contour plotted in Figure 22(a) at the Low Shoulder Depth factor level is unique compared to the plots in Figure 22(b) and (c). The surface is quite steep and is not as asymptotic in nature. The surface is also unique in that the surface stretches between both the minimum and maximum values of the Tool Heat Input. It should also be noted in Figure 22(b) and (c) that the second-order dependence on Feed Rate at the higher Spindle Speed values causes the surface to curve down slightly toward the rear corner of the plot area and out of view when looking from the current perspective.

In Figure 23, it can be seen that the Percent Energy increases with decreasing Feed Rate and decreasing shoulder penetration (i.e., from High (-0.06 mm) to Low (0.24 mm) Should Depth). Thus, higher Percent Energy values are found at parameter combinations that involve a Low Feed Rate and Low Shoulder Depth. A second-order dependence on both input parameters is seen in each of the plots. Although there is also a second-order dependence on Spindle Speed, the effect was quite small when compared to that of the other two variables. The dependence on Spindle Speed is noted here as the surface shifts between each of the plots. Of note is that at the High Spindle Speed factor level, both the minimum and maximum values for the Percent Energy are achieved. It is also interesting that, in each of the plots, the second-order dependence on Shoulder Depth varies with the Feed Rate value. Although the actual range of values may seem quite
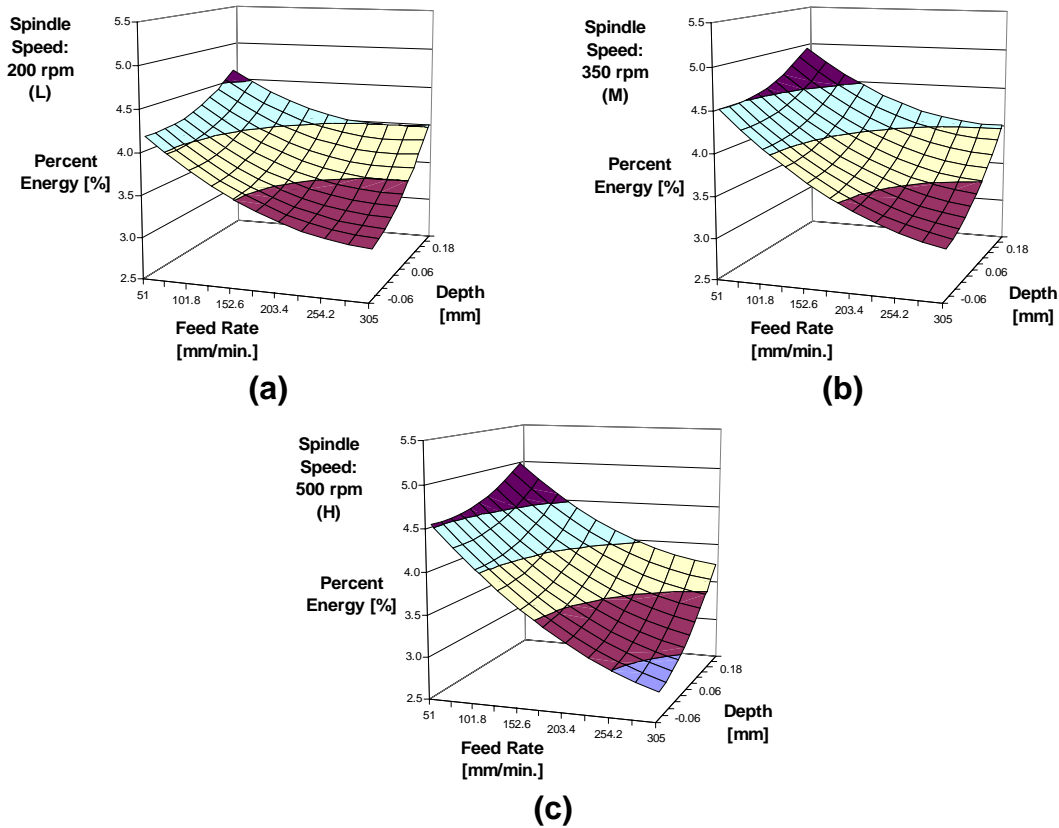
Figure 23. Percent Energy regression equation plotted versus Feed Rate and Shoulder Depth at different Spindle Speed values: (a) 200 rpm (L); (b) 350 rpm (M); (c) 500 rpm (H).

small (2.8% - 5.1%), there is clearly variation with respect to welding parameters in the

Percent Energy values.

4.1.4 Experimental Data Summary

Various weld outputs, including forces and internal tool temperatures, have been

measured for welds performed over a wide range of process operating parameters. Of

utmost importance to the current research is that the heat input to the tool and portion of

the mechanical power that enters the tool have also been quantified for each weld and

that a statistical analysis of the data reveals the dependence of these two outputs on the

operating parameters. The regression equations that describe this dependence have been made available and surface plots of the equations have been presented.

4.2 Numerical Predictions

4.2.1 Grid

The grid used for the heat conduction simulations is shown in Figure 24. It is shown in the actual orientation used for the modeling, which requires that the grid be oriented such that the axis of symmetry for the model is placed in the location of what is the common X-axis. The grid density is higher near the tool/workpiece interface of the model so that the anticipated steep thermal gradients in this region will be accurately resolved. However, since the computation time required for the heat conduction models was less than one minute, the grid density even near the top of the tool is fairly high.
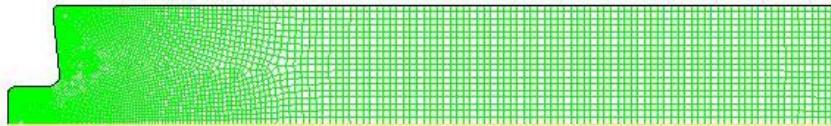
Figure 24. Axisymmetric grid used for numerical computations.

4.2.2 Radially Varying Heat Input

As described previously, three different heat flux spatial distributions were numerically modeled to investigate the true manner of tool heating, namely a radially varying heat input, a uniform heat input, and a distributed heat input. A summary table showing the parameter levels and values related to the heat input applied to the tool model for each of

65

Table 5. Four parameter combinations tested using the radially varying heat input.

Case	Spindle Speed	Feed Rate	Shoulder Depth	η	Numerical Heat Input [W]	Experimental Heat Input [W]
1	L	L	H	0.088	169.3	169.2
2	L	H	H	0.059	175.4	175.2
3	H	L	H	0.048	189.2	188.2
4	H	H	H	0.026	192.5	190.1

the cases modeled using the radially varying heat input is presented as Table 5. The

values for η, or the portion of the total radially varying heat input incident on the tool

(which was calculated from the radially varying heat input equation, Equation (13)), are

presented along with the numerical heat input value and experimental heat input as

calculated from the Tool Heat Input regression equation for each case. It should be

remembered that the value for η was iteratively adjusted until the numerical heat input

sufficiently represented that calculated by the regression equation at the given parameter

combination.

It can be seen in the table that the values for η vary significantly depending on the

parameter combination, ranging from 0.026 to 0.088, showing that 2.6% to 8.8% of the

total power generated as calculated by the Radially varying heat input equation enters the

tool over the range of parameters modeled. The numerical heat input values closely

resemble those calculated from the regression equations at the given parameter levels,

further demonstrating that reasonably accurate η values were used.

An example of a full temperature contour plot for the Radially Varying Case 4

(HHH parameter combination) is shown in Figure 25. The maximum predicted

temperature occurs near the edge of the shoulder where the maximum heat input was

applied. Although the maximum temperature varied with each case, the location of the

maximum temperature as shown is characteristic of each case when the Radially varying
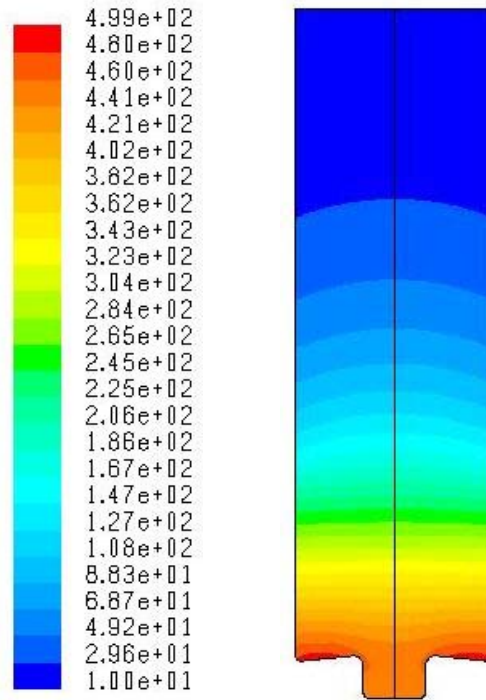
Figure 25. Predicted tool temperature contours [°C] for a weld performed at the HHH parameter combination simulated using the radially varying heat input.

heat input was applied. The pin is nearly isothermal at a temperature lower than the maximum predicted on the shoulder. The isotherms are nearly perpendicular to the tool axis at locations a few millimeters above the shoulder, showing that the axial temperature gradient of the tool does not vary with radial position and validating the assumption made for the experimental Tool Heat Input calculations.

Comparison with Experimental Data

The accuracy of a numerical model can perhaps best be measured by how closely the model predicts the measurement of actual experiments performed. Thus, as described in Section 3.1.2, predicted temperatures at the three thermocouple locations were noted and compared with the experimental data for the two welds performed at the same process

67

operating parameter combination. Predicted and experimental temperatures were

compared by calculating the following prediction error values for each case:

$$\left| T_{pred} - T_{\exp} \right| \tag{18}$$

$$T_{pred} - T_{\exp} \tag{19}$$

where T_{pred} is the predicted temperature and T_{exp} is the two-weld average experimental

temperature at a given parameter combination and thermocouple location. The absolute

prediction error derived from Equation (18) was used to quantify how close the predicted

temperature was to that measured (magnitude), and the actual prediction error in

Equation (19) revealed whether the temperature was over- or under-predicted by either a

positive or negative sign, respectively.

A summary table showing the prediction errors for the four cases where the

radially varying heat input was applied is shown as Table 6. As noted from the absolute

prediction errors, at the LLH parameter combination the predicted temperatures at the Pin

Center, Root, and Shoulder locations are within 47°C, 33°C, and 7°C, respectively, of the

measured temperatures and that the temperature at each location is generally under-

predicted by this magnitude (indicated by the negative T_{pred}-T_{exp} value). It might well be

assumed that if both the heat input magnitude and distribution were reasonably correct

that the prediction error at each of the thermocouple locations would be small. If the

distribution was correct with an incorrect heat input magnitude, the error would be scaled

equally at each of the thermocouple locations. However, at this parameter combination,

Table 6. Calculated prediction errors for the radially varying heat input.

	1 (LLH)	2 (LHH)	3 (HLH)	4 (HHH)
Pin Center				
$\left|T_{pred} - T_{exp}\right|$	47	6	53	42
$T_{pred} - T_{exp}$	-47	-6	-53	-42
Root				
$\left|T_{pred} - T_{exp}\right|$	33	4	27	24
$T_{pred} - T_{exp}$	-33	-4	-27	-24
Shoulder				
$\left|T_{pred} - T_{exp}\right|$	7	25	1	1
$T_{pred} - T_{exp}$	-7	25	1	1

it is seen that the prediction errors, especially at the Pin Center and Root locations, are quite large and that the absolute prediction error at each of the thermocouple locations differ. At the HLH and HHH parameter combinations the prediction error at the Shoulder location is near zero, but the error at the other two locations reflect that the heat input near the tool axis must be increased for a closer correlation with the experimental data.

A graphical representation of the prediction error data is shown in Figure 26. The prediction error, T_{pred}-T_{exp}, for the four cases modeled using the radially varying heat input is plotted according to the process parameter combination. Thus, it can be seen that at the LHH parameter combination, temperatures at the Pin Center and Root locations are predicted reasonably well and that at the LLH, HLH, and HHH parameter combinations the Shoulder temperature is most accurately predicted. However, at any given parameter combination, the absolute prediction error at the thermocouple locations are not equal.
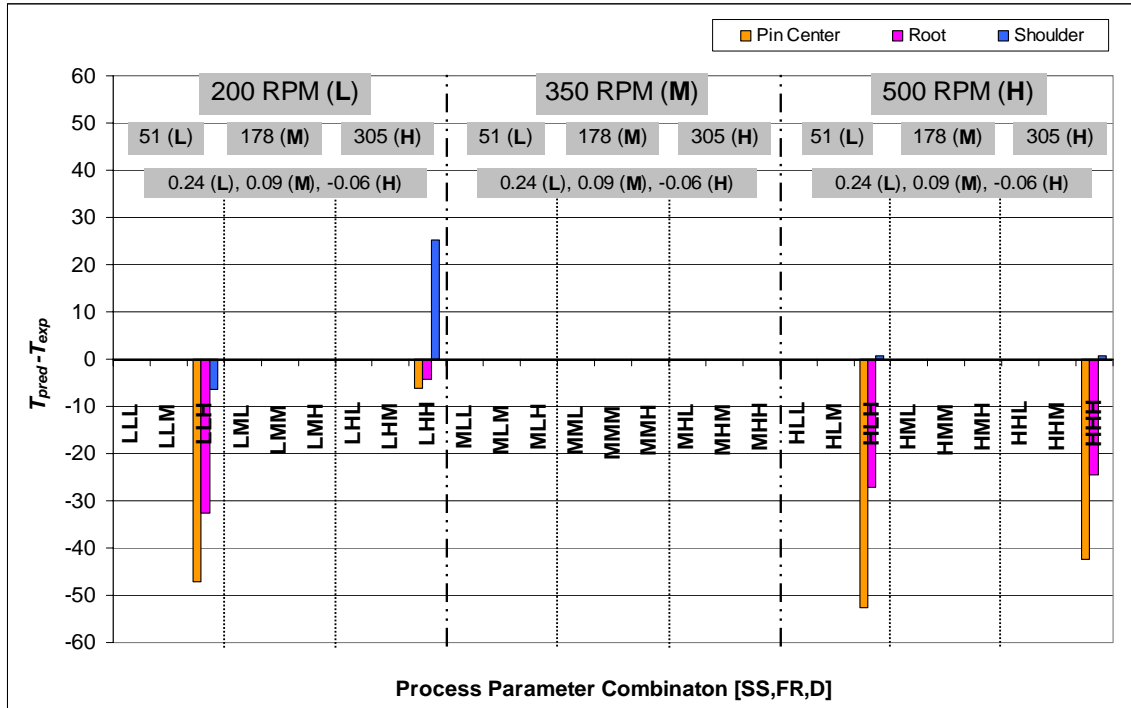
Figure 26. Prediction error for all cases modeled using the radially varying heat input configuration, plotted with respect to weld parameter combination.

How well a heat input configuration predicts that which occurs in FSW over the entire range of operating parameters modeled can be determined by calculating the mean prediction error at each of the thermocouple locations:

$$\overline{\left| T_{pred} - T_{\exp} \right|} \tag{20}$$

$$\overline{T_{pred} - T_{\exp}} . \tag{21}$$

Thus, the mean absolute prediction error calculated from Equation (20) showed how closely the experimental temperature was predicted over all of the parameter

70

combinations modeled and the mean prediction error from Equation (21) revealed to which side, either over- or under-predicted, the simulations were biased.

These mean prediction errors for each thermocouple location are listed in Table 7 for the predictions made using the radially varying heat input. An analysis of both error values for each location is necessary to understand to what degree the radially varying heat input reflects the actual heat input distribution present in FSW. It can be seen from the absolute prediction error at the Pin Center location that, on average, the predicted temperature was within 37°C of the experimental temperature. The mean prediction error shows that the predictions were biased toward an under-prediction of the experimental value (noted by the minus sign). Since the mean error was -37°C, the magnitude of which is equal to the absolute error, the temperature was under-predicted for all cases. An analysis of the mean prediction error for the Root thermocouple location gives similar results. However, at the Shoulder location, the predictions were within 8°C of the experimental values, but over-predicted by an average of 5°C, showing that, although some under-predictions were made, there was a bias toward an over-prediction of the experimental value. These trends can be confirmed by further analysis of the plot in Figure 26.

From the mean prediction error it may be said that the radially varying heat input does not accurately reflect the distribution present in FSW. Although a relatively accurate representation of the heat input magnitude is made near the Shoulder thermocouple location, the magnitude of the heat input near the tool axis is clearly too low for accurate prediction of the temperatures at the Pin Center and Root locations. The trend of obtaining artificially high Shoulder temperatures has been noted by Colegrove

**Table 7. Mean prediction error values
for the radially varying heat input.**

	Radially Varying Heat Input
Pin Center	
$\left|\overline{T_{pred} - T_{exp}}\right|$	37
$\overline{T_{pred} - T_{exp}}$	-37
Root	
$\left|\overline{T_{pred} - T_{exp}}\right|$	22
$\overline{T_{pred} - T_{exp}}$	-22
Shoulder	
$\left|\overline{T_{pred} - T_{exp}}\right|$	8
$\overline{T_{pred} - T_{exp}}$	5

and Shercliff as a result of using a heat flux that varies proportionally with radius
[Colegrove, 2003]. For this reason they chose to apply a uniform heat flux over the
shoulder and pin surfaces of the tool in their model.

4.2.3   Uniform Heat Input

Tool heating of welds performed at each of the 27 parameter combinations was modeled
by applying a heat input that was uniformly distributed over the tool/workpiece interface.
A representative temperature contour plot for the simulation of a weld performed at the
LLL parameter combination is shown in Figure 27. The maximum temperature of
599°C, which is above the solidus temperature of the workpiece material (532°C,
[Colegrove, 2003]), occurs near the bottom of the pin. A temperature gradient is clearly
apparent within the pin itself, and the temperature gradient continues upward through the
remainder of the tool. Although it may be said that the utility of applying a uniform heat
input has already been proven as unsatisfactory by predicting temperatures well above the
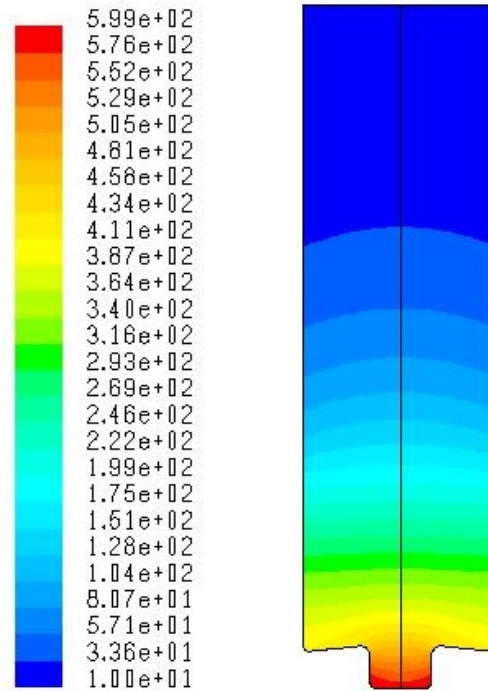
Figure 27. Predicted tool temperature contours [°C] for a weld performed at the LLL parameter combination when the Uniform Heat Input was applied.

workpiece solidus temperature, the results of the model for comparative purposes are quite useful.

Comparison with Experimental Data

As a summary table of prediction error values would be much too extensive for all 27 parameter combinations, the values are shown graphically in Figure 28. The prediction errors are plotted with respect to process operating parameter combination. From the data presented it is apparent that the Pin Center temperature is significantly over-predicted at all of the 27 parameter combinations, with errors ranging from 119°C to 173°C. Temperatures at the Root location are over-predicted at all but one of the 27 combinations, ranging from -1°C to 43°C. Temperatures at the Shoulder location are perhaps most closely predicted, ranging from -24°C to 10°C, the majority of which

73
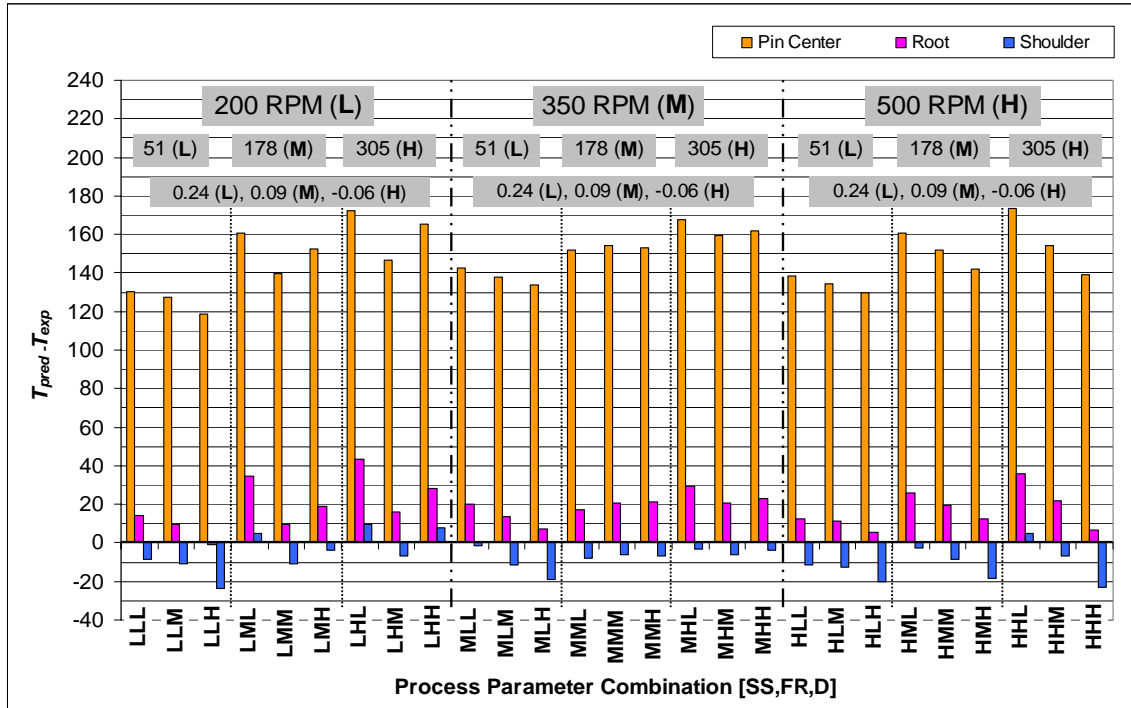
Figure 28. Prediction error plotted according to process parameter combination for the Uniform Heat Input simulations.

are under-predictions. Thus, it might be said that, although the radially varying heat input may result in artificially high Shoulder temperatures, the Uniform Heat Input clearly applies an excess amount of heat to portions of the interface near the tool axis.

The mean absolute prediction error and mean prediction error values for simulations utilizing the Uniform Heat Input are summarized for each thermocouple location in Table 8. Values for the radially varying heat input are also displayed for comparative purposes. When the Uniform Heat Input is utilized the Pin Center temperature is consistently over-predicted, with an mean absolute error of 148°C. The Root temperature is within 19°C of the experimental value, with an extreme bias toward an over-prediction and the Shoulder temperature is, on average, within 10°C of the measured value and with a bias toward an under prediction. Thus, from the mean

**Table 8. Mean prediction error values for the radially
varying and Uniform Heat Input configurations.**

	Radially Varying Heat Input	Uniform Heat Input
Pin Center		
$\overline{\left\|T_{pred} - T_{exp}\right\|}$	37	148
$\overline{T_{pred} - T_{exp}}$	-37	148
Root		
$\overline{\left\|T_{pred} - T_{exp}\right\|}$	22	19
$\overline{T_{pred} - T_{exp}}$	-22	18
Shoulder		
$\overline{\left\|T_{pred} - T_{exp}\right\|}$	8	10
$\overline{T_{pred} - T_{exp}}$	5	-8

prediction error it is apparent that when welds performed at all process parameter combinations are modeled using the Uniform Heat Input there is an overabundance of heat applied near the tool axis and insufficient heating present near the shoulder periphery.

From a comparison of the mean errors between the radially varying and Uniform Heat Input configurations it is difficult to state which may be more reflective of the FSW process. Although an under-prediction of both the Pin Center and Root thermocouple temperatures was achieved using the Radially varying heat input, the significant over-prediction of these values when using a Uniform Heat Input hardly justifies its use, especially when the over-prediction of the Pin Center temperature is of such a great magnitude. It is also again noteworthy that the maximum temperatures predicted when applying the Uniform Heat Input were above the solidus temperature of the workpiece material, which is unrealistic when modeling a solid-state joining process such as FSW.

4.2.4   Distributed Heat Input

Tool heating of welds performed at each of the 27 operating parameter combinations was modeled by applying a heat input that was non-uniformly distributed along the tool/workpiece interface. Using an iterative approach at the LLL parameter combination, the values for η_i, or the fraction of the total Tool Heat Input imposed on a given zone (see Equation (15)), which varied from zone to zone, were adjusted until the prediction error at each thermocouple location was minimized. The η_i values then remained the same for the models of the welds performed at the remaining 26 parameter combinations. The optimal η_i values for each zone along the tool/workpiece interface (see Figure 29) obtained from the iterations are summarized in Table 9. It is apparent from the values presented that a total of 1% of the Tool Heat Input enters the pin, 20% enters the tool near the Root thermocouple location, and the remaining 79% enters through the shoulder.
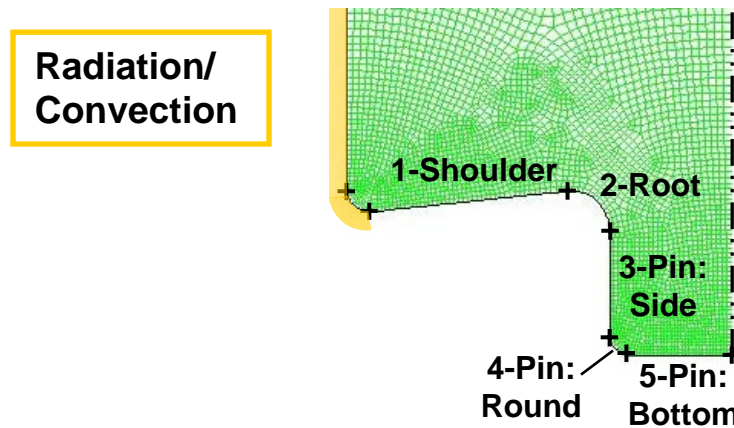
Figure 29. Tool/workpiece interface detail of numerical model showing zone designations.

Table 9. Fraction of Tool Heat Input incident on each zone.

Zone	η_i
1-Shoulder	0.79
2-Root	0.2
3-Pin: Side	0.004
4-Pin: Round	0.003
5-Pin: Bottom	0.003

A temperature contour plot of a simulation of a weld performed at the LLL parameter combination is shown in Figure 30. Similar to the simulations performed using the radially varying heat input, the pin of the tool is nearly isothermal, but the maximum temperature for the simulation (448°C) now occurs near the pin. Temperatures in the tool decrease upward along the tool axis from the shoulder.
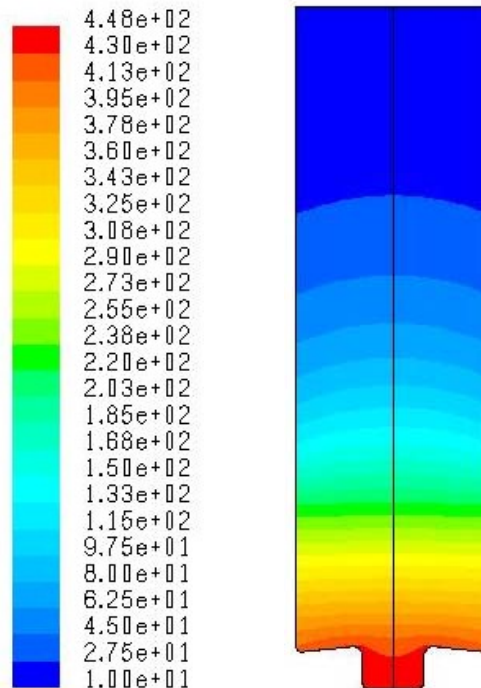
Figure 30. Predicted tool temperatures contours [°C] for a weld performed at the LLL parameter combination when the Distributed Heat Input was utilized.
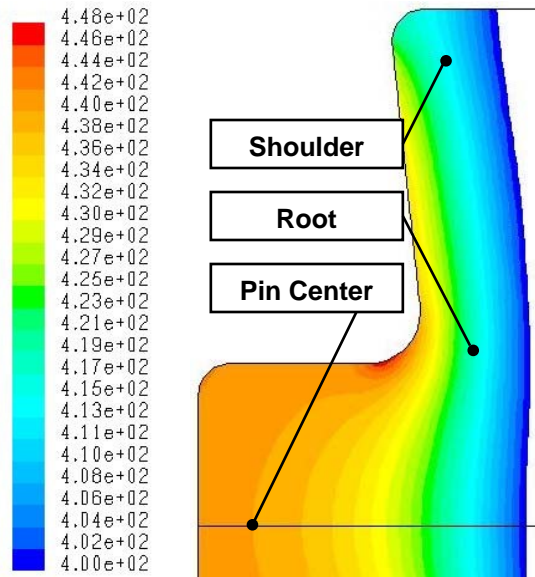
**Figure 31. Scaled temperature contour detail (range: 400-448°C) of the
simulation of a weld performed at the LLL parameter combination.**

An additional detail of contours near the tool/workpiece interface is shown in

Figure 31. The temperature scale has been adjusted so that gradients along the interface

and in the pin are visible (range: 400 - 448°C). The thermocouple measurement locations

are also noted. It is seen here that the maximum temperature in the simulations actually

occurs at the base of the pin, with steep temperature gradients occurring along the

shoulder. Gradients in the pin are much less apparent, further showing that the pin is

nearly isothermal. In fact, the maximum predicted temperature is only 7°C greater than

the experimental Pin Center temperature at this parameter combination. Thus, the

measured Pin Center temperature may reflect the maximum tool temperature at most

parameter combinations. It is interesting that the maximum temperature for the

simulation occurs at the base of the pin, as numerical studies by Askari et al. [2001] have

indicated that maximum flow stress and temperatures in the workpiece occur in a region

near the base of the pin.
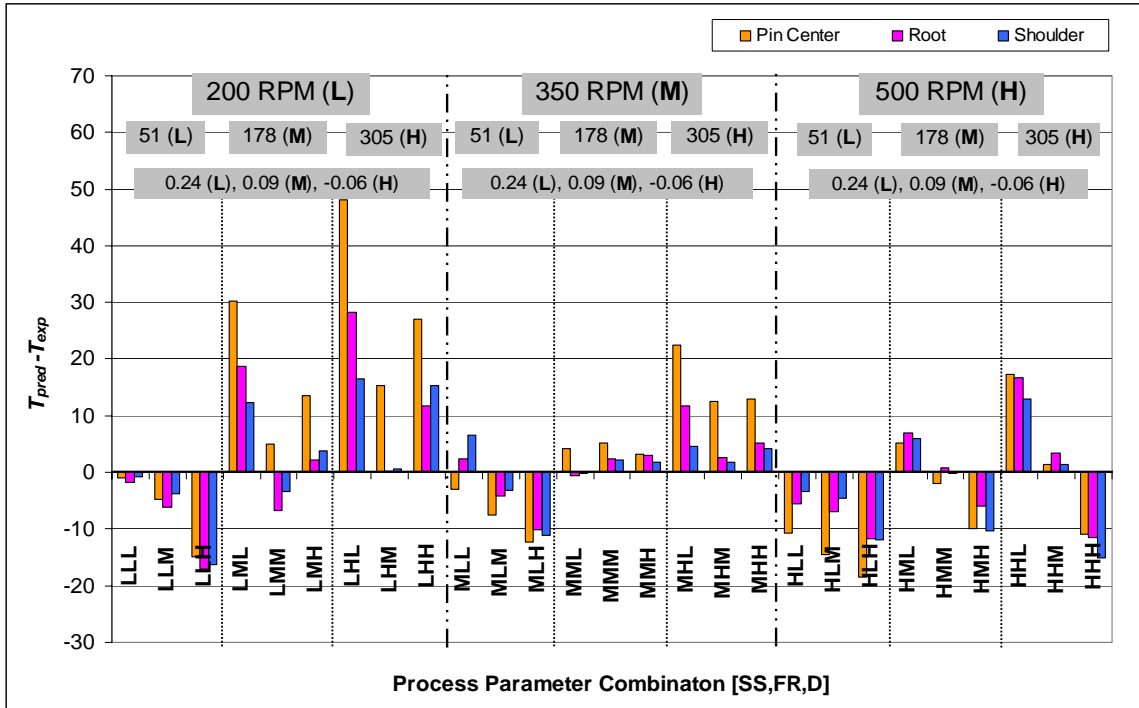
Figure 32. Prediction error plotted according to process operating parameter combination for the Distributed Heat Input configuration.

Comparison with Experimental Data

The prediction errors for the 27 simulations performed using the Distributed Heat Input are shown graphically in Figure 32, plotted again with respect to process operating parameters. It is seen here that the errors for each of the three thermocouple locations are now randomly distributed about the zero difference line. Predictions at the Pin Center location are within the -18°C to 48°C range. Predictions at the Root and Shoulder locations are within the ranges of -17°C to 28°C and -16°C to 16°C, respectively. At 14 of the 27 parameter combinations the difference values at all three thermocouple locations are within 5°C of each other (see for example: LLL, LLM, LLH, etc.), and at 24 of the 27 parameter combinations the difference values of the Root and Shoulder temperatures are within 5°C of the other (see for example: LLL, LLM, LHM, etc.). At 7

79

of the 27 parameter combinations the Pin Center temperature difference is 10°C or greater than the difference at either the Root or Shoulder location (see for example: LHL, LHH, etc.).

In Table 10 the mean prediction error values for all three heat input configurations are shown. As noted in the table, when the Distributed Heat Input is used to model tool heating at the 27 different parameter combinations, temperature predictions at the Pin Center location that are within 12°C of the experimental value, with a slight bias toward an over-prediction. Predicted temperatures at the Root location are within 8°C of the experimental values, with a very slight bias toward over-prediction, and the predicted Shoulder temperatures are within 6°C of the experimental value with a virtually even distribution about the zero difference line.

The mean error values for the Distributed Heat Input are clearly much less than those for either the radially varying or Uniform Heat Input configurations. The mean absolute error for each of the three thermocouple locations

Table 10. Mean prediction error values for all heat input configurations.

	Radially Varying Heat Input	Uniform Heat Input	Distributed Heat Input
Pin Center			
$\overline{\left\|T_{pred} - T_{exp}\right\|}$	37	148	12
$\overline{T_{pred} - T_{exp}}$	-37	148	4
Root			
$\overline{\left\|T_{pred} - T_{exp}\right\|}$	22	19	8
$\overline{T_{pred} - T_{exp}}$	-22	18	1
Shoulder			
$\overline{\left\|T_{pred} - T_{exp}\right\|}$	8	10	6
$\overline{T_{pred} - T_{exp}}$	5	-8	0.2

are quite remarkable and the distribution of the difference values about the zero-error line are especially close at the Root and Shoulder thermocouple locations. Thus, whereas the heat input magnitude was discovered from weld experiments, an approximate heat input spatial distribution along the tool/workpiece interface has been identified using numerical tool models. The proposed distribution closely reflects the actual distribution present during steady-state FSW.

Variation of Heat Input Distribution with Operating Parameters

It has already been demonstrated that the total heat generation and Tool Heat Input are extremely dependent on operating parameters. Similarly, variations in the softened weld material will also occur which change the interaction between the tool and workpiece. As Spindle Speed increases, heat generation in the weld zone similarly increases, softening the workpiece material to a greater degree. Increasing Feed Rate causes the tool to be forced into colder workpiece material at a greater rate. Changes in tool depth with respect to the top surface of the workpiece will greatly affect the tool/workpiece interaction as more or less of the shoulder area contacts the workpiece. It is therefore safe to assume that a variation in the Tool Heat Input distribution will also occur with process operating parameters.

This phenomenon is perhaps best seen at the LHL parameter combination. The contact condition between the tool and workpiece is unique at this combination where the heat generation from the rotation of the tool is lowest (SS = L), the pin is forced into the colder workpiece material at the highest rate (FR = H), and tool shoulder/workpiece contact is the least, with only the rear portion of the shoulder in contact with the workpiece (D = L). Thus, any preheating of the workpiece in front of the pin is

overcome by the high Feed Rate value. It was noted in Section 4.1.1 that at this

parameter combination, and only at this combination, the experimental Pin Center

temperature was lower than the Shoulder temperature. It was also at this parameter

combination that the X-force to Z-force ratio was the highest and the greatest Y-force

was detected. In Figure 32 it was also at this parameter combination that all three

thermocouple temperatures were over-predicted by their respective maximum values, the

most notable being the Pin Center temperature which was over-predicted by 48°C.

An adjustment in the heat input distribution to lower the heat input at locations

near the tool axis may allow for more accurate predictions at all three temperature

measurement locations at this parameter combination. For example, when the radially

varying heat input is applied at the LHL parameter combination, the Pin Center, Root,

and Shoulder temperatures are over-predicted by values of 17°C, 12°C, and 24°C,

respectively. When compared with the over-predictions seen in Figure 32 of 48°C, 28°C,

and 16°C, respectively, it may be said that a more accurate representation of the actual

distribution at the LHL parameter combination might be the radially varying heat input.

Since the over-prediction at the Shoulder location was high when using the radially

varying heat input, an even more accurate approximation may be some intermediate

distribution.

A similar adjustment to the heat input distribution could also be made at the LMx,

LHx, and MHx parameter combinations (where x represents any of the three factor levels

of Shoulder Depth) where the preheating of the tool is lower, due to lower heat inputs

from the rotation of the tool, and is easily overcome by the higher Feed Rate values. At

each of these parameter combinations the difference values for the Pin Center location is

82

significantly greater than the difference for either the Root or Shoulder thermocouple locations, showing that a lower heat input near the tool axis may be advantageous.

At the HL*x* parameter combinations, the Pin Center temperature is under-predicted with a magnitude that is noticeably less than the magnitude of either the Root or Shoulder locations. At these parameter combinations the distribution could perhaps be adjusted to allow a greater portion of the heat to enter the pin. Thus, when the heat generation from the rotating tool is greatest (SS = H) and the tool is forced into workpiece material at the slowest rate (FR = L), the Distributed Heat Input configuration does not account for additional pre-heating of the workpiece material that may actually occur.

Elimination of Heat Input to the Pin

With such a small portion of the Tool Heat Input entering the pin it is logical to question the value of applying any portion of the Tool Heat Input to the pin. Two additional cases were performed in FLUENT, one simulation each of the welds performed at the LLL and HHH parameter combinations, to investigate the importance of applying 1% of the Tool Heat Input to the pin. The heat input distribution was modified, eliminating the heat input to the pin and applying the additional 1% to Zone 2-Root, or in the area of shoulder near the Root thermocouple location (see Table 9 and Figure 29).

Predicted temperatures from these two cases are displayed in Table 11 along with predicted temperatures from cases performed using the Distributed Heat Input. It can be noted from the values presented that removing the heat input to the pin effectively lowered the predicted Pin Center temperature by approximately 5°C, while the predicted temperatures at the other two thermocouple locations remained virtually unchanged.

Table 11. Comparison of predicted tool temperatures: Distributed Heat Input and modified Distributed Heat Input with pin heat input eliminated.

	Pin Center [C]	Root [C]	Shoulder [C]
LLL			
Distributed Heat Input	440	419	416
Pin Heat Input Eliminated	436	419	415
HHH			
Distributed Heat Input	490	466	461
Pin Heat Input Eliminated	485	466	461

Although not shown here, the temperature gradients through the pin when using the modified heat input were also reduced, causing the pin to be more isothermal then when applying the Distributed Heat Input.

If the heat input to the pin were eliminated for all 27 cases modeled, it could be assumed that the predicted Pin Center temperature would be lowered by approximately 5°C. This would lower the prediction error at the Pin Center by that same amount for all 27 cases (see Figure 32). If this were to happen, the difference value of the Pin Center thermocouple location would be lower than the difference value for the other two thermocouple locations for 17 of the 27 cases (LLx, MLx, MMM, MMH, and Hxx), lessening the accuracy of the predictions and showing the need for the additional 1% to be applied to the pin. Nine of the remaining ten parameter combinations (LMx, LHx, and MHx) have already been noted above as combinations where a lower heat input near the tool axis would allow for a closer correlation of the predicted and experimental temperatures. However, 5°C would hardly improve the predictions at the LHx combinations. For the final case (MML) the difference values for the Pin Center and Root thermocouple locations would be equal, showing the best improvement for the 27 parameter combinations and affirming that, at the majority of the parameter

combinations, applying 1% of the total heat input to the pin is a true reflection of the distribution that occurs during FSW.

4.3   Implications of the Distributed Heat Input

Numerical results from simulations performed utilizing the Distributed Heat Input reveal much about temperature profiles that exist in the tool and give other insights into the FSW process. It has already been noted that the pin is nearly isothermal and that the maximum temperature in the tool is located at the base of the pin at a majority of process operating parameter combinations (see Figure 30). For many years it has been thought that a maximum temperature exists near the shoulder periphery where, when assuming a radially varying heat input, both a maximum heat input and temperature do exist. However, it is has been shown by both the experimental data and numerical predictions that, for a majority of operating parameters, the pin is the warmest portion of the tool. Even at the one experimental parameter combination where the measured Shoulder temperature was greater than that measured at the Pin Center and Root locations (LHL), the difference is small (7°C), meaning that the temperature along the interface is nearly isothermal at this operating parameter extreme. It is further interesting that the pin is warmest even though the heat input applied to the pin is a very small percentage (1%) of the heat that enters the tool.

By noting that only a small percentage of the Tool Heat Input enters the pin, some interesting conclusions can be drawn about the temperature of the weld material in the vicinity of the pin. Heat Transfer is defined as the transfer of energy as a result of a temperature difference. If there is little heat transfer between to bodies or regions within a single body it can be assumed that either: 1) a high thermal resistance exists between
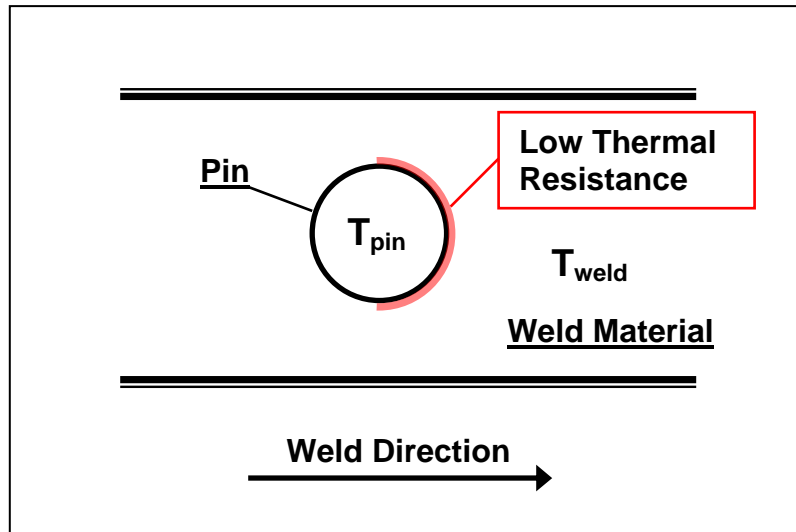
Figure 33. Simplified diagram of the pin traveling through the softened weld material during FSW.

the two bodies or regions, or 2) the two bodies or regions are at nearly equal

temperatures.

A diagram of the pin traveling through the softened weld material is shown in

Figure 33 with the temperatures of the pin and weld material denoted as T_{pin} and T_{weld}.

As the pin is forced through the weld material it may well be assumed that excellent

contact between the pin and weld material is created from the high forces against the pin,

resulting in a very low thermal resistance. Thus, it can also be assumed that the

temperature of the weld material near the pin is very near the temperature measured at the

Pin Center.

This would indicate that the maximum temperature in the workpiece during

steady-state FSW occurs near the pin. Experimental results published by other

researchers support this fact, where maximum temperatures in the workpiece have been

reported at locations at or near the joint line or at locations near the edge of the pin

[Khandkar,2003; Shi,2003;, Song, 2003a; Chao,1998; Askari, 2001; McClure, 1998;

Tang, 1998]. Much of the experimental data shown also indicates a nearly isothermal region near the joint line at or near this maximum temperature [Khandkar, 2003; Chao, 1998; McClure, 1998; Tang, 1998]. The temperatures then decrease out into the workpiece.

Assuming that the measured Pin Center temperature is the maximum temperature in the workpiece, the maximum temperature of the material in the weld zone ranged from 371°C to 507°C over the entire operational parameter window tested. The minimum value in this range is far below the workpiece solidus temperature and it is interesting that welds can be performed at such low temperatures. Although a maximum X-force was not recorded at the same parameter combination used to produce a weld with this minimum temperature (LHL), the X-force to Z-force ratio was greatest here, perhaps indicating that very high strains must be present in the weld zone to enable the pin to move through the workpiece material.

Unfortunately there is very little that can be learned about the distribution of heat generation during FSW from the current study. The Total Heat Input, or the mechanical power required for each weld, has been measured for the 54 welds and the values have been presented, but there is little that can be concluded about the respective contributions of the pin or shoulder to the heat generation process or locations of maximum or minimum heat generation within the workpiece.

5 Conclusions

The heat input quantity and distribution to the tool has been investigated for friction stir welding of aluminum alloy AL 7075-T7351 over a wide range of process operating parameters. 54 experimental welds were performed in a statistical Design of Experiments fashion at 27 different parameter combinations and Tool Heat Input values were extracted for each weld and subsequently analyzed to identify the effect of process operating parameters. The percentage of the mechanical power that entered the tool (Percent Energy) was also quantified and analyzed. Numerical heat conduction models of the tool were then produced and the spatial distribution of the Tool Heat Input along the tool/workpiece interface was analyzed. The following conclusions can be drawn for the tool and workpiece combination used:

- The experimental Tool Heat Input ranged from 155 W to 200 W for the tool/workpiece combination used over the entire range of process operating parameters tested

- The percentage of the mechanical power that entered the tool ranged between 2.8% and 5.1%

- The Tool Heat Input and Percent Energy values are functions of the process operating parameters

- At a majority of process operating parameter combinations a Distributed Heat Input configuration exists where 79% of the Tool Heat Input enters the tool through the shoulder, 20% enters the tool at the base of the pin near the Root thermocouple location, and 1% enters the pin

- A radially varying heat input configuration, where a maximum heat generation is assumed to exist on the shoulder periphery, does not reflect that present in FSW

- Maximum temperatures in the tool are predicted to occur near the base of the pin when the Distributed Heat Input configuration is assumed to exist

- The distribution of the tool heat input along the tool/workpiece interface is also a function of process operating parameters and at some parameter combinations does not reflect that modeled by the Distributed Heat Input

- The temperature of the softened material in the weld zone during steady-state FSW is near that measured at the Pin Center thermocouple location in the tool, ranging from 371°C to 507°C for the operational parameter test window used

REFERENCES

Askari, A., S. Silling, B. London, and M. Mahoney, 2001, "Modeling and Analysis of Friction Stir Welding Processes", *Friction Stir Welding and Processing*, TMS (The Minerals, Metals & Materials Society), pp. 43-54.

Chao, Y. J. and X. Qi, 1998, "Thermal and Thermo-Mechanical Modeling of Friction Stir Welding of Aluminum Alloy 6061-T6", *Journal of Materials Processing and Manufacturing Science*, October 1998, Technomic Publishing Co., Inc., pp. 215-233.

Chao, Y. J., X. Qi, and W. Tang, 2003, "Heat Transfer in Friction Stir Welding— Experimental and Numerical Studies", *Journal of Manufacturing Science and Engineering, Transactions of the ASME*, vol. 25, no. 1, February 2003, ASME, pp. 138-145.

Chen, C., and R. Kovacevic, 2003, "Finite Element Modeling of Friction Stir Welding— Thermal and Thermomechanical Analysis", *International Journal of Machine Tools & Manufacture*, vol. 43, Elsevier Ltd., pp. 1319-1326.

Colegrove, Paul, 2000, "3 Dimensional Flow and Thermal Modeling of the Friction Stir Welding Process", *Proceedings of the 2nd International Symposium on Friction Stir Welding*, 26-28 June 2000, Gothenburg, Sweden.

Colegrove, P. A., and H. R. Shercliff, 2003, "Experimental and Numerical Analysis of Aluminium Alloy 7075-T7351 Friction Stir Welds", *Science and Technology of Welding and Joining*, vol. 8, no. 5, IoM Communications Ltd., pp. 360-368.

Desrayaud, Ch., P. Heurtier, D. Allehaux, and F. Montheillet, 2004, "Thermomechanical and Microstructural Modelling of the Friction Stir Welding Process", *Proceedings of the 5th International Symposium on Friction Stir Welding*, 14-16 Sept. 2004, Metz, France.

Dickerson, T., Q. Shi, and H. R. Shercliff, 2003, "Heat Flow into Friction Stir Welding Tools", *Proceedings of the 4th International Symposium on Friction Stir Welding, Poster Presentation*, 14-16 May 2003, Park City, Utah, USA.

Dong, P., F. Lu, K. Hong, and Z. Cao, 2001, "Coupled Thermomechanical Analysis of Friction Stir Welding Process using Simplified Models", *Science and Technology of Welding and Joining*, vol. 6, no. 5, pp. 281-287.

Figliola, R. S., and D. E. Beasley, 2000, *Theory and Design for Mechanical Measurements, Third Edition*, New York, NY: John Wiley and Sons, Inc., pp. 151-161.

Frigaard, O., O. Grong, and O. T. Midling, 2001, "A Process Model for Friction Stir Welding of Age Hardening Aluminum Alloys", *Metallurgical and Materials Transactions A, Physical Metallurgy and Materiasl Science*, vol. 32A, no. 5, May 2001, ASM International, pp. 1189-2000.

Goetz, R. L., and K. V. Jata, 2001, "Modelling Friction Stir Welding of Titanium and Aluminum Alloys", *Friction Stir Welding and Processing*, TMS (The Minerals, Metals & Materials Society), pp. 35-42.

Gould, J. E. and Z. Feng, 1998, "Heat Flow Model for Friction Stir Welding of Aluminum Alloys", *Journal of Materials Processing and Manufacturing Science*, vol. 7, October 1998, Technomic Publishing Co., Inc., pp. 185-194.

Heurtier, P., C. Desrayaud, and F. Montheillet, 2002, "A Thermomechanical Analysis of the Friction Stir Welding Process", *Materials Science Forum*, vols. 396-402, no. 3, Trans Tech Publications, Switzerland, pp. 1537-1542.

Heurtier, P., M. J. Jones, C. Desrayaud, J. H. Driver, and F. Montheillet, 2003, "Thermomechanical Conditions and Resultant Microstructures in Friction Stir Welded 2024 Aluminum", *Materials Science Forum*, vols. 426-432, no. 4, Trans Tech Publications, Switzerland, pp. 2927-2932.

Hyoe, T., P. A. Colegrove, and H. R. Shercliff, 2003, "Thermal and Microstructure Modelling in Thick Plate Aluminium Alloy 7075 Friction Stir Welds", *Friction Stir Welding and Processing II*, TMS (The Minerals, Metals & Materials Society), pp. 33-42.

Incropera, F. P, and D. P. Dewitt, 2002, *Fundamentals of Heat and Mass Transfer, Fifth Edition*, New York, NY: John Wiley and Sons, Inc.

Kendoush, A. A., 1996, "An Approximate Solution of the Convective Heat Transfer from an Isothermal Rotating Cylinder", *International Journal of Heat and Fluid Flow*, vol. 17, Elsevier Science Inc., pp. 439-441.

Khandkar, M. Z. H., and J. A. Khan, 2001, "Thermal Modeling of Overlap Friction Stir Welding for Al-Alloys", *Journal of Materials Processing & Manufacturing Science*, vol. 10, October 2001, Sage Publications, pp. 91-105.

Khandkar, M. Z. H., J. A. Khan, and A. P. Reynolds, 2003, "Prediction of Temperature Distribution and Thermal History during Friction Stir Welding: Input Torque Based Method", *Science and Technology of Welding and Joining*, vol. 8, no. 3, pp. 165-174.

Langerman, Michael, and Devin Kvalvik, 2003, "Modeling Plasticized Aluminum Flow and Temperature Fields during Friction Stir Welding", *Proceedings of The 6th ASME-JSME Thermal Engineering Joint Conference*, 16-20 March 2003, JSME, No. TED-AJ03-133.

Lawson, J., and J. Erjavec, 2001, *Modern Statistics for Engineering and Quality Improvement*, Pacific Grove, CA: Duxbury/Wadsworth Group.

Lienert, T. J., and W. L. Stellwag, 2001, "Determination of Load, Torque, and Tool Temperature During Friction Stir Welding", *Abstracts of Papers Presented at the 2001 AWS Convention, Cleveland, Ohio*, 82nd American Welding Society Annual Meeting, 6-10 May 2001, AWS, pp. 152-155.

Lienert, T. J., W. L. Stellwag, Jr., B. B. Grimmett, and R. W. Warke, 2003a, "Friction Stir Welding Studies on Mild Steel", *Welding Journal*, vol. 82, no. 1, January 2003, American Welding Society, pp. 1S-9S.

Lienert, T. J., W. L. Stellwag, Jr., and L. R. Lehman, 2003b, "Heat Inputs, Peak Temperatures and Process Efficiencies for FSW", *Proceedings of the 4th International Symposium on Friction Stir Welding*, 14-16 May 2003, Park City, Utah, USA.

Mahoney, M. W., C. G. Rhodes, J. G. Flintoff, R. A. Spurling, and W. H. Bingel, 1998, "Properties of Friction-Stir-Welded 7075 T651 Aluminum", *Metallurgical and Materials Transactions A: Physical Metallurgy and Materials Science*, vol. 29A, no. 7, July 1998, TMS, pp. 1955-1964.

McClure, J. C., W. Tang, L. E. Murr, X. Guo, Z. Feng and J. E. Gould, 1998, "A Thermal Model of Friction Stir Welding", *Trends in Welding Research*, June 1998, ASM International, pp. 590-595.

Montgomery, D. C., G. C. Runger, and N. F. Hubele, 2001, *Engineering Statistics, Second Edition*, New York, NY: John Wiley and Sons, Inc.

Nishihara, T., and Y. Nagasaka, 2003, "Measurement of Tool Temperature During Friction Stir Welding", *Proceedings of the 4th International Symposium on Friction Stir Welding* 14-16 May 2003, Park City, Utah, USA.

North, T. H., G. J. Dendzsak, and C. Smith, 2000, "Material Properties Relevant to 3-D FSW Modeling", *Proceedings of the 2nd International Symposium on Friction Stir Welding*, 26-28 June 2000, Gothenburg, Sweden.

omega.com, "Thermocouples and Thermocouple Assemblies: Introduction to Thermocouples", The Temperature Handbook, vol. 29, Omega Engineering , Inc., pp. A-7, available online: www.omega.com.

Record, J. H., J. L. Covington, T. W. Nelson, C. D. Sorensen, and B. W. Webb, 2004, "Fundamental Characterization of Friction Stir Welding", *Proceedings of the 5th International Symposium on Friction Stir Welding*, 14-16 Sept. 2004, Metz, France.

Reynolds, A. P., Z. Khankdar, T. Long, W. Tang, and J. Khan, 2003, "Utility of Relatively Simple Models for Understanding Process Parameter Effects on", *Materials Science Forum*, vols. 426-432, no. 4, Trans Tech Publications, Switzerland, pp. 2959-2964.

Russell, M. J., and H. R. Shercliff, 1998, "Analytical Modelling of Friction Stir Welding", *Papers presented at the Seventh International Conference Joints in Aluminum - INALCO98*, 15-17 April 1998, Cambridge, UK, pp. 197-207.

Russell, M. J., and H. R. Shercliff, 1999, "Analytical Modelling of Microstructure Development in Friction Stir Welding", *Proceedings of the 1st International Symposium on Friction Stir Welding*, 14-16 June 1999, Thousand Oaks, CA, USA.

Russell, M. J., H. R. Shercliff, and P. L. Threadgill, 2001, "Development and Application of and Analytical Process Model for Friction Stir Welding", *Aluminum 2001 – Proceedings of the TMS 2001, Aluminum Automotive and Joining Sessions*, TMS (The Minerals, Metals & Materials Society),   pp. 225-234.

Schmidt, H. N. B., and J. Hattel, 2004a, "Heat Source Models in Simulation of Heat Flow in Friction Stir Welding", *International Journal of Offshore and Polar Engineering*, vol. 14, no. 4, The International Society of Offshore and Polar Engineering, pp. 296-304.

Schmidt, H., and J. Hattel, 2004b, "Modelling Thermomechanical Conditions at the Tool/matrix Interface in Friction Stir Welding", *Proceedings of the 5th International Symposium on Friction Stir Welding*, 14-16 Sept. 2004, Metz, France.

Schmidt, H., J. Hattel, and J. Wert, 2004c, "An Analytical Model for the Heat Generation in Friction Stir Welding", *Modelling and Simulation in Materials Science and Engineering*, vol. 12, IOP Publishing Ltd., UK, pp. 143-157.

Seidel, T. U., and A. P. Reynolds, 2003, "Two-dimensional Friction Stir Welding Process Model Based on Fluid Mechanics", *Science and Technology of Welding and Joining*, vol. 8, no. 3, pp. 175-183.

Shi, Q., T. Dickerson, and H. R. Shercliff, 2003, "Thermo-mechanical FE Modelling of Friction Stir Welding of Al-2024 Including Tool Loads", *Proceedings of the 4th International Symposium on Friction Stir Welding*, 14-16 May 2003, Park City, Utah, USA.

Simar, A., T. Pardoen, and B. de Meester, 2004, "Influence of Friction Stir Welding Parameters on the Power Input and Temperature Distribution in Aluminium Alloys", *Proceedings of the 5th International Symposium on Friction Stir Welding*, 14-16 Sept. 2004, Metz, France.

Song, M. and R. Kovacevic, 2003a, "Numerical and Experimental Study of the Heat Transfer Process in Friction Stir Welding", *Proceedings of the Institution of Mechanical Engineers Part B: Journal of Engineering Manufacture*, vol. 217, no. 1, Professional Engineering Publishing Ltd., pp. 73-85.

Song, M. and R. Kovacevic, 2003b, "Thermal Modeling of Friction Stir Welding in a Moving Coordinate System and its Validation", *International Journal of Machine Tools and Manufacture*, vol. 43, no. 6, May 2003, Elsevier Science Ltd., pp. 605-615.

Song, M. and R. Kovacevic, 2003c, "A Coupled Heat-Transfer Model for Workpiece and Tool in Friction Stir Welding", *Proceedings of the 4th International Symposium on Friction Stir Welding, Poster Presentation*, 14-16 May 2003, Park City, Utah, USA.

Sorensen, C. D., T. W. Nelson and S. M. Packer, 2001, "Tool Material Testing for FSW or High-Temperature Alloys", *Proceedings of the 3rd International Symposium on Friction Stir Welding*, 27-28 September 2001, Kobe, Japan.

Sterling, C. J., T. W. Nelson, C. D. Sorensen, R. J. Steel, and S. M. Packer, 2003, "Friction Stir Welding of Quenched and Tempered C-Mn Steel", *TMS Annual Meeting, Proceedings of Friction Stir Welding and Processing II*, March 2-6 2003, San Diego, CA, USA, TMS, pp. 165-171.

Stewart, M. B., G. P. Adams, A. C. Nunes, Jr., and P. Romine, 1998, "A Combined Experimental and Analytical Modeling Approach to Understanding Friction Stir Welding", *Developments in Theoretical and Applied Mechanics*, vol. 19, Southeastern Conference on Theoretical and Applied Mechanics, pp. 472-484.

Tang, W., X. Guo, J. C. McClure, L. E. Murr, and A. Nunes, 1998, "Heat Input and Temperature Distribution in Friction Stir Welding", *Journal of Materials Processing and Manufacturing Science*, vol. 7, October 1998, Technomic Publishing Co., Inc., pp. 163-172.

Thomas, W. M., J. Nicholas, J. C. Needham, M. G. Murch, P. Temple-Smith, and C. J. Dawes, 1991, "Friction Stir Butt Welding", International Patent Application PCT/GB92/02203, GB Patent Application 9125978.8, 6 December 1991, U.S. Patent 5460317, U.S. Patent Office, Alexandria, VA, 1995.

Ulysse, P., 2002, "Three-Dimensional Modeling of the Friction Stir-welding Process", *International Journal of Machine Tools and Manufacture*, vol. 42, no. 14, Elsevier Science Ltd., pp. 1549-1557.

Appendix A

Statistical Background and Residual Analysis

BACKGROUND

In *Modern Statistics for Engineering and Quality Improvement* by Lawson and Erjavec [2001], residual ($R_i = Y_i - \hat{Y}_i$) analysis is discussed to validate four assumptions that are made:

1. The errors (or Residuals) are Normally distributed
2. The residuals have a constant variance
3. The residuals are random (experiment was randomized)
4. The residuals have a mean of zero (the model is adequate)

To check assumption 1 a Probability Plot of the Residuals is constructed. Lawson notes: "Remember that if the points come from a Normal Distribution, the plot will be a straight line." Plots given as examples seem to be fairly straight, but not perfect. Assumption 2 is checked by plotting the Residuals vs. the Fitted Values ($\hat{Y}_i$). Lawson gives two suggestions for corrections if the Constant Variance assumption seems to be poor: 1) Transform the data; and 2) Use a weighted least-squares analysis in which each data point is given a weight inversely proportional to its variance. Suggestion 2 is beyond the scope of the current work. Assumption 3 is checked by assuring that the experiment is randomized. Assumption 4 is verified by plotting the residuals against each independent variable (i.e., the factors) and also against the run order. Trends in these plots should be noted. Trends in the Residuals vs. Independent Variables plots may indicate that another variable was overlooked and may need to be accounted for. Trends with time indicated changes with time.

In a similar fashion, Montgomery et al. [2001] in *Engineering Statistics, Second Edition* states the following:

> Analysis of a factorial design assumes that the data are normally and independently distributed. The normality assumption is checked by constructing a normal probability plot of the residuals. The residuals should all lie in basically a straight line. Small variability could indicate only a slight violation of the normality assumption, and can possibly be overlooked. If an apparent pattern appears, this usually points to the need of a transformation of the data (i.e. look at the natural log or square root of the data). The independence assumption is checked by plotting the residuals against time or run order. There should be no trend with time. If a trend exists, there may be a time-dependent variable that needs to be considered for accurate data analysis. On a separate page, it was noted that, at times, a histogram of the residuals is constructed. However, the data sets are often too small in a traditional factorial design to merit the use or reliability of the histogram to note any violation of assumptions.

As will be shown hereafter, histogram plots of the residuals was not used, following the assumption given by Montgomery et al.

ANALYSIS

As stated in Section 2.5.2, multiple regression cases, each including different combinations of terms, were performed. Residual plots for the outputs were constructed for each regression equation case and analyzed. The Minitab output for the chosen Tool Heat Input regression equation is displayed below, followed by the residual plots. The Minitab output and residual plots for the chosen Percent Energy regression equation are then displayed.

TOOL HEAT INPUT

Regression Analysis

```
The regression equation is
ToolHeatInput = 124 + 0.260 SpindleSpeed + 0.0903 FeedRate - 0.370 FR*D
          +0.000905 SS*FR*D -0.000219 FR*FR -0.000277 SS*SS

Predictor          Coef        StDev            T          P
Constant        123.620        7.217        17.13      0.000
SpindleS        0.26026      0.04301         6.05      0.000
FeedRate        0.09034      0.03089         2.92      0.005
FR*D           -0.37046      0.07226        -5.13      0.000
SS*FR*D       0.0009054    0.0001935         4.68      0.000
FR*FR       -0.00021926   0.00008485        -2.58      0.013
SS*SS       -0.00027736   0.00006082        -4.56      0.000

S = 4.741        R-Sq = 86.0%      R-Sq(adj) = 84.2%

Analysis of Variance

Source            DF           SS           MS           F          P
Regression         6       6483.1       1080.5       48.08      0.000
Residual Error    47       1056.3         22.5
Total             53       7539.3

Source        DF      Seq SS
SpindleS       1      5238.4
FeedRate       1        33.6
FR*D           1       101.6
SS*FR*D        1       492.0
FR*FR          1       150.1
SS*SS          1       467.3

Unusual Observations
Obs   SpindleS   ToolHeat         Fit   StDev Fit     Residual     St Resid
 46        200    155.450     165.601       1.779      -10.151        -2.31R

R denotes an observation with a large standardized residual
```

Normal Probability Plot of the Residuals
(response is ToolHeat)

Residuals Versus the Fitted Values
(response is ToolHeat)

Residuals Versus the Order of the Data
(response is ToolHeat)

Residuals Versus SpindleS
(response is ToolHeat)

Residuals Versus FeedRate
(response is ToolHeat)

Residuals Versus ShldrD
(response is ToolHeat)
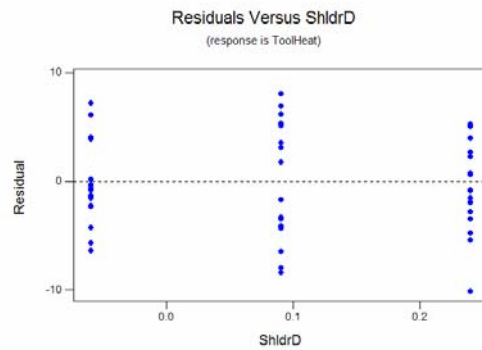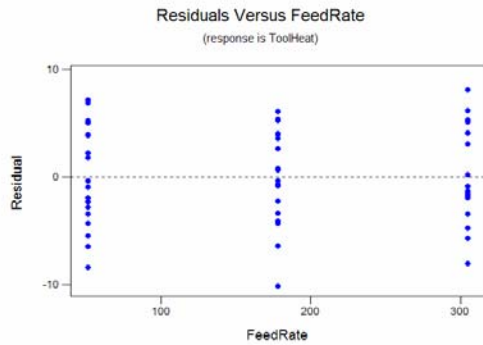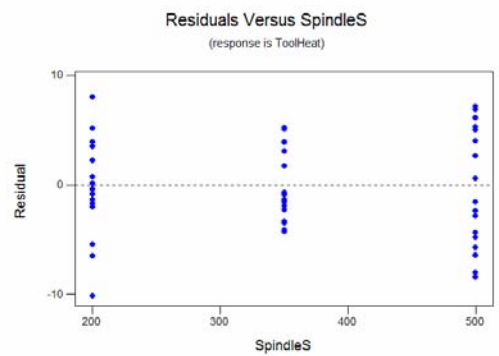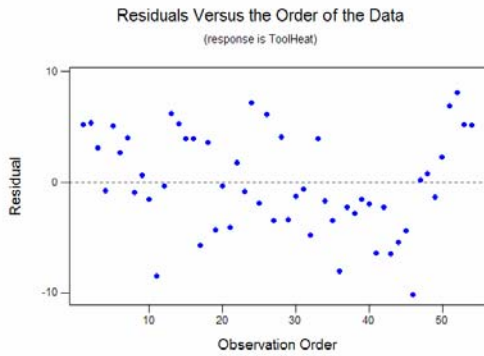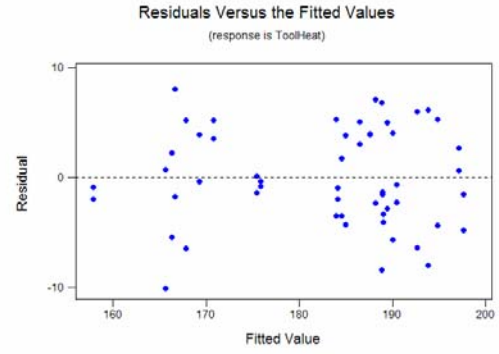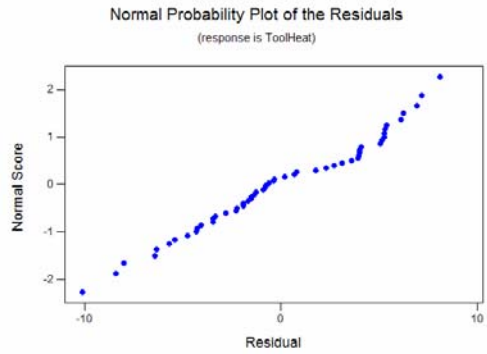
As noted in the plots, the Normal Probability Plot of the Residuals is virtually a straight line. The Residuals vs. Fitted Values plot shows some trend, but transformations of the data did not reducing the grouping of the data. The Residuals vs. Order of the Data shows very little trend, if any, in the data with respect to time, and the Residuals vs. Independent Variables plots show even spacing about the zero-residual line. Thus, the assumptions appear to have not been violated in a significant manner.

PERCENT ENERGY

Regression Analysis

```
The regression equation is
PercentEnergy = 3.66 + 0.00595 SpindleSpeed - 0.00756 FeedRate -0.000008 SS*FR
         + 0.00647 FR*D -0.000006 SS*SS +0.000015 FR*FR + 6.69 D*D
```

Predictor	Coef	StDev	T	P
Constant	3.6581	0.2434	15.03	0.000
SpindleS	0.005954	0.001357	4.39	0.000
FeedRate	-0.007560	0.001106	-6.84	0.000
SS*FR	-0.00000831	0.00000157	-5.29	0.000
FR*D	0.006467	0.001231	5.25	0.000
SS*SS	-0.00000617	0.00000188	-3.28	0.002
FR*FR	0.00001485	0.00000263	5.65	0.000
D*D	6.686	1.278	5.23	0.000

```
S = 0.1467     R-Sq = 95.1%     R-Sq(adj) = 94.3%
```

Analysis of Variance

Source	DF	SS	MS	F	P
Regression	7	19.1455	2.7351	127.11	0.000
Residual Error	46	0.9898	0.0215		
Total	53	20.1353			

Source	DF	Seq SS
SpindleS	1	0.0196
FeedRate	1	12.3669
SS*FR	1	0.6017
FR*D	1	4.6486
SS*SS	1	0.2315
FR*FR	1	0.6880
D*D	1	0.5892

Normal Probability Plot of the Residuals (response is PercentE)

Residuals Versus the Fitted Values (response is PercentE)

Residuals Versus the Order of the Data (response is PercentE)

Residuals Versus SpindleS (response is PercentE)

Residuals Versus FeedRate (response is PercentE)

Residuals Versus ShldrD (response is PercentE)
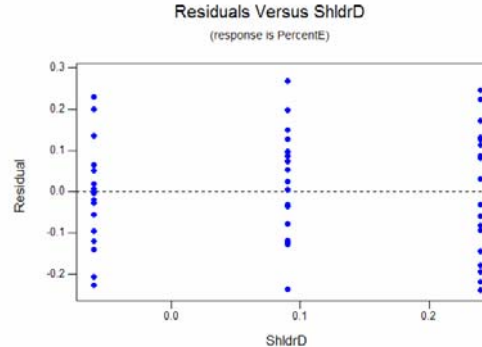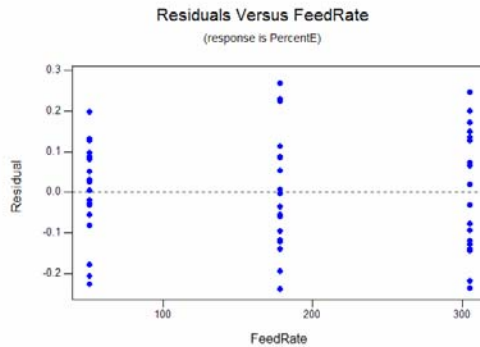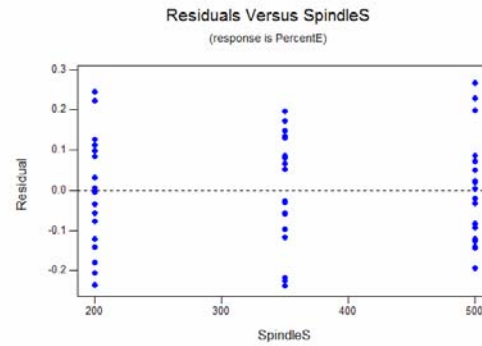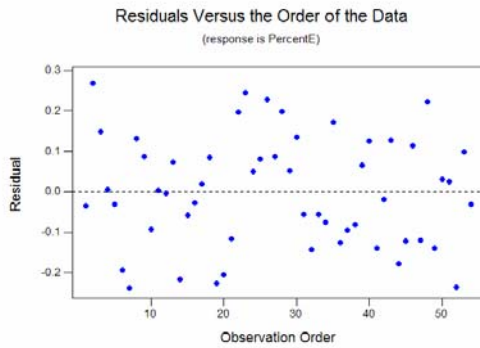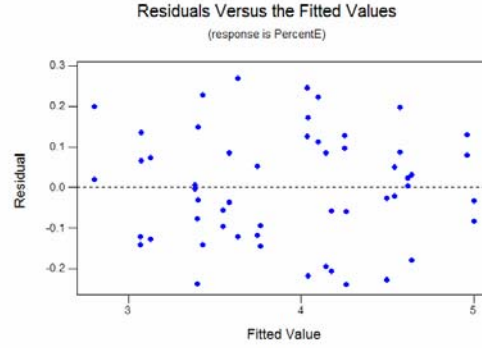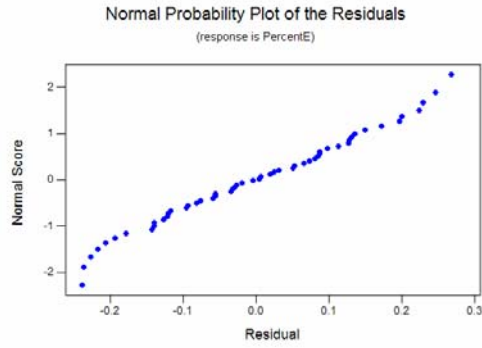
An analysis of the plots for the Percent Energy shows again that the assumptions were not violated. The Normal Probability Plot of the Residuals shows a virtually straight line. The Residuals vs. Fitted Values plot is randomly distributed, as is the data in the Residuals vs. Order of the Data. The Residuals vs. Independent Variables plots are evenly distributed, which was not the case for the other regression equations for the Percent Energy that were tested.

Appendix B

Thermal Conductivity of H13 Tool Steel

Thermal Conducivity for H-13 Tool Steel
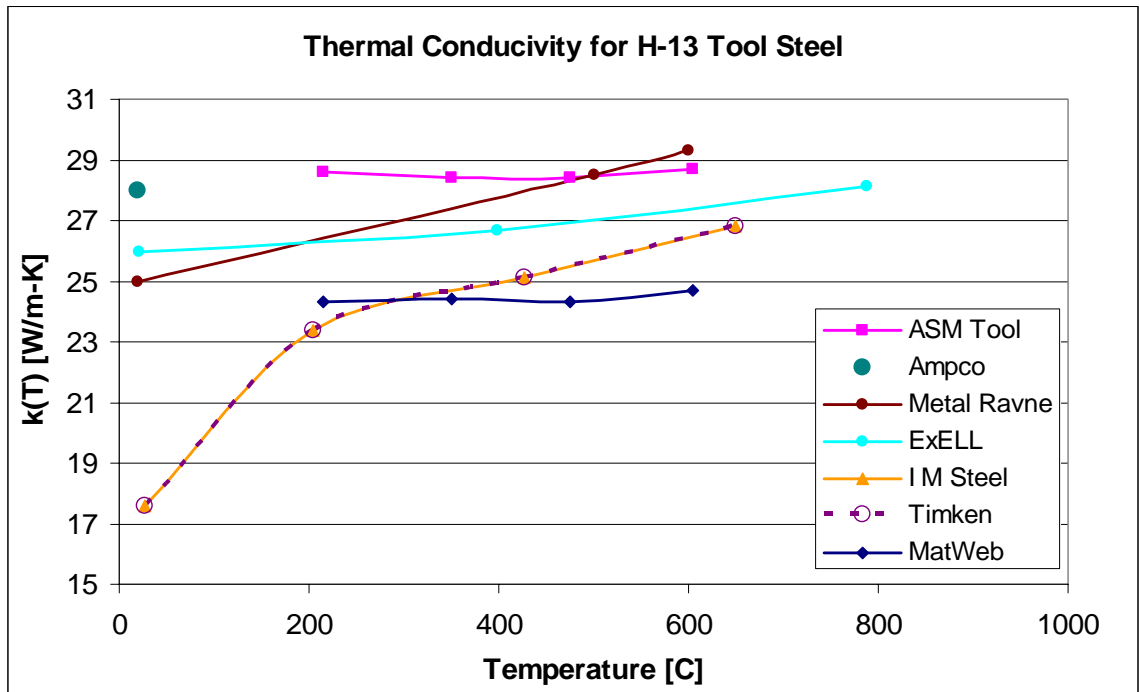
SOURCES

ASM Tool: Davies, J. R., *Tool Materials*, 1995, Materials Park, OH: ASM International, pp136.

Ampco: "H13 Tool Steel", available online at: www.ampcometal.com.

Metal Ravne: Metal Ravne, "Data Sheet: AISI: H13", available online at: www.sz-metal.si/en/.

ExELL: Ellwood Specialty Steel, "ExELL H-13 SMDQ-N Hot Work Tool Steel", available online at: www.ess.elwd.com/pdf/essh13.pdf.

I M Steel: International Mold Steel, Inc, "Premium H13: Physical Properties", available online at: www.imsteel.com/h13.htm.

Timken: Timken Latrobe Steel, "Data Sheet: TLS H13 Tool Steel", available online at: www.timken.com.

MatWeb: "H13 Hot Work Tool Steel", available online at: www.matweb.com.

Appendix C

FLUENT UDF File Example: Radially Varying Heat Input

```
/*********************************************

The purpose of this UDF is to define a heat flux
boundary condition as a function of radius for an
axisymmetric geometry.

HHH Parameter Combination - Experimental Weld 1497 (& 1484)
*********************************************/


#include "udf.h"

#define mu 0.3                  /** Coefficient of Friction **/
#define Fzlbs 14580             /** Z-force in lbf **/
#define Nrpm 500                /** Spindle Speed in rev. per min. **/
#define Roin 0.5                /** Outer Shoulder Radius in inches **/
#define Riin 0.1575             /** Inner Shoulder Radius in inches **/
#define Per 0.026               /** Percentage of power input **/


DEFINE_PROFILE(Horizontal, t, i)
{

        real x[ND_ND];
        real y, Fz, T, Ro, Ri;
        face_t f;

        Fz = Fzlbs * 4.44822;           /** Convert to Newtons **/
        T = Nrpm / 60 ;                 /** Convert to rev. per sec. **/
        Ro = Roin * 0.0254;             /** Convert to meters   **/
        Ri = Riin * 0.0254;             /** Convert to meters   **/

        printf("Horiz");

        begin_f_loop(f, t)
        {
                F_CENTROID(x, f, t);
                y = x[1];
                F_PROFILE(f, t, i) = ((Per*mu*Fz*2*T) / (Ro*Ro - Ri*Ri)) * y;
        }
        end_f_loop(f, t)
}
```

Appendix D

FLUENT UDF File Example: Uniform Heat Input

```
/********************************************
Base Heat Input Calculation for 0.1875" PL tool

The purpose of this UDF is to define a uniform heat flux
boundary condition as a function of input parameters
for an axisymmetric geometry.

LLL Parameter Combination (Uniform Heat Flux)
*********************************************/

#include "udf.h"

#define SS 200                      /** Input Spindle Speed [rpm] (200, 350, 500) **/
#define FR 51                       /** Input Feed Rate [mm/min.] (51, 178, 305) **/
#define D 0.24                      /** Input Shoulder Depth [mm] (0.24, 0.09, -0.06) **/
#define pin_bottom_area 3.294865e-5 /** Pin Bottom area [m2] **/
#define pin_rnd_area 2.7967604e-5   /** Pin Round area [m2] **/
#define pin_side_area 8.5862135e-5  /** Pin Side area [m2] **/
#define root_rnd_area 6.0355898e-5  /** Root Round area [m2] **/
#define shld_flat_area 0.00035198042 /** Shoulder Flat area [m2] **/
#define interface_area 0.00055911468 /** Total interface area [m2] (shld_rnd not included) **/


DEFINE_PROFILE(shld_flat, t, i)
{
        real x[ND_ND];
        /**real d, dmax, dmin, P; **/
        real total_heat_input, heat_flux;
        face_t f;

        printf("shld");

        total_heat_input = 123.6196726982 +0.2602579337*SS +0.0903300101*FR -
0.3704575647*FR*D + 0.0009054044*SS*FR*D -0.0002192565*FR*FR -0.0002773580*SS*SS ;

        heat_flux = total_heat_input/interface_area;

        begin_f_loop(f, t)
        {
                F_PROFILE(f, t, i) = heat_flux;
        }
        end_f_loop(f, t)
}


DEFINE_PROFILE(root_rnd, t, i)
{
        real x[ND_ND];
        real total_heat_input, heat_flux;
        face_t f;

        printf("root");

        total_heat_input = 123.6196726982 +0.2602579337*SS +0.0903300101*FR -
0.3704575647*FR*D +0.0009054044*SS*FR*D -0.0002192565*FR*FR -0.0002773580*SS*SS ;
```

```
            heat_flux = total_heat_input/interface_area;

            begin_f_loop(f, t)
            {
                    F_PROFILE(f, t, i) = heat_flux;
            }
            end_f_loop(f, t)
  }


DEFINE_PROFILE(pin_bottom, t, i)
{
            real x[ND_ND];
            real total_heat_input, heat_flux;
            face_t f;

            printf("pbottom");

            total_heat_input = 123.6196726982 +0.2602579337*SS +0.0903300101*FR -
0.3704575647*FR*D +0.0009054044*SS*FR*D -0.0002192565*FR*FR -0.0002773580*SS*SS ;

            heat_flux = total_heat_input/interface_area;

            begin_f_loop(f, t)
            {
                    F_PROFILE(f, t, i) = heat_flux;
            }
            end_f_loop(f, t)
}


DEFINE_PROFILE(pin_rnd, t, i)
{
            real x[ND_ND];
            real total_heat_input, heat_flux;
            face_t f;

            printf("prnd");

            total_heat_input = 123.6196726982 +0.2602579337*SS +0.0903300101*FR -
0.3704575647*FR*D + 0.0009054044*SS*FR*D -0.0002192565*FR*FR -0.0002773580*SS*SS ;

            heat_flux = total_heat_input/interface_area;

            begin_f_loop(f, t)
            {
                    F_PROFILE(f, t, i) = heat_flux;
            }
            end_f_loop(f, t)
}
```

```
DEFINE_PROFILE(pin_side, t, i)
{
        real x[ND_ND];
        real total_heat_input, heat_flux;
        /**real Fx, T, Ri, Var, BF, Hm;**/
        face_t f;

        printf(" pside ");

        total_heat_input = 123.6196726982 +0.2602579337*SS +0.0903300101*FR -
0.3704575647*FR*D +0.0009054044*SS*FR*D -0.0002192565*FR*FR -0.0002773580*SS*SS ;

        heat_flux = total_heat_input/interface_area;

        begin_f_loop(f, t)
        {
                F_PROFILE(f, t, i) = heat_flux;
        }
        end_f_loop(f, t)
}
```

Appendix E

FLUENT UDF File Example: Distributed Heat Input

```
/******************************************
Base Heat Input Calculation for 0.1875" PL tool

The purpose of this UDF is to define a heat flux
boundary condition as a function of input parameters
for an axisymmetric geometry.  The heat input is
distributed according to the fractional parameters
in the #define section.

LLL Parameter Combination (Distributed Heat Flux)
*********************************************/


#include "udf.h"

#define SS 200                  /** Input Spindle Speed [rpm] (200, 350, 500) **/
#define FR 51                   /** Input Feed Rate [mm/min.] (51, 178, 305) **/
#define D 0.24                  /** Input Shoulder Depth [mm] (0.24, 0.09, -0.06) **/
#define pin_bottom_area 3.294865e-5   /** Pin Bottom area [m2] **/
#define pin_rnd_area 2.7967604e-5     /** Pin Round area [m2] **/
#define pin_side_area 8.5862135e-5    /** Pin Side area [m2] **/
#define root_rnd_area 6.0355898e-5    /** Root Round area [m2] **/
#define shld_flat_area 0.00035198042  /** Shoulder Flat area [m2] **/
#define interface_area 0.00055911468  /** Total interface area [m2] (shld_rnd not included) **/
#define pin_bottom_per 0.003    /** Percentage of Heat Input applied on the Pin Bottom area **/
#define pin_rnd_per 0.003       /** Percentage of Heat Input applied on the Pin Round area **/
#define pin_side_per 0.004      /** Percentage of Heat Input applied on the Pin Side area **/
#define root_rnd_per 0.2        /** Percentage of Heat Input applied on the Root Round area **/


DEFINE_PROFILE(shld_flat, t, i)
{
        real x[ND_ND];
        /**real d, dmax, dmin, P; **/
        real total_heat_input, heat_flux;
        face_t f;

        printf("shld");


        total_heat_input = 123.6196726982 +0.2602579337*SS +0.0903300101*FR -
0.3704575647*FR*D + 0.0009054044*SS*FR*D -0.0002192565*FR*FR -0.0002773580*SS*SS ;

        heat_flux = (1 - (pin_bottom_per +pin_rnd_per +pin_side_per +root_rnd_per)) *
total_heat_input/shld_flat_area;

        begin_f_loop(f, t)
        {
                F_PROFILE(f, t, i) = heat_flux;
        }
        end_f_loop(f, t)
}
```

```
DEFINE_PROFILE(root_rnd, t, i)
{
        real x[ND_ND];
        real total_heat_input, heat_flux;
        face_t f;

        printf("root%.3lf", root_rnd_per);

        total_heat_input = 123.6196726982 +0.2602579337*SS +0.0903300101*FR -
0.3704575647*FR*D + 0.0009054044*SS*FR*D -0.0002192565*FR*FR -0.0002773580*SS*SS ;

        heat_flux = root_rnd_per * total_heat_input/root_rnd_area;

        begin_f_loop(f, t)
        {
                F_PROFILE(f, t, i) = heat_flux;
        }
        end_f_loop(f, t)
}


DEFINE_PROFILE(pin_bottom, t, i)
{
        real x[ND_ND];
        real total_heat_input, heat_flux;
        face_t f;

        printf("pbottom%.3lf", pin_bottom_per);

        total_heat_input = 123.6196726982 +0.2602579337*SS +0.0903300101*FR -
0.3704575647*FR*D +0.0009054044*SS*FR*D -0.0002192565*FR*FR -0.0002773580*SS*SS ;

        heat_flux = pin_bottom_per * total_heat_input/pin_bottom_area;

        begin_f_loop(f, t)
        {
                F_PROFILE(f, t, i) = heat_flux;
        }
        end_f_loop(f, t)
}


DEFINE_PROFILE(pin_rnd, t, i)
{
        real x[ND_ND];
        real total_heat_input, heat_flux;
        face_t f;

        printf("prnd%.3lf", pin_rnd_per);


        total_heat_input = 123.6196726982 +0.2602579337*SS +0.0903300101*FR -
0.3704575647*FR*D + 0.0009054044*SS*FR*D -0.0002192565*FR*FR -0.0002773580*SS*SS ;

        heat_flux = pin_rnd_per * total_heat_input/pin_rnd_area;
```

```
        begin_f_loop(f, t)
        {
                F_PROFILE(f, t, i) = heat_flux;
        }
        end_f_loop(f, t)
}


DEFINE_PROFILE(pin_side, t, i)
{
        real x[ND_ND];
        real total_heat_input, heat_flux;
        /**real Fx, T, Ri, Var, BF, Hm;**/
        face_t f;

        printf(" pside%.3lf ", pin_side_per);

        total_heat_input = 123.6196726982 +0.2602579337*SS +0.0903300101*FR -
0.3704575647*FR*D + 0.0009054044*SS*FR*D -0.0002192565*FR*FR -0.0002773580*SS*SS ;

        heat_flux = pin_side_per * total_heat_input/pin_side_area;

        begin_f_loop(f, t)
        {
                F_PROFILE(f, t, i) = heat_flux;
        }
        end_f_loop(f, t)
}
```

Appendix F

Experimental Data (steady-state averages)

SS	FR	D	Spindle Speed [rpm]	Feed Rate [mm/min.]	Shoulder Depth [mm]	Weld ID	Measured Depth [mm]	X-force [kN]	Y-force [kN]	Z-force [kN]	Run Order
L	L	L	200	51	0.24	1520	0.242	3.90	-0.94	33.77	44
L	L	L	200	51	0.24	1528	0.241	4.10	-1.02	31.67	50
L	L	M	200	51	0.09	1519	0.088	3.68	-0.51	33.98	43
L	L	M	200	51	0.09	1531	0.086	3.90	-0.59	39.61	53
L	L	H	200	51	-0.06	1487	-0.067	3.91	-0.56	44.91	20
L	L	H	200	51	-0.06	1506	-0.064	3.91	-0.44	45.02	33
L	M	L	200	178	0.24	1522	0.240	5.99	-0.74	31.82	46
L	M	L	200	178	0.24	1524	0.238	7.37	-0.51	34.57	48
L	M	M	200	178	0.09	1461	0.086	6.39	-0.46	53.76	1
L	M	M	200	178	0.09	1485	0.091	6.77	-0.99	53.23	18
L	M	H	200	178	-0.06	1465	-0.068	6.67	-0.66	59.56	4
L	M	H	200	178	-0.06	1479	-0.067	7.14	-0.90	60.79	12
L	H	L	200	305	0.24	1491	0.244	8.42	2.35	35.46	23
L	H	L	200	305	0.24	1515	0.241	8.54	2.26	35.23	40
L	H	M	200	305	0.09	1507	0.095	7.03	-0.06	47.46	34
L	H	M	200	305	0.09	1530	0.095	8.90	-0.71	59.44	52
L	H	H	200	305	-0.06	1523	-0.063	8.82	-0.62	70.19	47
L	H	H	200	305	-0.06	1527	-0.057	8.90	-0.75	68.74	49
M	L	L	350	51	0.24	1473	0.241	3.50	-0.29	27.50	8
M	L	L	350	51	0.24	1493	0.242	3.63	-0.57	28.20	25
M	L	M	350	51	0.09	1490	0.087	4.18	-0.72	34.41	22
M	L	M	350	51	0.09	1496	0.088	3.87	-0.43	33.19	27
M	L	H	350	51	-0.06	1483	-0.064	4.16	-0.22	37.87	16
M	L	H	350	51	-0.06	1486	-0.064	4.31	-0.34	39.02	19
M	M	L	350	178	0.24	1470	0.240	7.00	-0.54	44.93	7
M	M	L	350	178	0.24	1482	0.242	6.52	-0.47	40.67	15
M	M	M	350	178	0.09	1488	0.088	7.49	-0.75	54.02	21
M	M	M	350	178	0.09	1498	0.085	7.31	-0.56	46.60	29
M	M	H	350	178	-0.06	1502	-0.063	8.60	-0.33	61.84	31
M	M	H	350	178	-0.06	1511	-0.066	8.64	-0.28	60.99	37
M	H	L	350	305	0.24	1481	0.247	8.54	0.13	43.35	14
M	H	L	350	305	0.24	1508	0.247	7.31	1.22	35.52	35
M	H	M	350	305	0.09	1464	0.091	8.16	-0.68	51.38	3
M	H	M	350	305	0.09	1533	0.092	10.20	-0.52	58.63	54
M	H	H	350	305	-0.06	1500	-0.060	9.52	-0.64	62.49	30
M	H	H	350	305	-0.06	1514	-0.064	9.94	-0.60	64.23	39
H	L	L	500	51	0.24	1467	0.240	3.34	-0.07	27.38	5
H	L	L	500	51	0.24	1512	0.240	4.11	-0.09	27.37	38
H	L	M	500	51	0.09	1477	0.089	3.53	-0.03	29.11	11
H	L	M	500	51	0.09	1529	0.087	4.77	-0.42	35.09	51
H	L	H	500	51	-0.06	1492	-0.065	4.96	0.02	36.56	24
H	L	H	500	51	-0.06	1518	-0.063	3.63	0.24	32.52	42
H	M	L	500	178	0.24	1469	0.238	7.26	-0.71	44.76	6
H	M	L	500	178	0.24	1474	0.239	6.49	0.03	38.31	9
H	M	M	500	178	0.09	1462	0.086	6.48	-0.38	44.99	2
H	M	M	500	178	0.09	1521	0.085	8.74	-0.60	53.31	45
H	M	H	500	178	-0.06	1494	-0.067	8.03	-0.74	54.04	26
H	M	H	500	178	-0.06	1517	-0.069	8.22	-0.56	52.93	41
H	H	L	500	305	0.24	1476	0.244	9.64	0.24	44.83	10
H	H	L	500	305	0.24	1504	0.244	9.97	0.53	46.06	32
H	H	M	500	305	0.09	1480	0.090	10.37	-0.39	62.27	13
H	H	M	500	305	0.09	1509	0.089	10.65	-0.53	59.75	36
H	H	H	500	305	-0.06	1484	-0.058	10.36	-0.28	65.60	17
H	H	H	500	305	-0.06	1497	-0.061	10.03	-0.39	64.11	28
Minimum								3.34	-1.02	27.37	
Maximum								10.65	2.35	70.19	

SS	FR	D	Spindle Speed [rpm]	Feed Rate [mm/min.]	Shoulder Depth [mm]	Weld ID	Pin Center Temp [C]	Root Temp [C]	Shoulder Temp [C]	Motor Power [kW]	Run Order
L	L	L	200	51	0.24	1520	442.9	422.3	417.4	3.86	44
L	L	L	200	51	0.24	1528	439.4	418.3	413.9	3.86	50
L	L	M	200	51	0.09	1519	443.6	422.9	417.5	3.93	43
L	L	M	200	51	0.09	1531	453.1	433.3	426.1	4.22	53
L	L	H	200	51	-0.06	1487	460.2	441.8	436.1	4.50	20
L	L	H	200	51	-0.06	1506	463.7	443.0	439.1	4.45	33
L	M	L	200	178	0.24	1522	405.1	396.2	399.6	3.94	46
L	M	L	200	178	0.24	1524	411.3	400.5	402.3	4.10	48
L	M	M	200	178	0.09	1461	447.2	438.5	430.1	5.20	1
L	M	M	200	178	0.09	1485	444.3	432.3	425.9	5.00	18
L	M	H	200	178	-0.06	1465	450.3	440.8	433.2	5.40	4
L	M	H	200	178	-0.06	1479	448.4	435.4	431.3	5.44	12
L	H	L	200	305	0.24	1491	371.0	370.9	379.7	3.91	23
L	H	L	200	305	0.24	1515	371.7	370.6	378.4	4.00	40
L	H	M	200	305	0.09	1507	418.2	410.8	407.7	5.21	34
L	H	M	200	305	0.09	1530	432.6	427.3	421.7	5.77	52
L	H	H	200	305	-0.06	1523	435.5	428.5	420.4	6.20	47
L	H	H	200	305	-0.06	1527	433.6	426.1	418.9	6.19	49
M	L	L	350	51	0.24	1473	480.8	451.3	437.7	4.12	8
M	L	L	350	51	0.24	1493	483.6	455.0	450.9	4.14	25
M	L	M	350	51	0.09	1490	489.0	463.4	459.2	4.43	22
M	L	M	350	51	0.09	1496	486.8	457.7	450.5	4.41	27
M	L	H	350	51	-0.06	1483	493.4	468.0	464.1	4.76	16
M	L	H	350	51	-0.06	1486	493.5	466.9	463.5	4.75	19
M	M	L	350	178	0.24	1470	485.0	465.3	460.3	5.29	7
M	M	L	350	178	0.24	1482	481.6	462.6	456.7	5.09	15
M	M	M	350	178	0.09	1488	486.5	465.5	460.2	5.63	21
M	M	M	350	178	0.09	1498	485.0	462.8	458.5	5.41	29
M	M	H	350	178	-0.06	1502	491.4	467.3	464.7	5.97	31
M	M	H	350	178	-0.06	1511	490.9	465.9	461.1	5.99	37
M	H	L	350	305	0.24	1481	465.9	451.1	451.7	5.48	14
M	H	L	350	305	0.24	1508	447.0	435.8	440.0	4.81	35
M	H	M	350	305	0.09	1464	471.5	459.3	455.3	5.86	3
M	H	M	350	305	0.09	1533	473.0	456.8	452.5	6.21	54
M	H	H	350	305	-0.06	1500	476.5	461.2	457.2	6.38	30
M	H	H	350	305	-0.06	1514	478.8	460.8	457.0	6.49	39
H	L	L	500	51	0.24	1467	500.9	471.7	463.3	4.96	5
H	L	L	500	51	0.24	1512	498.6	468.4	462.2	4.84	38
H	L	M	500	51	0.09	1477	500.3	467.5	455.6	4.94	11
H	L	M	500	51	0.09	1529	503.9	472.7	469.7	5.26	51
H	L	H	500	51	-0.06	1492	506.4	476.6	473.6	5.30	24
H	L	H	500	51	-0.06	1518	502.8	470.3	463.5	5.15	42
H	M	L	500	178	0.24	1469	502.8	476.9	472.3	6.10	6
H	M	L	500	178	0.24	1474	500.7	472.1	467.8	5.72	9
H	M	M	500	178	0.09	1462	505.0	479.6	475.1	6.17	2
H	M	M	500	178	0.09	1521	502.3	471.9	467.7	6.47	45
H	M	H	500	178	-0.06	1494	506.9	477.4	478.2	6.47	26
H	M	H	500	178	-0.06	1517	506.4	477.9	475.4	6.70	41
H	H	L	500	305	0.24	1476	492.4	467.5	466.1	6.38	10
H	H	L	500	305	0.24	1504	489.4	464.1	462.0	6.36	32
H	H	M	500	305	0.09	1480	500.2	473.4	472.2	7.30	13
H	H	M	500	305	0.09	1509	495.5	468.6	462.8	7.23	36
H	H	H	500	305	-0.06	1484	501.8	478.7	477.8	7.58	17
H	H	H	500	305	-0.06	1497	500.8	476.3	473.7	7.52	28
Minimum							371.0	370.6	378.4	3.86	
Maximum							506.9	479.6	478.2	7.58	

128

SS	FR	D	Motor Power [kW]	Gear Losses [kW]	Total Energy Input [kW]	Temp. Gradient [°C/mm]	h [W/m²-K]	Convective Losses [W]	Radiative Losses [W]	Tool Heat Input [W]	Percent Energy [%]
L	L	L	3.86	0.25	3.61	10.4	11	3.48	8.18	160.88	4.46
L	L	L	3.86	0.25	3.61	10.9	11	3.42	7.85	168.57	4.67
L	L	M	3.93	0.25	3.69	10.4	11	3.49	8.22	161.32	4.38
L	L	M	4.22	0.25	3.98	11.2	11	3.53	8.43	173.00	4.35
L	L	H	4.50	0.25	4.25	10.8	11	3.65	9.10	168.88	3.97
L	L	H	4.45	0.25	4.21	11.1	11	3.67	9.18	173.21	4.12
L	M	L	3.94	0.25	3.69	10.1	11	3.32	7.37	155.45	4.21
L	M	L	4.10	0.25	3.85	10.8	11	3.30	7.27	166.38	4.32
L	M	M	5.20	0.25	4.96	11.4	11	3.56	8.59	175.97	3.55
L	M	M	5.00	0.25	4.75	11.3	11	3.52	8.40	174.31	3.67
L	M	H	5.40	0.25	5.16	11.3	11	3.59	8.79	175.06	3.39
L	M	H	5.44	0.25	5.19	11.3	11	3.57	8.66	175.48	3.38
L	H	L	3.91	0.25	3.66	10.3	11	3.10	6.37	157.00	4.28
L	H	L	4.00	0.25	3.75	10.2	11	3.09	6.29	155.88	4.16
L	H	M	5.21	0.25	4.96	10.7	11	3.37	7.61	164.93	3.32
L	H	M	5.77	0.25	5.52	11.3	11	3.48	8.17	174.73	3.16
L	H	H	6.20	0.25	5.95	11.4	11	3.45	8.04	175.62	2.95
L	H	H	6.19	0.25	5.95	11.3	11	3.45	8.01	174.08	2.93
M	L	L	4.12	0.53	3.60	11.8	15	4.93	8.93	183.21	5.09
M	L	L	4.14	0.53	3.62	11.6	15	5.13	9.75	182.20	5.04
M	L	M	4.43	0.53	3.91	11.9	15	5.22	10.17	186.31	4.77
M	L	M	4.41	0.53	3.89	11.6	15	5.12	9.71	181.06	4.66
M	L	H	4.76	0.53	4.23	12.0	15	5.28	10.43	188.86	4.47
M	L	H	4.75	0.53	4.23	11.5	15	5.32	10.57	180.67	4.27
M	M	L	5.29	0.53	4.77	12.3	15	5.21	10.10	191.59	4.02
M	M	L	5.09	0.53	4.57	12.3	15	5.16	9.91	191.55	4.20
M	M	M	5.63	0.53	5.10	11.8	15	5.25	10.27	184.95	3.63
M	M	M	5.41	0.53	4.88	11.8	15	5.23	10.18	185.68	3.80
M	M	H	5.97	0.53	5.44	12.1	15	5.29	10.48	189.85	3.49
M	M	H	5.99	0.53	5.46	12.0	15	5.24	10.25	188.24	3.45
M	H	L	5.48	0.53	4.95	12.1	15	5.10	9.65	189.28	3.82
M	H	L	4.81	0.53	4.28	11.6	15	4.98	9.11	180.51	4.21
M	H	M	5.86	0.53	5.33	12.1	15	5.15	9.83	189.57	3.55
M	H	M	6.21	0.53	5.69	12.3	15	5.10	9.66	191.59	3.37
M	H	H	6.38	0.53	5.85	12.0	15	5.19	10.00	187.66	3.21
M	H	H	6.49	0.53	5.97	12.0	15	5.19	10.01	187.43	3.14
H	L	L	4.96	1.04	3.91	12.4	18	6.29	10.25	194.52	4.97
H	L	L	4.84	1.04	3.80	11.8	18	6.33	10.38	186.64	4.92
H	L	M	4.94	1.04	3.90	11.4	18	6.27	10.14	180.40	4.62
H	L	M	5.26	1.04	4.22	12.4	18	6.40	10.69	195.72	4.64
H	L	H	5.30	1.04	4.26	12.4	18	6.48	10.97	195.36	4.59
H	L	H	5.15	1.04	4.11	11.7	18	6.37	10.53	185.90	4.52
H	M	L	6.10	1.04	5.06	12.7	18	6.41	10.73	199.77	3.95
H	M	L	5.72	1.04	4.68	12.6	18	6.35	10.51	197.74	4.23
H	M	M	6.17	1.04	5.13	12.7	18	6.46	10.92	200.23	3.90
H	M	M	6.47	1.04	5.43	12.1	18	6.41	10.69	190.52	3.51
H	M	H	6.47	1.04	5.43	12.6	18	6.52	11.17	198.73	3.66
H	M	H	6.70	1.04	5.66	11.7	18	6.56	11.28	186.26	3.29
H	H	L	6.38	1.04	5.34	12.5	18	6.33	10.41	196.10	3.67
H	H	L	6.36	1.04	5.32	12.3	18	6.28	10.23	192.88	3.62
H	H	M	7.30	1.04	6.26	12.7	18	6.41	10.72	200.03	3.20
H	H	M	7.23	1.04	6.19	11.7	18	6.35	10.47	185.81	3.00
H	H	H	7.58	1.04	6.54	11.5	18	6.63	11.55	184.31	2.82
H	H	H	7.52	1.04	6.48	12.3	18	6.49	11.01	194.09	3.00
Minimum			3.86		3.60	10.06		3.09	6.29	155.45	2.82
Maximum			7.58		6.54	12.71		6.63	11.55	200.23	5.09

Appendix G

Numerical/Experimental Comparison Data

LINEARLY VARYING HEAT INPUT

			Linearly Varying Heat Input				Experimental Data					
SS	FR	D	Max. T_{pred}	PC T_{pred}	RT T_{pred}	SH T_{pred}	PC T_{exp}	RT T_{exp}	SH T_{exp}	PC T_{pred} - T_{exp}	RT T_{pred} - T_{exp}	SH T_{pred} - T_{exp}
L	L	L										
L	L	M										
L	L	H	451.2	414.9	409.8	431.1	462	442	438	-47	-33	-7
L	M	L										
L	M	M										
L	M	H										
L	H	L	421.7	387.9	383.1	403.1	371	371	379	17	12	24
L	H	M										
L	H	H	465.9	428.4	423.1	445	435	427	420	-6	-4	25
M	L	L										
M	L	M										
M	L	H										
M	M	L										
M	M	M										
M	M	H										
M	H	L										
M	H	M										
M	H	H										
H	L	L										
H	L	M										
H	L	H	491.8	452	446.2	469.2	505	473	469	-53	-27	1
H	M	L										
H	M	M										
H	M	H										
H	H	L										
H	H	M										
H	H	H	499.4	458.9	453.1	476.4	501	478	476	-42	-24	1

UNIFORM HEAT INPUT

SS	FR	D	Uniform				Experimental Data					
			Max. T_{pred}	PC T_{pred}	RT T_{pred}	SH T_{pred}	PC T_{exp}	RT T_{exp}	SH T_{exp}	PC $T_{pred} - T_{exp}$	RT $T_{pred} - T_{exp}$	SH $T_{pred} - T_{exp}$
L	L	L	599.4	571.2	434.4	407.4	441	420	416	130	14	-8
L	L	M	604.3	575.9	437.9	410.7	448	428	422	128	10	-11
L	L	H	609.1	580.5	441.4	413.9	462	442	438	119	-1	-24
L	M	L	597.1	569	432.8	406	408	398	401	161	34	5
L	M	M	614.2	585.3	445	417.2	446	435	428	140	10	-11
L	M	H	631.3	601.6	457	428.4	449	438	432	152	19	-4
L	H	L	570.7	543.9	414.1	388.6	371	371	379	173	43	10
L	H	M	600.2	572	435	408	425	419	415	147	16	-7
L	H	H	629.5	600	455.8	427.3	435	427	420	165	29	8
M	L	L	655.7	624.5	473.1	442.8	482	453	444	142	20	-1
M	L	M	657.1	625.8	474.1	443.7	488	461	455	138	14	-11
M	L	H	658.4	627.1	475	444.6	493	467	464	134	8	-19
M	M	L	667.2	635.4	481.2	450.3	483	464	459	152	17	-8
M	M	M	672	640	484.6	453.4	486	464	459	154	20	-6
M	M	H	676.8	644.5	487.9	456.4	491	467	463	153	21	-6
M	H	L	655.2	624	472.7	442.4	456	443	446	168	29	-3
M	H	M	663.4	631.8	478.5	447.8	472	458	454	160	20	-6
M	H	H	671.5	639.6	484.2	453.1	478	461	457	162	23	-4
H	L	L	670.6	638.5	482.7	451.3	500	470	463	139	13	-11
H	L	M	668.5	636.6	481.3	449.9	502	470	463	134	11	-13
H	L	H	666.4	634.6	478.9	448.5	505	473	469	130	5	-20
H	M	L	695.8	662.4	500.3	467.5	502	475	470	161	26	-3
H	M	M	688.4	655.5	495.2	462.8	504	476	471	152	19	-9
H	M	H	681.2	648.6	490.2	458.1	507	478	477	142	13	-19
H	H	L	697.5	664.1	501.6	468.7	491	466	464	173	36	5
H	H	M	685.1	652.3	492.9	460.6	498	471	468	154	22	-7
H	H	H	672.6	640.4	484.1	452.5	501	478	476	139	7	-23

DISTRIBUTED HEAT INPUT

SS	FR	D	Distributed Heat Input				Experimental Data			PC	RT	SH
			Max. T_{pred}	PC T_{pred}	RT T_{pred}	SH T_{pred}	PC T_{exp}	RT T_{exp}	SH T_{exp}	$T_{pred} - T_{exp}$	$T_{pred} - T_{exp}$	$T_{pred} - T_{exp}$
L	L	L	447.6	440.1	418.6	414.8	441	420	416	-1	-2	-1
L	L	M	451.2	443.6	422	418.1	448	428	422	-5	-6	-4
L	L	H	454.8	447.1	425.3	421.3	462	442	438	-15	-17	-16
L	M	L	446	438.4	417.1	413.2	408	398	401	30	19	12
L	M	M	458.4	450.8	428.7	424.7	446	435	428	5	-7	-3
L	M	H	470.9	463	440.3	436.1	449	438	432	14	2	4
L	H	L	426.6	419.4	399.1	395.5	371	371	379	48	28	16
L	H	M	448.2	440.7	419.2	415.3	425	419	415	15	0	1
L	H	H	469.6	461.7	439.1	434.9	435	427	420	27	12	15
M	L	L	487.6	479.3	455.5	450.8	482	453	444	-3	2	7
M	L	M	488.6	480.3	456.4	451.7	488	461	455	-8	-4	-3
M	L	H	489.6	481.2	457.4	452.6	493	467	464	-12	-10	-11
M	M	L	496	487.5	463.3	458.4	483	464	459	4	-1	0
M	M	M	499.4	490.9	466.5	461.5	486	464	459	5	2	2
M	M	H	502.9	494.3	469.7	464.7	491	467	463	3	3	2
M	H	L	487.2	478.9	455.2	450.4	456	443	446	22	12	5
M	H	M	493.2	484.8	460.7	455.8	472	458	454	13	3	2
M	H	H	499.1	490.6	466.2	461.2	478	461	457	13	5	4
H	L	L	497.6	489.1	464.6	459.4	500	470	463	-11	-5	-3
H	L	M	496.1	487.6	463.2	458	502	470	463	-15	-7	-5
H	L	H	494.6	486.1	461.8	456.7	505	473	469	-18	-12	-12
H	M	L	515.8	506.9	481.4	476	502	475	470	5	7	6
H	M	M	510.5	501.8	476.6	471.2	504	476	471	-2	1	0
H	M	H	505.3	496.6	471.7	466.4	507	478	477	-10	-6	-10
H	H	L	517.1	508.2	482.6	477.1	491	466	464	17	17	13
H	H	M	508.1	499.3	474.3	468.9	498	471	468	1	3	1
H	H	H	499.1	490.4	465.9	460.7	501	478	476	-11	-12	-15